

## 13

# Physiological Modeling

*John D. Enderle, PhD*

## O U T L I N E

|   |     |   |     |
|---|-----|---|-----|
| 13.1 Introduction   | 818 | 13.7 The 1995 Linear Homeomorphic Saccadic Eye Movement Model | 864 |
| 13.2 An Overview of the Fast Eye Movement System                        | 821 | 13.8 The 2009 Linear Homeomorphic Saccadic Eye Movement Model | 878 |
| 13.3 The Westheimer Saccadic Eye Movement Model                         | 828 | 13.9 Saccade Neural Pathways                                  | 905 |
| 13.4 The Saccade Controller   | 835 | 13.10 System Identification                                   | 910 |
| 13.5 Development of an Oculomotor Muscle Model                          | 838 | 13.11 Exercises   | 927 |
| 13.6 The 1984 Linear Reciprocal Innervation Saccadic Eye Movement Model | 852 | References  | 935 |

## AT THE CONCLUSION OF THIS CHAPTER, STUDENTS WILL BE ABLE TO:

- Describe the process used to build a mathematical physiological model.
- Qualitatively describe a saccadic eye movement.
- Describe the saccadic eye movement system with a second order model.
- Explain the importance of the pulse-step saccadic control signal.
- Explain how a muscle operates using a nonlinear and linear muscle model.
- Simulate a saccade with a fourth order saccadic eye movement model.
- Estimate the parameters of a model using system identification.

### 13.1 INTRODUCTION

A *quantitative* physiological model is a mathematical representation that approximates the behavior of an actual physiological system. *Qualitative* physiological models, most often used by biologists, describe the actual physiological system without the use of mathematics. Quantitative physiological models, however, are much more useful and are the subject of this chapter. Physiological systems are almost always dynamic and mathematically characterized with differential equations. The modeling techniques developed in this chapter are intimately tied to many other interdisciplinary areas, such as physiology, biophysics, and biochemistry, and involve electrical and mechanical analogs. A model is usually constructed using basic and natural laws. This chapter extends this experience by presenting models that are more complex and involve larger systems.

Creating a model is always accompanied by carrying out an experiment and obtaining data. The best experiment is one that provides data that are related to variables used in the model. Consequently, the design and execution of an experiment is one of the most important and time-consuming tasks in modeling. A model constructed from basic and natural laws then becomes a tool for explaining the underlying processes that cause the experimental data and predicting the behavior of the system to other types of stimuli. Models serve as vehicles for thinking, organizing complex data, and testing hypotheses. Ultimately, modeling's most important goals are the generation of new knowledge, prediction of observations before they occur, and assistance in designing new experiments.

Figure 13.1 illustrates the typical steps in developing a model. The first step involves observations from an experiment or a phenomenon that leads to a conjecture or a verbal description of the physiological system. An initial hypothesis is formed via a mathematical model. The strength of the model is tested by obtaining data and testing the model against the data. If the model performs adequately, the model is satisfactory, and a solution is stated. If the model does not meet performance specifications, then the model is updated, and additional experiments are carried out. Usually some of the variables in the model are observable and some are not. New experiments provide additional data that increase the understanding of the physiological system by providing information about previously unobservable variables, which improves the model. The process of testing the model against the data continues until a satisfactory solution is attained. Usually a statistical test is performed to test the goodness of fit between the model and the data. One of the characteristics of a good model is how well it predicts the future performance of the physiological system.

The introduction of the digital computer, programming languages, and simulation software has caused a rapid change in the use of physiological models. Before digital computers, mathematical models of biomedical systems were either oversimplified or involved a great deal of hand calculation, as described in the Hodgkin-Huxley investigations published in 1952. Today, digital computers have become so common that the terms *modeling* and *simulation* have almost become synonymous. This has allowed the development of much more realistic or homeomorphic models that include as much knowledge as possible about the structure and interrelationships of the physiological system without any overriding concern about the number of calculations. Models of neuron networks and muscle cross-bridge models involving thousands of differential equations are becoming quite commonplace.

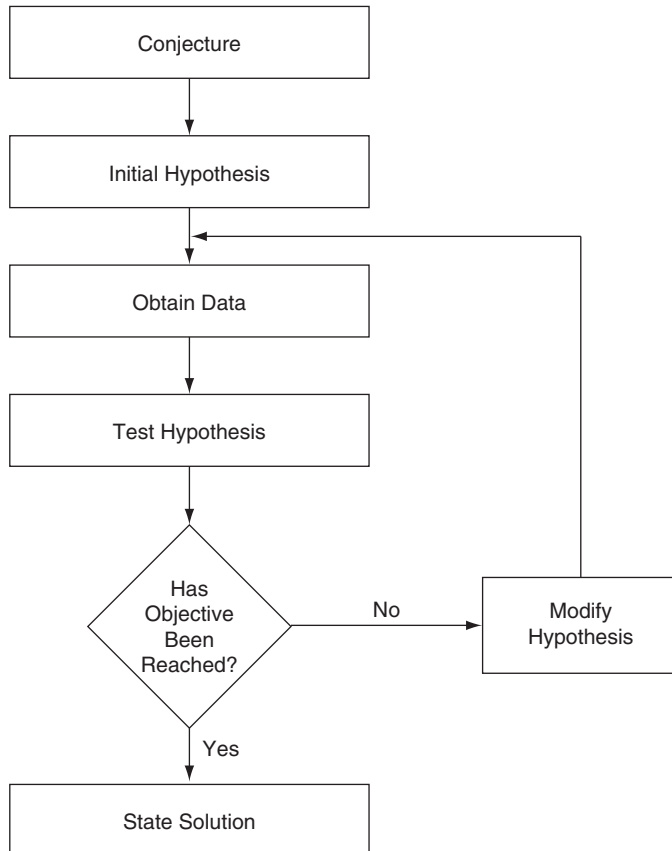


FIGURE 13.1 Flow chart for modeling.

While models can continue to be made more complex, it is important to evaluate the value added with each stage of complexity. The model should be made as simple as possible to explain the data but not so simple that it becomes meaningless. On the other hand, a model that is made too complex is also of little use.

### 13.1.1 Deterministic and Stochastic Models

A deterministic model is one that has an exact solution that relates the independent variables of the model to one another and to the dependent variable. For a given set of initial conditions, a deterministic model yields the same solution each and every time. A stochastic model involves random variables that are functions of time and include probabilistic considerations. For a given set of initial conditions, a stochastic model yields a different solution each and every time. Suffice it to say that solutions involving stochastic models are much more involved than the solution for a deterministic model.

It is interesting to note that all deterministic models include some measurement error. The measurement error introduces a probabilistic element into the deterministic model, so it might be considered stochastic. However, in this chapter, models are deterministic if their principle features lead to definitive predictions. On the other hand, models are stochastic if their principle features depend on probabilistic elements. This chapter is primarily concerned with deterministic models.

### 13.1.2 Solutions

There are two types of solutions available to the modeler. A closed form solution exists for models that can be solved by analytic techniques, such as solving a differential equation using the classical technique or by using Laplace transforms. For example, given the following differential equation

$$\ddot{x} + 4\dot{x} + 3x = 9$$

with initial conditions  $x(0) = 0$  and  $\dot{x}(0) = 1$ , the solution is found as

$$x(t) = (e^{-3t} - 4e^{-t} + 3)u(t)$$

A numerical or simulation solution exists for models that have no closed form solution. Consider the following function:

$$x = \int_{-20}^{20} \frac{e^{\frac{-1}{2} \left(\frac{t-7}{33}\right)^2}}{33\sqrt{2\pi}} dt$$

This function (the area under a Gaussian curve) has no closed form solution and must be solved using an approximation technique, such as the trapezoidal rule for integration. Most nonlinear differential equations do not have an exact solution and must be solved via an iterative method or simulation package such as SIMULINK. This was the situation in Chapter 12 when the Hodgkin-Huxley model was solved.

#### **Inverse Solutions**

Engineers often design and build systems to a predetermined specification. They often use a model to predict how the system will behave because a model is efficient and economical. The model that is built is called a plant and consists of parameters that completely describe the system: the characteristic equation. The engineer selects the parameters of the plant to achieve a certain set of specifications such as rise time, settling time, or peak overshoot time.

In contrast, biomedical engineers involved with physiological modeling do not build the physiological system but only observe the behavior of the system—the input and output of the system—and then characterize it with a model. Characterizing the model as illustrated in [Figure 13.1](#) involves identifying the form or structure of the model, collecting data, and then using the data to estimate the parameters of the model. The goal of physiological modeling is not to design a system but to identify the components (or parameters) of the system. Most often, data needed for building the model are not the data that can be

collected using existing bioinstrumentation, biosensors, and biosignal processing, as discussed in Chapters 8–10. Typically, the recorded data are transformed from measurement data into estimates of the variables used in the model. Collecting appropriate data is usually the most difficult aspect of the discovery process.

Model building typically involves estimating the parameters of the model that optimize, in a mean square error sense, the output of the model or model prediction,  $\hat{x}_i$ , and the data,  $x_i$ . For example, one metric for estimating the parameters of a model,  $S$ , is given by minimizing the sum of squared errors between the model prediction and the data

$$S = \sum_{i=1}^n \varepsilon_i^2 = \sum_{i=1}^n (x_i - \hat{x}_i)^2$$

where  $\varepsilon_i$  is the error between the data  $x_i$  and the model prediction  $\hat{x}_i$ . This technique provides an unbiased estimate with close correspondence between the model prediction and the data.

In order to provide a feeling for the modeling process described in [Figure 13.1](#), this chapter focuses on one particular system—the fast eye movement system—the modeling of which began with early muscle modeling experiences in the 1920s and continues today with neural network models for the control of the fast eye movement system. This physiological system is probably the best understood of all systems in the body. Some of the reasons for this success are the relative ease in obtaining data, the simplicity of the system in relation to others, and the lack of feedback during dynamic changes in the system. In this chapter, a qualitative description of the fast eye movement system is presented, followed by the first model of the system by Westheimer, who used a second-order model published in 1954. The 1964 model of the system by Robinson is next presented because of its fundamental advances in describing the input to the system. With the physical understanding of the system in place, a detailed presentation of muscle models is given with the early work of Levin and Wyman in 1927, and Fenn and Marsh in 1935. These muscle models are important in developing a realistic model that accurately depicts the system. Using the more accurate muscle models, the fast eye movement model is revisited by examining the model presented by Bahill and coworkers and then several models by Enderle and coworkers. Next, the control mechanism for this system is described from the basis of physiology, systems control theory, and neural networks based on anatomical pathways. Finally, the topic of system identification or parameter estimation closes the chapter. The literature on the fast eye movement system is vast, and the material covered in this chapter is not exhaustive but rather a representative sample from the field. Not covered in this chapter at all is how visual information is collected and processed by the body and how the body reacts to the information.

## 13.2 AN OVERVIEW OF THE FAST EYE MOVEMENT SYSTEM

The visual system is our most important sensory system. It provides a view of the world around us captured with receptors in the eyeball that is transmitted to the central nervous system (CNS). The eye movement or oculomotor system is responsible for movement of the

eyes so images are clearly seen. The oculomotor system also responds to auditory and vestibular sensory stimuli. A saccadic or fast eye movement involves quickly moving the eye from one image to another image. This type of eye movement is very common, and it is observed most easily while reading—that is, when the end of a line is reached, the eyes are moved quickly to the beginning of the next line. Saccades are also used to locate or acquire targets. Smooth pursuit is a slow eye movement used to track an object as it moves by keeping the eyes on the target. In addition to these two movements, the eye movement system also includes the vestibular ocular movement, optokinetic eye movement, and vergence movement. Vestibular ocular movements are used to maintain the eyes on the target during head movements. Optokinetic eye movements are reflex movements that occur when moving through a target-filled environment or to maintain the eyes on target during continuous head rotation. The optokinetic eye movement is a combination of saccadic and slow eye movements that keeps a full-field image stable on the retina during sustained head rotation. Each of these four eye movements is a conjugate eye movement—that is, movements of both eyes together driven by a common neural source. Vergence eye movements use non-conjugate eye movements to keep the eyes on the target. If the target moves closer, the eyes converge, and if the target moves farther away, they diverge. Each of these movements is controlled by a different neural system, and all of these controllers share the same final common pathway to the eye muscles.

Each eye can be moved within the orbit in three directions: vertically, horizontally, and torsionally. These movements are due to three pairs of agonist-antagonist muscles. These muscles are called antagonistic pairs because their activity opposes each other and follows the principle of reciprocal innervation. [Figure 13.2](#) shows the muscles of the eye, optic nerve, and the eyeball. We refer to the three muscle pairs and the eyeball as the oculomotor plant, and the oculomotor system as the oculomotor plant and the neural system controlling the eye movement system.

At the rear of the eyeball is the retina, shown in [Figure 13.3](#). Regardless of the input, the oculomotor system is responsible for movement of the eyes so images are focused on

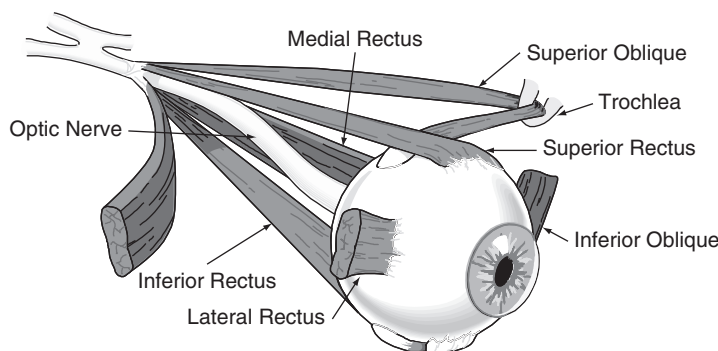


**FIGURE 13.2** The muscles, eyeball, and optic nerve of the right eye. The left eye is similar except the lateral and medial rectus muscles are reversed. The lateral and medial rectus muscles are used to move the eyes in a horizontal motion. The superior rectus, inferior rectus, superior oblique, and inferior oblique are used to move the eyes vertically and torsionally. The contribution from each muscle depends on the position of the eye. When the eyes are looking straight ahead, called primary position, the muscles are stimulated and under tension.

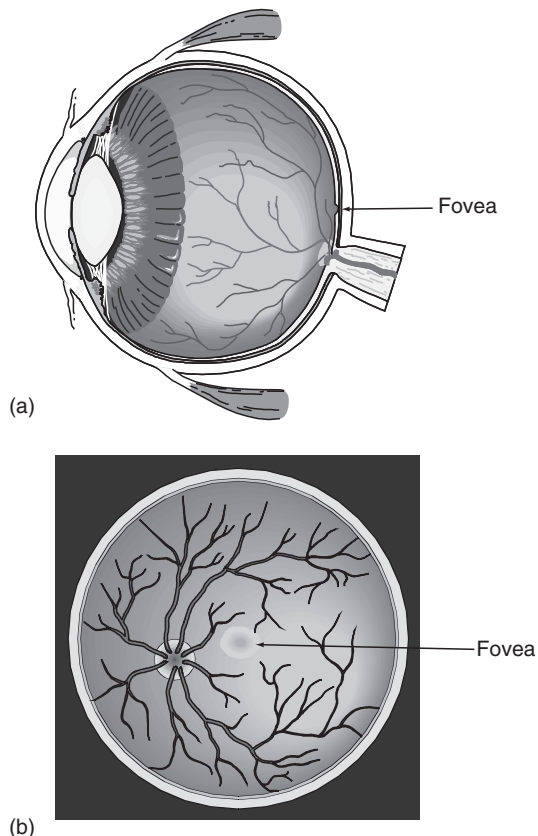


**FIGURE 13.3** (A) Side view of the eye. The rear surface of the eye is called the retina. The retina is part of the central nervous system and consists of two photoreceptors: rods and cones. (B) Front view looking at the rear inside surface (retina) of the eye. The fovea is located centrally and is approximately 1 mm in diameter. The oculomotor system maintains targets centered on the fovea.

the central one-half degree region of the retina, known as the fovea. Lining the retina are photoreceptive cells that translate images into neural impulses. These impulses are then transmitted along the optic nerve to the central nervous system via parallel pathways to the superior colliculus and the cerebral cortex. The fovea is more densely packed with photoreceptive cells than the retinal periphery—thus a higher-resolution image (or higher visual acuity) is generated in the fovea than the retinal periphery. The purpose of the fovea is to allow us to *clearly* see an object, and the purpose of the retinal periphery is to allow us to *detect* a new object of interest. Once a new object of interest is detected in the periphery, the system redirects the eyes to the new object.

One of the most successfully studied systems in the human is the oculomotor or eye movement system. Some of the reasons for this success are the relative ease in obtaining data, the simplicity of the system, and the lack of feedback during dynamic changes in the system. A saccade is a fast eye movement that involves quickly moving the eyes from

one target or image to another. The word *saccade* originated from the French word *saquer*, which means to jerk the reins of a horse. A saccade is a very quick and jerky movement of the eye from one target to another.

The eye muscles are among the fastest in the human body, with a 10° saccade taking only 50 ms. The saccadic system can be thought of as a targeting system that is concerned only with accurate and swift eye movements from one target to another without concern for the information swept across the retina during the eye movement. During a saccade, the visual system is turned off. After the saccade is complete, the system operates in a closed-loop mode to ensure that the eyes reached the correct destination. Information from the retina and muscle proprioceptors is used to correct any error between the desired and current eye position. The saccade system operates in a closed-loop mode to reduce this error to zero with a corrective saccade. One possible explanation of the operation of the neural control of saccades is that the saccadic neural controller is an open-loop time-optimal system using an internal closed-loop controller [11, 13, 16, 50]. This system does not rely on muscle proprioceptors or real time visual feedback to ensure accuracy of movement because the eye movements occur too fast. Instead, a complex neural network involving the mesencephalon, cerebellum, brainstem, and cerebrum keeps track of the eye movement.

A typical experiment for recording saccades has the subject sitting before a horizontal target display of small light emitting diodes (LEDs), as shown in Figure 13.4 (left). The subject is instructed to maintain their eyes on the lit LED by moving their eyes as fast as possible to avoid errors. A saccade is made by the subject when the active LED is switched off and another LED is switched on. Eye movements can be recorded using a variety of techniques, including electrooculography, video oculography, scleral search coil, and

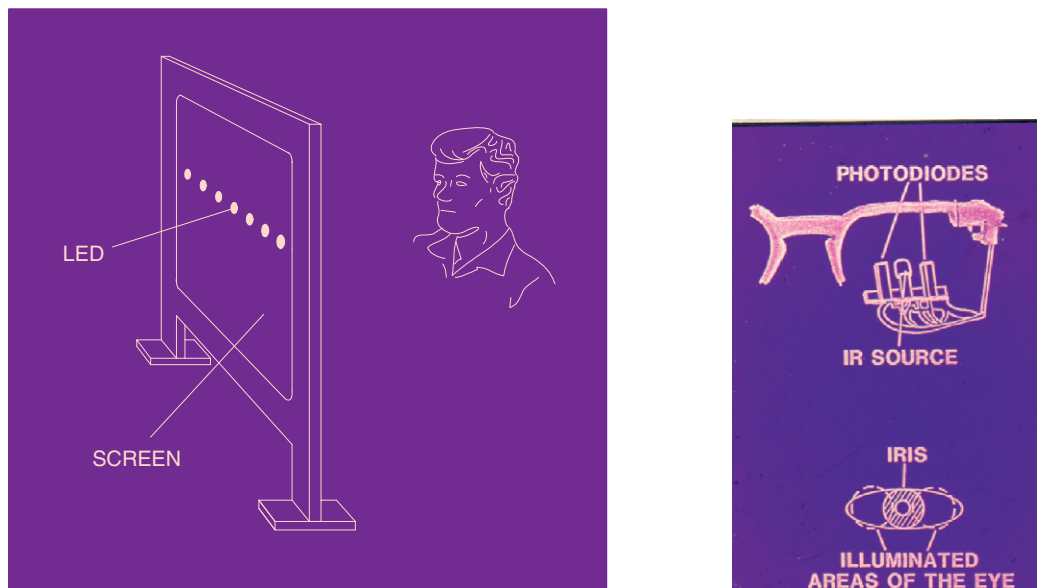


FIGURE 13.4 Experimental setup to record a saccade (left) and an infrared eye movement recorder (right). The eye movement recorder is based on the design by Engelken et al. [21].

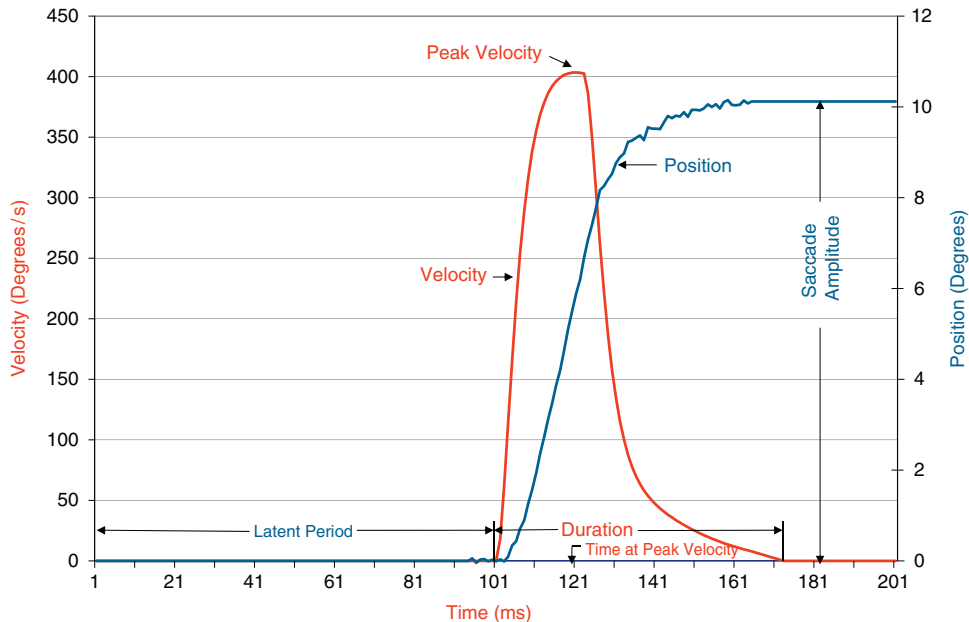


FIGURE 13.5 A  $10^\circ$  saccade with various indices labeled.

infrared oculography (shown in Figure 13.4 (right)). A typical saccade is shown in Figure 13.5, with a latent period of approximately 100 ms, amplitude of  $10^\circ$ , and a duration of approximately 60 ms. Saccadic eye movements are conjugate and ballistic, with a typical duration of 30–100 ms and a latency of 100–300 ms. The latent period is thought to be the time interval during which the CNS determines whether to make a saccade and, if so, calculates the distance the eyeball is to be moved, transforming retinal error into transient muscle activity. Also shown in this figure is the velocity of the saccade with a peak velocity of approximately  $400^\circ\text{s}^{-1}$ .

Generally, saccades are extremely variable, with wide variations in the latent period, time to peak velocity, peak velocity, and saccade duration. Furthermore, variability is well coordinated for saccades of the same size; saccades with lower peak velocity are matched with longer saccade durations, and saccades with higher peak velocity are matched with shorter saccade durations. Thus, saccades driven to the same destination usually have different trajectories.

To appreciate differences in saccade dynamics, it is often helpful to describe them with saccade main sequence diagrams [3, 17, 27]. The main sequence diagrams plot saccade peak velocity–saccade magnitude, saccade duration–saccade magnitude, and saccade latent period–saccade magnitude. The saccade size or amplitude is the angular displacement from the initial position to its destination. The size of a saccade ranges from less than a degree (microsaccades) to  $45^\circ$  in both the nasal (toward the nose) and temporal (toward the temple) directions. Peak or maximum velocity occurs at approximately half the duration of the saccade for small saccades less than  $15^\circ$  [2]. The duration of a saccadic eye movement is the time from the start to the end of a saccade. Duration is usually hard to determine

from the saccade amplitude versus time graph, but it is more easily seen in the velocity versus time graph, as shown in [Figure 13.5](#). Saccade durations can range from approximately 30 ms for saccades less than 5° and up to 100 ms for large saccades. For saccades greater than 7°, there is a linear relationship between saccade amplitude and duration. The latent period is the time interval from when a target appears until the eyes begin to move.

[Figure 13.6](#) shows the main sequence characteristics for a subject executing 26 saccades. The subject actually executed 52 saccades in both the positive and negative directions, with only the results of the saccades in the positive direction displayed in [Figure 13.6](#) for simplicity. Note that saccade characteristics moving to the left are different from those moving to the right. The solid lines in the figures include a fit to the data. Peak velocity–saccade magnitude is basically a linear function until approximately 15°, after which it levels off to a constant for larger saccades. Many researchers have fit this relationship to an exponential function. The line in graph (A) is fitted to the nonlinear equation

$$v_{\max} = \alpha \left(1 - e^{-\frac{x}{\beta}}\right) \quad (13.1)$$

where  $v_{\max}$  is the maximum velocity,  $x$  the saccade size, and the constants  $\alpha$  and  $\beta$  evaluated to minimize the summed error squared between the model and the data. Note that  $\alpha$  is to represent the steady-state peak velocity–saccade magnitude curve, and  $\beta$  is to represent the “time constant” for the peak velocity–saccade magnitude curve. For this data set for positive eye movements,  $\alpha$  equals 825, and  $\beta$  equals 9.3.

A similar pattern is observed with eye movements moving in the negative direction (not shown), but the parameters are  $\alpha = 637$  and  $\beta = 6.9$ , which are typically different from the values computed for the positive direction. The exponential shape of the peak velocity–saccade amplitude relationship might suggest that the system is nonlinear if a step input to the system is assumed. A step input provides a linear peak velocity–saccade amplitude relationship. In fact, the saccade system is not driven by a step input but rather a more complex pulse-step waveform, as discussed later. Thus, the saccade system cannot be assumed to be nonlinear solely based on the peak velocity–saccade amplitude relationship.

[Figure 13.6B](#) shows the data depicting a linear relationship between saccade duration–saccade magnitude. If a step input is assumed, then the dependence between saccade duration and saccade magnitude also might suggest that the system is nonlinear. A linear system with a step input always has a constant duration. Since the input is not characterized by a step waveform, the saccade system cannot be assumed to be nonlinear solely based on the saccade duration–saccade magnitude relationship.

[Figure 13.6C](#) shows the latent period–saccade magnitude data. It is quite clear that the latent period does not show any linear relationship with saccade size—that is, the latent period’s value appears independent of saccade size. However, some other investigators have proposed a linear relationship between the latent period and saccade magnitude. This feature is unimportant for the presentation in this book, since in the development of the oculomotor plant models, the latent period is implicitly assumed within the model.

Because of the complexity of the eye movement system, attention is restricted to horizontal fast eye movements. In reality, the eyeball is capable of moving horizontally, vertically, and torsionally. An appropriate model for this system would include a model for each muscle

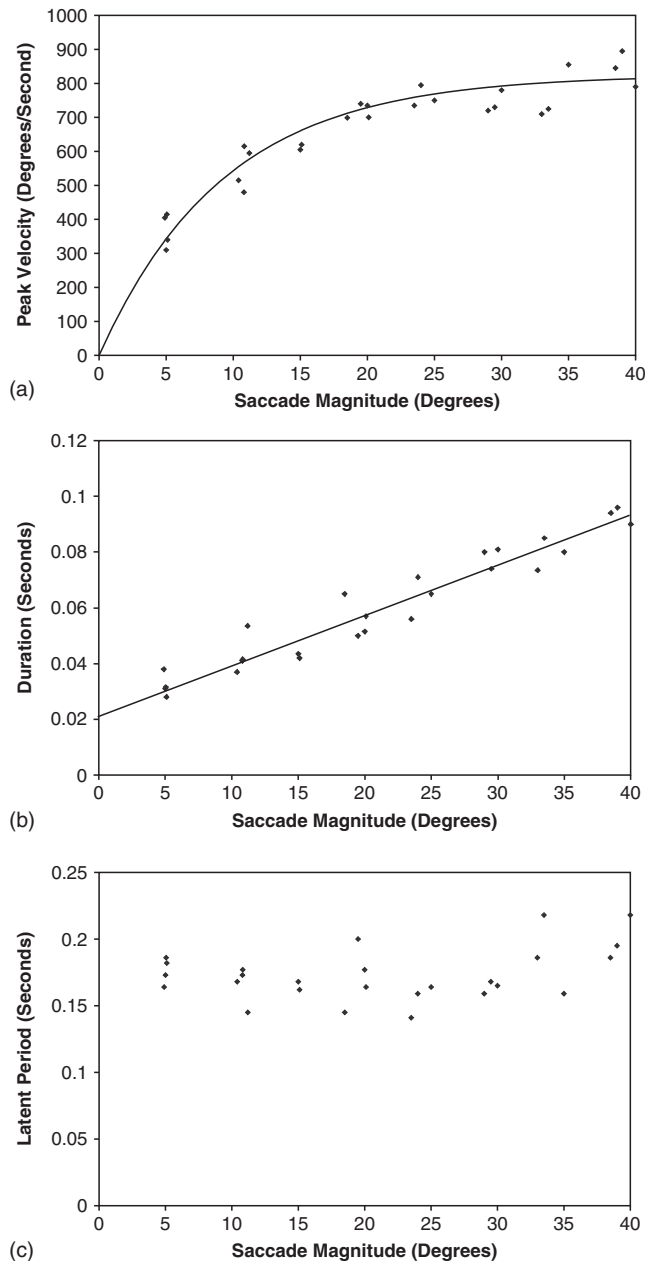


FIGURE 13.6 Main sequence diagrams for positive saccades. Similar shapes are observed for negative saccades. (a) Peak velocity–saccade magnitude, (b) saccade duration–saccade magnitude, and (c) latent period–saccade magnitude for 26 saccadic movements by a single subject. *Adapted from [9].*

and a separate controller for each muscle pair. The development of the horizontal saccadic eye movement models in this chapter are historical and are presented in increasing complexity with models of muscle introduced out of sequence so their importance is fully realized. Not every oculomotor model is discussed. A few are presented for illustrative purposes.

### 13.3 THE WESTHEIMER SACCADIC EYE MOVEMENT MODEL

The first quantitative saccadic eye movement model was published by Westheimer in 1954. In this model, he described horizontal saccades in response to a  $20^\circ$  target displacement. A mechanical description of the model is given in [Figure 13.7](#), and a system description is given in [Eq. \(13.2\)](#).

$$J\ddot{\theta} + B\dot{\theta} + K\theta = \tau(t) \quad (13.2)$$

To analyze the characteristics of this model and compare it to data, Laplace variable analysis is used. Assuming zero initial conditions, the Laplace transform of [Eq. \(13.2\)](#) yields

$$\theta(s^2J + sB + K) = \tau(s) \quad (13.3)$$

and as a transfer function in standard form

$$H(s) = \frac{\theta}{\tau} = \frac{1}{s^2J + sB + K} = \frac{\frac{\omega_n^2}{K}}{s^2 + 2\zeta\omega_n s + \omega_n^2} \quad (13.4)$$

where according to Westheimer's data for a  $20^\circ$  saccade,

$$\omega_n = \sqrt{\frac{K}{J}} = 120 \text{ and } \zeta = \frac{B}{2\sqrt{KJ}} = 0.7.$$

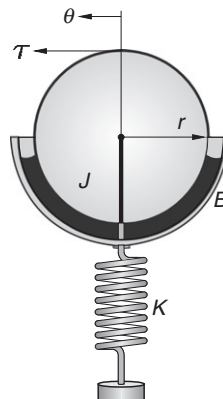


**FIGURE 13.7** Westheimer's second-order model of the saccade system. The parameters  $J$ ,  $B$ , and  $K$  are rotational elements for moment of inertia, friction, and stiffness, respectively, and represent the eyeball and its associated viscoelasticity. The torque applied to the eyeball by the lateral and medial rectus muscles is given by  $\tau(t)$ , and  $\theta$  is the angular eye position. The radius of the eyeball is  $r$ .

According to the data, the roots are complex and given by

$$s_{1,2} = -\zeta\omega_n \pm j\omega_n\sqrt{1-\zeta^2} = -84 \pm j85.7.$$

The input to this system is a step input  $\tau(s) = \frac{\gamma}{s}$ , and  $\theta(t)$  is determined as

$$\theta(t) = \frac{\gamma}{K} \left[ 1 + \frac{e^{-\zeta\omega_n t}}{\sqrt{1-\zeta^2}} \cos \left( \omega_n \sqrt{1-\zeta^2} t + \psi \right) \right] \quad (13.5)$$

where

$$\psi = \pi + \tan^{-1} \frac{-\zeta}{\sqrt{1-\zeta^2}}.$$

### EXAMPLE PROBLEM 13.1.

Show the intermediate steps in going from Eq. (13.4) to Eq. (13.5).

#### Solution

Substituting the input,  $\tau(s) = \frac{\gamma}{s}$ , into Eq. (13.4) yields

$$\theta(s) = \frac{\gamma \frac{\omega_n^2}{K}}{s(s^2 + 2\zeta\omega_n s + \omega_n^2)}$$

Assuming a set of complex roots based on the estimates from Westheimer, a partial fraction expansion gives

$$\theta(s) = \frac{\frac{\gamma}{K}}{s} + \frac{\frac{\gamma}{2K}[(\zeta^2 - 1) - j\zeta\sqrt{1-\zeta^2}]}{(s + \zeta\omega_n - j\omega_n\sqrt{1-\zeta^2})} + \frac{\frac{\gamma}{2K}[(\zeta^2 - 1) + j\zeta\sqrt{1-\zeta^2}]}{(s + \zeta\omega_n + j\omega_n\sqrt{1-\zeta^2})}$$

where the magnitude numerator of the complex terms is

$$M = \left| \frac{\gamma}{2K}[(\zeta^2 - 1) - j\zeta\sqrt{1-\zeta^2}] \right| = \frac{\gamma}{2K((\zeta^2 - 1)^2 + \zeta^2(1 - \zeta^2))^{\frac{1}{2}}} = \frac{\gamma}{2K(1 - \zeta^2)^{\frac{1}{2}}}$$

and the phase angle is

$$\phi = \tan^{-1} \frac{-\zeta\sqrt{1-\zeta^2}}{(\zeta^2 - 1)} = \tan^{-1} \frac{-\zeta\sqrt{1-\zeta^2}}{-(\sqrt{1-\zeta^2})^2} = \tan^{-1} \frac{-\zeta}{-\sqrt{1-\zeta^2}}$$

The solution is given by

$$\theta(t) = \frac{\gamma}{K} \left[ 1 + \frac{e^{-\zeta\omega_n t}}{\sqrt{1-\zeta^2}} \cos \left( \omega_n \sqrt{1-\zeta^2} t + \psi \right) \right]$$

*Continued*

where  $\psi = \pi + \tan^{-1} \frac{-\zeta}{\sqrt{1 - \zeta^2}}$ . It is always helpful to check analysis results and one easy point to check is usually at time zero.

$$\theta(0) = \frac{\gamma}{K} \left[ 1 + \frac{\cos(\phi)}{\sqrt{1 - \zeta^2}} \right] = \frac{\gamma}{K} \left[ 1 + \frac{-\sqrt{1 - \zeta^2}}{\sqrt{1 - \zeta^2}} \right] = 0$$

as it should, since the saccade starts at primary position or  $\theta(0) = 0$ .

To fully explore the quality of a model, it is necessary to compare its performance against the data. For a saccade, convenient metrics are time to peak overshoot, which gives an indication of saccade duration and peak velocity. These metrics were discussed previously when the main sequence diagram was described in [Section 13.2](#).

The time to peak overshoot of saccade model,  $T_p$ , is found by first calculating

$$\frac{\partial \theta}{\partial t} = \frac{\partial}{\partial t} \left[ \frac{\gamma}{K} \left( 1 + \frac{e^{-\zeta \omega_n t}}{\sqrt{1 - \zeta^2}} \cos \left( \omega_n \sqrt{1 - \zeta^2} t + \psi \right) \right) \right] \Big|_{t=T_p} = 0 \quad (13.6)$$

Using the chain rule to evaluate [Eq. \(13.6\)](#) and substituting  $t = T_p$ , yields

$$T_p = \frac{\pi}{\omega_d} = \frac{\pi}{\omega_n \sqrt{1 - \zeta^2}}. \quad (13.7)$$

With Westheimer's constants of  $\zeta = 0.7$  and  $\omega_n = 120$ , we find that  $T_p = \frac{\pi}{120 \times \sqrt{1 - 0.7^2}} = 37$  ms.  $T_p$  in the Westheimer model is independent of saccade size and not in agreement with experimental data presented in the main sequence diagram. The data show a saccade duration that increases with saccade amplitude, where this model has a constant duration.

### EXAMPLE PROBLEM 13.2

Show that [Eq. \(13.7\)](#) follows from [Eq. \(13.6\)](#). Find the value of  $\theta(T_p)$ .

#### Solution

From [Eq. \(13.6\)](#), we have

$$\frac{\gamma}{K \sqrt{1 - \zeta^2}} \left[ -\zeta \omega_n \cos(\omega_d T_p + \psi) e^{-\zeta \omega_n t} - \omega_d e^{-\zeta \omega_n t} \sin(\omega_d T_p + \psi) \right] = 0 \quad (13.8)$$

[Eq. \(13.8\)](#) is rewritten as

$$-\zeta \cos(\omega_d T_p + \psi) = \sqrt{1 - \zeta^2} \sin(\omega_d T_p + \psi)$$

which yields

$$\tan(\omega_d T_p + \psi) = \frac{-\zeta}{\sqrt{1 - \zeta^2}} = \tan \psi \quad (13.9)$$

[Eq. \(13.9\)](#) is true whenever  $\omega_d T_p = n\pi$ . The time to peak amplitude is the smallest value that satisfies [Eq. \(13.9\)](#), which is  $n = 1$ . Thus,  $T_p = \frac{\pi}{\omega_d} = \frac{\pi}{\omega_n \sqrt{1 - \zeta^2}}$ . To determine  $\theta(T_p)$ , note that  $\omega_d t + \psi = \pi + \psi$ , and

$$\begin{aligned}\theta(T_p) &= \frac{\gamma}{K} \left[ 1 + \frac{e^{-\frac{\zeta\pi}{\sqrt{1-\zeta^2}}}}{\sqrt{1-\zeta^2}} \cos(\pi + \psi) \right] \\ &= \frac{\gamma}{K} \left[ 1 + \frac{e^{-\frac{\zeta\pi}{\sqrt{1-\zeta^2}}}}{\sqrt{1-\zeta^2}} \times \sqrt{1-\zeta^2} \right] \\ &= \frac{\gamma}{K} \left( 1 + e^{\frac{-\pi\zeta}{\sqrt{1-\zeta^2}}} \right)\end{aligned}\quad (13.10)$$

An important aid in examining the suitability of a model is to study the model predictions and data estimates of higher-order derivatives. If there are problems with the model, these problems are amplified when comparing estimates of the higher-order derivatives with model predictions. For the Westheimer model, maximum velocity is found from  $\frac{\partial^2\theta}{\partial t^2} \Big|_{t=T_{mv}} = 0$ , where  $T_{mv}$  is the time at peak velocity. Using the solution given by [Eq. \(13.6\)](#), we next compute

$$\begin{aligned}\frac{\partial^2\theta}{\partial t^2} &= \frac{\partial}{\partial t} \left[ \frac{-\gamma}{K} \frac{e^{-\zeta\omega_n t}}{\sqrt{1-\zeta^2}} \{ \zeta\omega_n \cos(\omega_d t + \psi) + \omega_d \sin(\omega_d t + \psi) \} \right] \\ &= \frac{-\gamma}{K\sqrt{1-\zeta^2}} [-\zeta\omega_n e^{-\zeta\omega_n t} (\zeta\omega_n \cos(\omega_d t + \psi) + \omega_d \sin(\omega_d t + \psi)) \\ &\quad + e^{-\zeta\omega_n t} (-\zeta\omega_n \omega_d \sin(\omega_d t + \psi) + \omega_d^2 \cos(\omega_d t + \psi))] = 0\end{aligned}\quad (13.11)$$

After taking the second derivative in [Eq. \(13.11\)](#), we find that

$$T_{mv} = \frac{1}{\omega_d} \tan^{-1} \left( \frac{\sqrt{1-\zeta^2}}{\zeta} \right) \quad (13.12)$$

$\theta(T_{mv})$  can be evaluated using  $T_{mv}$ .

Using Westheimer's parameter values with any arbitrary saccade magnitude given by  $\Delta\theta = \frac{\gamma}{K}$  and Eq. (13.10) gives

$$\dot{\theta}(T_{mv}) = 55.02 \times \Delta\theta \quad (13.13)$$

Equation (13.13) indicates that peak velocity is directly proportional to saccade magnitude. As illustrated in the main sequence diagram shown in Figure 13.6, experimental peak velocity data have an exponential form and do not represent a linear function as predicted by the Westheimer model. Both Eqs. (13.7) and (13.13) are consistent with linear systems theory. That is, for a step input to a linear system, the duration (and time to peak overshoot) stays constant regardless of the size of the input, and the peak velocity increases with the size of the input.

### EXAMPLE PROBLEM 13.3

Show that Eq. (13.12) follows from (13.11).

#### Solution

Beginning with Eq. (13.11), we have

$$\begin{aligned} \frac{-\gamma}{K\sqrt{1-\zeta^2}} & [ -\zeta\omega_n e^{-\zeta\omega_n t} (\zeta\omega_n \cos(\omega_d t + \psi) + \omega_d \sin(\omega_d t + \psi)) \\ & + e^{-\zeta\omega_n t} (-\zeta\omega_n \omega_d \sin(\omega_d t + \psi) + \omega_d^2 \cos(\omega_d t + \psi)) ] = 0 \end{aligned}$$

The terms multiplying the sinusoids are removed, since they do not equal zero. Therefore,

$$(\omega_d^2 - \zeta^2\omega_n^2) \cos(\omega_d t + \psi) - 2\zeta\omega_n\omega_d \sin(\omega_d t + \psi) = 0$$

which reduces to

$$\frac{\omega_d^2 - \zeta^2\omega_n^2}{2\zeta\omega_n\omega_d} = \frac{\sin(\omega_d t + \psi)}{\cos(\omega_d t + \psi)} = \tan(\omega_d t + \psi) \quad (13.14)$$

Substituting  $\omega_d = \omega_n(1 - \zeta^2)$  into Eq. (13.14), we have

$$\frac{\omega_n^2(1 - \zeta^2) - \zeta^2\omega_n^2}{2\zeta\omega_n\omega_n(1 - \zeta^2)} = \frac{1 - 2\zeta^2}{2\zeta\sqrt{1 - \zeta^2}} = \tan(\omega_d t + \psi) \quad (13.15)$$

With  $\tan \psi = \frac{-\zeta}{\sqrt{1 - \zeta^2}}$ , we factor out  $\frac{-\zeta}{\sqrt{1 - \zeta^2}}$  in Eq. (13.15), substitute  $\tan \psi$ , giving

$$\frac{1 - 2\zeta^2}{2\zeta\sqrt{1 - \zeta^2}} = \frac{-\zeta}{\sqrt{1 - \zeta^2}} \left( 1 - \frac{1}{2\zeta^2} \right) = \left( 1 - \frac{1}{2\zeta^2} \right) \tan \psi = \tan(\omega_d t + \psi) \quad (13.16)$$

Now

$$\tan(\omega_d t + \psi) = \frac{\tan(\omega_d t) + \tan \psi}{1 - \tan(\omega_d t) \tan \psi} \quad (13.17)$$

and

$$\tan \phi = \tan \psi$$

Substituting for  $\tan(\omega_d t + \psi)$  from Eq. (13.17) into Eq. (13.16) gives

$$\left(1 - \frac{1}{2\zeta^2}\right) \tan \psi = \frac{\tan(\omega_d t) + \tan \psi}{1 - \tan(\omega_d t) \tan \psi} \quad (13.18)$$

Multiplying both sides of Eq. (13.18) by  $(1 - \tan \omega_d t \tan \psi)$  gives

$$\left(1 - \frac{1}{2\zeta^2}\right) \tan \psi - \left(1 - \frac{1}{2\zeta^2}\right) \tan(\omega_d t) (\tan \psi)^2 = \tan(\omega_d t) + \tan \psi \quad (13.19)$$

Collecting like terms in Eq. (13.19) gives

$$\tan(\omega_d t) \left(1 + (\tan \psi)^2 \left(1 - \frac{1}{2\zeta^2}\right)\right) = \frac{-\tan \psi}{2\zeta^2} \quad (13.20)$$

Dividing both sides of Eq. (13.20) by the term multiplying  $\tan(\omega_d t)$  gives

$$\tan(\omega_d t) = \frac{-\tan \psi}{2\zeta^2 \left(1 + (\tan \psi)^2 \left(\frac{2\zeta^2 - 1}{2\zeta^2}\right)\right)} = \frac{-\tan \psi}{2\zeta^2 + (\tan \psi)^2 (2\zeta^2 - 1)} \quad (13.21)$$

With  $\tan \psi = \tan \phi = \frac{-\zeta}{\sqrt{1 - \zeta^2}}$ , we have

$$\begin{aligned} \tan(\omega_d t) &= \frac{\frac{\zeta}{\sqrt{1 - \zeta^2}}}{2\zeta^2 + \frac{\zeta^2}{1 - \zeta^2} (2\zeta^2 - 1)} = \frac{\frac{\zeta}{\sqrt{1 - \zeta^2}}}{\zeta^2 \left(2 + \frac{(2\zeta^2 - 1)}{1 - \zeta^2}\right)} = \left(\frac{1 - \zeta^2}{1 - \zeta^2}\right) \frac{\frac{\zeta}{\sqrt{1 - \zeta^2}}}{\zeta^2 \left(2 + \frac{(2\zeta^2 - 1)}{1 - \zeta^2}\right)} \\ &= \frac{\sqrt{1 - \zeta^2}}{\zeta (2(1 - \zeta^2) + (2\zeta^2 - 1))} = \frac{\sqrt{1 - \zeta^2}}{\zeta} \end{aligned}$$

Taking the inverse tangent of the previous equation gives  $T_{mv} = \frac{1}{w_d} \tan^{-1} \left( \frac{\sqrt{1 - \zeta^2}}{\zeta} \right)$ .

Westheimer noted the differences between saccade duration–saccade magnitude and peak velocity–saccade magnitude in the model and the experimental data and inferred that the saccade system was not linear because the peak velocity–saccade magnitude plot was nonlinear. He also noted that the input was not an abrupt step function. Overall, this model provided a satisfactory fit to the eye position data for a saccade of 20° but not for saccades of other magnitudes. Interestingly, Westheimer's second-order model proves to be an adequate model for saccades of all sizes if a different input function, as described in the next section, is assumed. Due to its simplicity, the Westheimer model of the oculomotor plant is still popular today.

### EXAMPLE PROBLEM 13.4

Simulate a  $20^\circ$  saccade using the Westheimer saccade model. Plot position versus time.

#### Solution

The Laplace transform of the Westheimer saccade model with a step input is

$$\theta(s) = H(s)\tau(s) = \frac{\frac{\omega_n^2}{K}}{s^2 + 2\zeta\omega_n s + \omega_n^2} \times \frac{\gamma}{s}$$

and based on the model, the SIMULINK program is shown in [Figure 13.8](#) (top). Using the parameters given by Westheimer,  $\zeta = 0.7$  and  $\omega_n = 120$ , and the input  $\gamma = 20$ , the response is shown in [Figure 13.8](#) (bottom). Notice that the response is underdamped as expected and that  $T_p = 37$  ms.

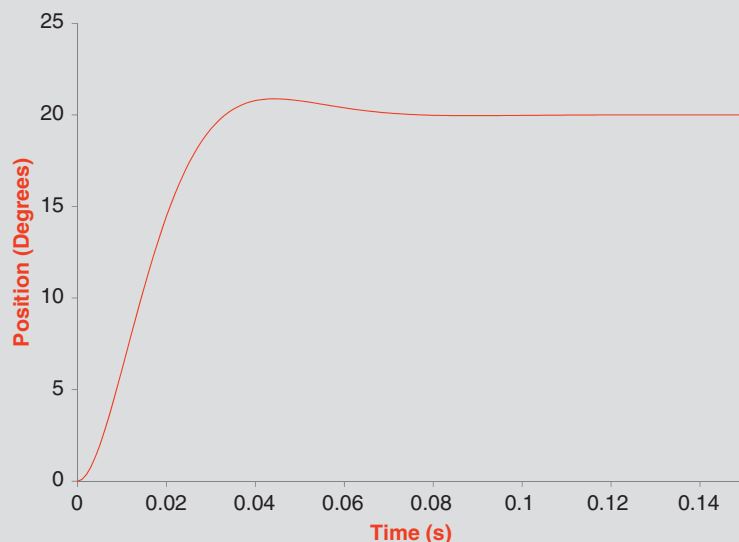
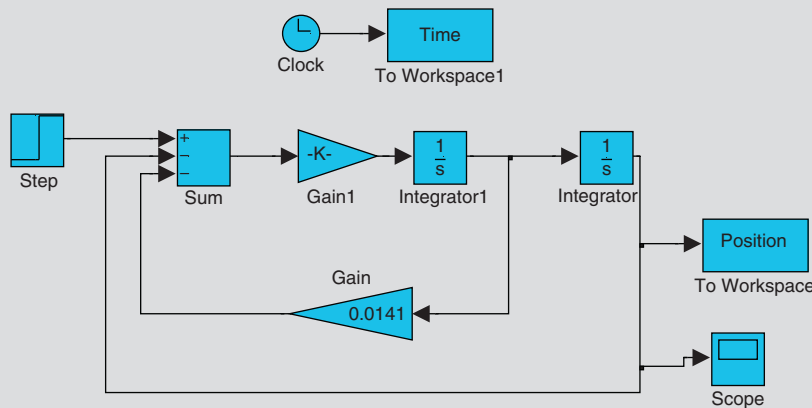


FIGURE 13.8 SIMULINK program and response for [Example Problem 13.4](#).

## 13.4 THE SACCADE CONTROLLER

One of the challenges in modeling physiological systems is the lack of data or information about the input to the system. For instance, in the fast eye movement system the input is the neurological signal from the CNS to the muscles connected to the eyeball. Information about the input is not available in this system, since it involves thousands of neurons firing at a very high rate. Recording the signal would involve invasive surgery and instrumentation that was not available in the 1960s. Often, however, it is possible to obtain information about the input via indirect means, as described in this section.

In 1964, Robinson performed an experiment in an attempt to measure the input to the eyeballs during a saccade. To record the input, one eye was held fixed using a suction contact lens, while the other eye performed a saccade from target to target. Since the same innervation signal is sent to both eyes during a saccade, Robinson inferred that the input, recorded through the transducer attached to the fixed eyeball, was the same input driving the other eyeball. He proposed that muscle tension driving the eyeballs during a saccade is a pulse plus a step or, simply, a pulse-step input (Figure 13.9).

Today, microelectrode studies are carried out to record the electrical activity in oculomotor neurons in monkeys. Figure 13.10 shows a micropipette being used to record the activity in the oculomotor nucleus, an important neuron population responsible for driving a saccade. Additional experiments on oculomotor muscle have been carried out to learn more about the saccade controller since Robinson's initial study. For instance in 1975, Collins and his coworkers reported using a miniature "C" gauge force transducer to measure muscle tension *in vivo* at the muscle tendon during unrestrained human eye movements. This type of study has allowed a better understanding of the tensions exerted by each muscle, rather than the combined effect of both muscles, as shown in Figure 13.11.

It is important to distinguish between the tension or force generated by a muscle, called muscle tension, and the force generator within the muscle, called the *active-state tension generator*. The active-state tension generator creates a force within the muscle that is transformed through the internal elements of the muscle into the muscle tension. Muscle tension is external and measurable. Active-state tension is internal and not measurable. Active-state tension

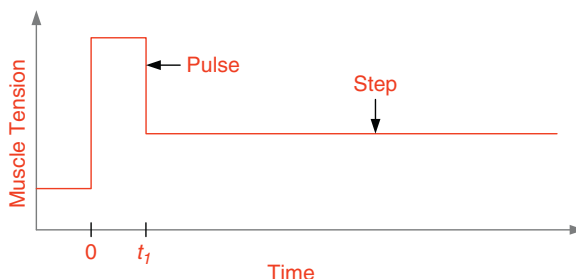
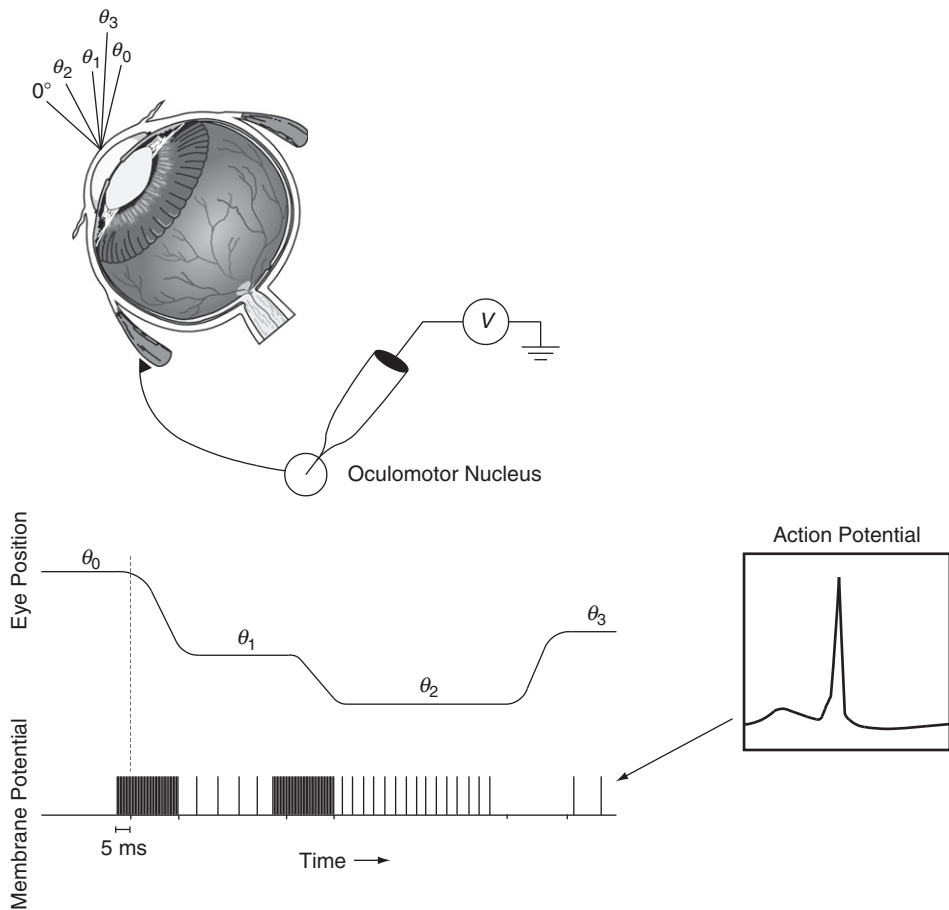


FIGURE 13.9 The muscle tension recorded during a saccade.



**FIGURE 13.10** Recording of a series of saccades using a micropipette and the resultant electrical activity in a single neuron. Spikes in the membrane potential indicate an action potential occurred. Saccade neural activity initiates with a burst of neural firing approximately 5 ms before the eye begins to move and continues until the eye has almost reached its destination. Relative position of the eye is shown at the top with angles  $\theta_0$  through  $\theta_3$ . Initially, the eye starts in position  $\theta_0$ , a position in the extremity in which the muscle is completely stretched with zero input. To move the eye from  $\theta_0$  to  $\theta_1$ , neural burst firing occurs. To maintain the eye at  $\theta_1$ , a steady firing occurs in the neuron. The firing rate for fixation is in proportion to the shortness of the muscle. Next, the eye moves from  $\theta_1$  to  $\theta_2$ . This saccade moves much more slowly than the first saccade with approximately the same duration as the first. The firing level is also approximately at the same level as the first. The difference in input corresponds to fewer neurons firing to drive the eye to its destination, which means a smaller input than the first saccade. Because the muscle is shorter after completing this saccade, the fixation firing rate is higher than the previous position at  $\theta_1$ . Next, the eye moves in the opposite direction to  $\theta_3$ . Since the muscle is lengthening, the input to the muscle is zero—that is, no action potentials are used to stimulate the muscle. The fixation firing level  $\theta_3$  is less than that for  $\theta_1$  because the muscle is longer.

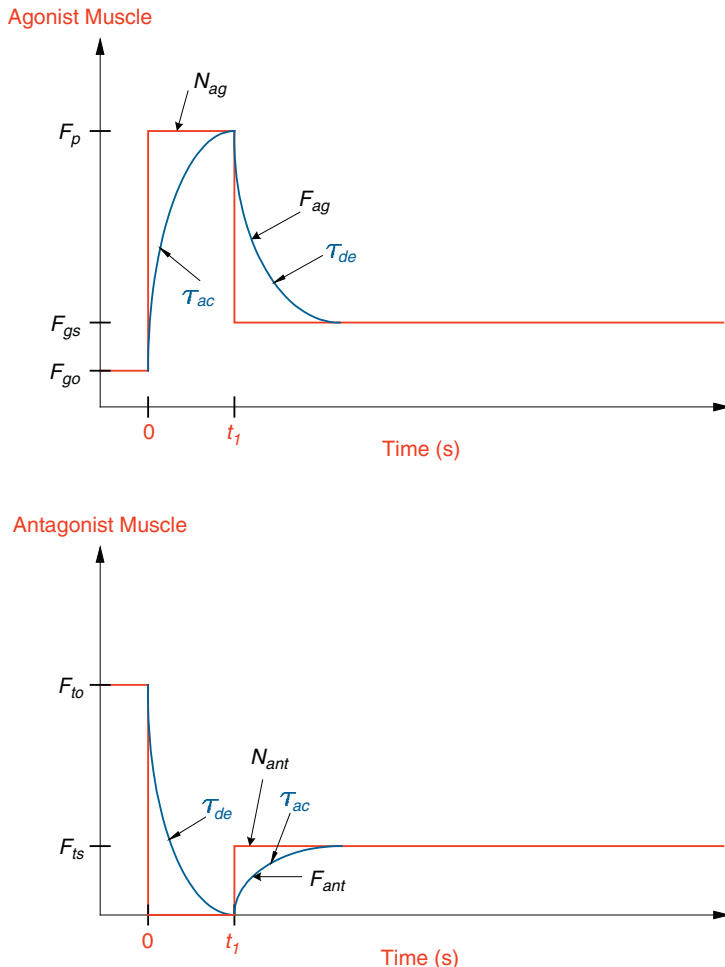


FIGURE 13.11 Agonist,  $N_{ag}$ , and antagonist,  $N_{ant}$ , control signals and the agonist,  $F_{ag}$ , and antagonist,  $F_{ant}$ , active-state tensions. Note that the time constant for activation,  $\tau_{ac}$ , is different from the time constant for deactivation,  $\tau_{de}$ . The time interval,  $t_1$ , is the duration of the pulse.

follows most closely the neural input to the muscle. From Figure 13.11, a pattern of neural activity is observed as follows:

1. The muscle that is being contracted (agonist) is stimulated by a pulse, followed by a step to maintain the eyeball at its destination.
2. The muscle that is being stretched (antagonist) is unstimulated during the saccade (stimulated by a pause or a negative pulse to zero), followed by a step to maintain the eyeball at its destination.

Figure 13.11 quantifies these relationships for the agonist neural input,  $N_{ag}$ , and the antagonist neural input,  $N_{ant}$ . The pulse input is required to get the eye to the target as soon

as possible, and the step is required to keep the eye at that location. It has been reported that the active-state tensions are not identical to the neural controllers but are described by low-pass filtered pulse-step waveforms. The active-state tensions,  $F_{ag}$  and  $F_{ant}$ , are shown in [Figure 13.11](#) with time-varying time constants  $\tau_{ac}$  and  $\tau_{de}$ . It is thought that the low-pass filtering involves the movement of  $\text{Ca}^{++}$  across the cell membrane.

Some investigators have reported a different set of time constants for the agonist and antagonist activity, and others have noted a firing frequency-dependent agonist activation time constant. Others suggest that the agonist activation time constant is a function of saccade magnitude. For simplicity in this chapter, activation and deactivation time constants are assumed to be identical for both agonist and antagonist activity. The parameters are defined as follows:

$F_{go}$  is the initial agonist active-state tension before the saccade starts

$F_P$  is the maximum agonist active-state tension

$F_{gs}$  is the steady-state agonist active-state tension after the saccade ends

$F_{to}$  is the initial antagonist active-state tension before the saccade starts

$F_{ts}$  is the steady-state antagonist active-state tension after the saccade ends

Generally, the pulse is used to get the eyeball to the target quickly, and the step is required to keep the eye at that location. The same innervation signal is sent to both eyes, and as a result, they move together. We call this a conjugate eye movement.

## 13.5 DEVELOPMENT OF AN OCULOMOTOR MUSCLE MODEL

It is clear that an accurate model of muscle is essential for the development of a model of the horizontal fast eye movement system that is driven by a pair of muscles (lateral and medial rectus muscles). In fact, the Westheimer model does not include any muscle model and relies solely on the inertia of the eyeball, friction between the eyeball and socket, and elasticity due to the optic nerve and other attachments as the elements of the model. In this section, the historical development of a muscle model is discussed as it relates to the oculomotor system. Muscle model research involves a broad spectrum of topics, ranging from the nano models that deal with the sarcomeres to macro models, in which collections of cells are grouped into a lumped parameter system and described with ordinary mechanical elements. Here the focus is on a macro, or lumped parameter model of the oculomotor muscle based on physiological evidence from experimental testing. The model elements, as presented, consist of an active-state tension generator (input), elastic elements, and viscous elements. Each element is introduced separately and the muscle model is incremented in each subsection. It should be noted that the linear muscle model presented in [Sections 13.7](#) and [13.8](#) completely revises the subsections before it. The earlier subsections are presented because of their historical significance and to appreciate the current muscle model.

### 13.5.1 Muscle Model Passive Elasticity

Consider the experiment of stretching an unexcited muscle and recording tension to investigate the passive elastic properties of muscle. The data curve shown in [Figure 13.12](#) is a typical recording of the tension observed in an eye rectus muscle. The tension required

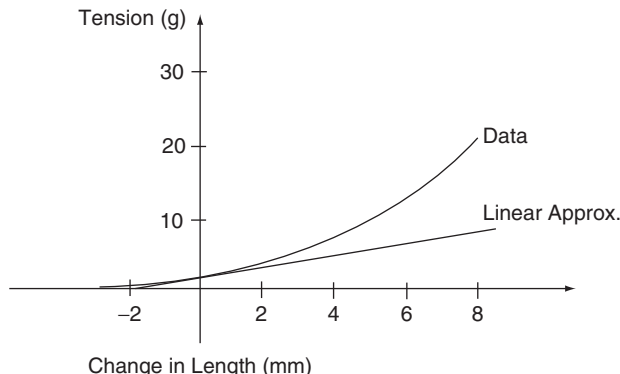


**FIGURE 13.12** The tension-displacement curve for unexcited muscle. The slope of the linear approximation to the data is muscle passive elasticity,  $K_{pe}$ .

to stretch a muscle is a *nonlinear* function of distance. Thus, in order to precisely model this element, a nonlinear spring element should be used. Note that the change in length at 0 refers to the length of the muscle at primary position (looking straight ahead). Thus, the eye muscles are stretched, approximately 3 mm, when the eye movement system is at rest in primary position. At rest, the muscle length is approximately 37 mm.

To be useful in a linear model of muscle, Figure 13.12 should be linearized in the vicinity of an operating point. The operating point should be somewhat centered in the region in which the spring operates. In Figure 13.12, a line tangent to the curve at primary position provides a linear approximation to the spring's behavior in this region as done historically. For ease in analysis, the following relationships hold for a sphere representing the eyeball radius of 11 mm.

$$1 \text{ g} = 9.806 \times 10^{-3} \text{ N}$$

$$1^\circ = 0.192 \text{ mm} = 1.92 \times 10^{-4} \text{ m}$$

The slope of the line,  $K_{pe}$ , is approximately

$$K_{pe} = 0.2 \frac{\text{g}}{\circ} = 0.2 \frac{\text{g}}{\circ} \times \frac{9.806 \times 10^{-3} \text{ N}}{1 \text{ g}} \times \frac{1^\circ}{1.92 \times 10^{-4} \text{ m}} = 10.2 \frac{\text{N}}{\text{m}}$$

and represents the elasticity of the passive elastic element.

The choice of the operating region is of vital importance concerning the slope of the curve. At this time, a point in the historical operating region of rectus muscle is used. In most of the oculomotor literature, the term  $K_{pe}$  is typically subtracted out of the analysis and is not used. The operating point will be revisited in Section 13.7, and this element will be completely removed from the model.

### 13.5.2 Active-State Tension Generator

In general, a muscle produces a force in proportion to the amount of stimulation. The element responsible for the creation of force is the active-state tension generator. Note that this

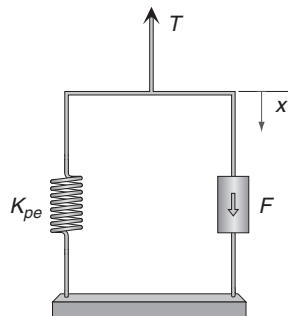


**FIGURE 13.13** A muscle model consisting of an active-state tension generator,  $F$ , and a passive elastic element,  $K_{pe}$ . Upon stimulation of the active-state tension generator, a tension,  $T$ , is exerted by the muscle.

terminology is used so there is no confusion with the force created within the muscle when the tension created by the muscle is discussed. The active tension generator is included along with the passive elastic element in the muscle model as shown in [Figure 13.13](#). The relationship between tension,  $T$ , active-state tension,  $F$ , and elasticity is given by

$$T = F - K_{pe}x \quad (13.21)$$

*Isometric* (constant length) experiments have been performed on humans over the years to estimate the active tension generator at different levels of stimulation. These experiments were usually performed in conjunction with strabismus surgery when muscles were detached and reattached to correct crossed eyes. Consider the tension created by a muscle when stimulated as a function of length as shown in [Figure 13.14](#). The data were collected from the lateral rectus muscle that was detached from one eyeball, while the other unoperated eyeball fixated at different locations in the nasal (N) and temporal (T) directions from  $-45^\circ$  to  $45^\circ$ . This experiment was carried out under the assumption that the same neural input is sent to each eyeball (Hering's Law of equal innervation), so the active-state tension in the freely moving eyeball should be the same as that in the detached lateral rectus muscle. At each fixation point, the detached lateral rectus muscle was stretched and tension data was recorded at each of the points indicated on the graph. The thick line represents the muscle tension at that particular eye position under normal conditions. The curve for  $45^\circ$  T is the zero stimulation case and represents the passive mechanical properties of muscle. Note that the tension generated is a *nonlinear* function of the length of the muscle.

To compare the model in [Figure 13.13](#) against the data in [Figure 13.14](#), it is convenient to subtract the passive elasticity in the data (represented by the  $45^\circ$  T curve) from each of the data curves  $30^\circ$  T through  $45^\circ$  N, leaving only the hypothetical active-state tension. Shown in the graph on the left in [Figure 13.15](#) is one such calculation for  $15^\circ$  N with the active-state tension given by the dashed line. The other curves in [Figure 13.14](#) give similar results and have been omitted because of the clutter. The dashed line should represent the active-state tension, which appears to be a function of length. If this was a *pure* active-state tension element, the subtracted curve should be a horizontal line indicative of the size of the input.

One such input is shown for the active-state tension in the graph on the right in [Figure 13.15](#). The result in [Figure 13.15](#) implies that either the active-state tension's effect

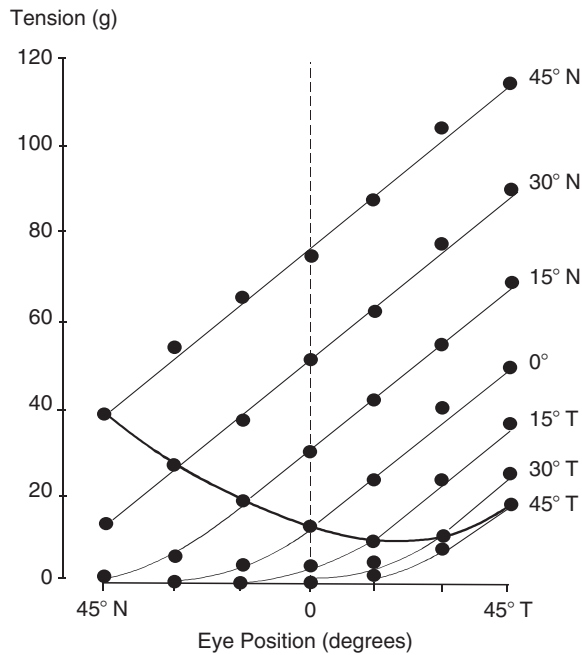


**FIGURE 13.14** Length-tension curves for lateral rectus muscle at different levels of activation. Dots represent tension data recorded from the detached lateral rectus muscle during strabismus surgery, while the unoperated eyeball fixated at targets from  $-45^\circ$  to  $45^\circ$ . Adapted from Collins et al. [8].

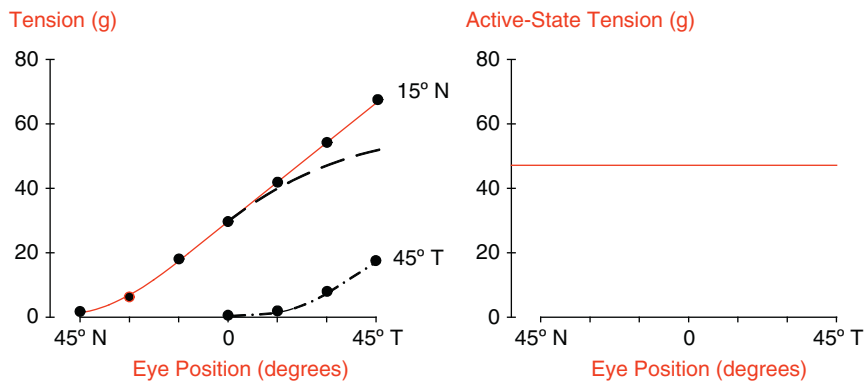


**FIGURE 13.15** (Left) Length-tension curves for extraocular muscle at two levels of activation corresponding to the  $15^\circ$  N and  $45^\circ$  T positions. The solid line represents tension data recorded from the detached lateral rectus muscle during strabismus surgery, while the unoperated eyeball fixated at targets. The dashed curve is the  $15^\circ$  curve with the  $45^\circ$  curve (dashed-dot line) subtracted from it. The resultant dashed curve represents the active-state tension as a function of eye position. (Right) The theoretical graph for active-state tension versus eye position as given by Eq. (3.4.1). Adapted from Collins et al. [8].

is a nonlinear element—that is, there may be other nonlinear or linear elements missing in the model—or, perhaps, some of the assumptions made in the development of the model are wrong. For the moment, consider that the analysis is correct and assume that some elements are missing. This topic will be revisited in [Section 13.7](#).

### 13.5.3 Elasticity

The normal operating point (at primary position),  $L_p$ , is much shorter than the length at which maximum force occurs at approximately  $30^\circ$ . Even when the effects of the passive muscle are removed, a relationship between length and tension is still evident, as previously described. Let us introduce a new elastic element into the model to account for the relationship between length and tension as shown in [Figure 13.16](#), which is described by the following equation.

$$T = F - K_{pe}x - Kx \quad (13.22)$$

The new elastic element,  $K$ , accounts for the slope of the subtracted curve shown as the dashed line in the graph on the left in [Figure 13.15](#). The slope of the line,  $K$ , at primary position, is approximately  $0.8 \text{ g}^\circ = 40.86 \text{ N/m}$  (a value typically reported in the literature). The slope for each of the curves in [Figure 13.14](#) can be calculated in the same manner at primary position with the resultant slopes all approximately equal to the same value as the one for  $15^\circ \text{ N}$ . At this time, the introduction of additional experiments will provide further insight to the development of the muscle model.

#### **Series Elastic Element**

Experiments carried out by Levin and Wyman in 1927 and Collins in 1975 indicated the need for a series elasticity element, in addition to the other elements previously presented in the muscle model. The experimental setup and typical data from the experiment are shown in [Figure 13.17](#). The protocol for this experiment, called the quick release experiment, is as follows. (1) A weight is hung onto the muscle. (2) The muscle is fully stimulated at time  $t_1$ . (3) The weight is released at time  $t_2$ . At time  $t_2$ , the muscle changes length almost instantaneously when the weight is released. The only element that can instantaneously change its length is a spring. Thus, to account for this behavior, a spring, called the series elastic element,  $K_{se}$ , is connected in series to the active-state tension element. While some

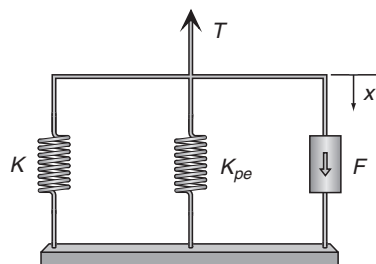


**FIGURE 13.16** A muscle model consisting of an active-state tension generator,  $F$ , passive elastic element,  $K_{pe}$ , and elastic element,  $K$ . Upon stimulation of the active-state tension generator, a tension  $T$  is exerted by the muscle.

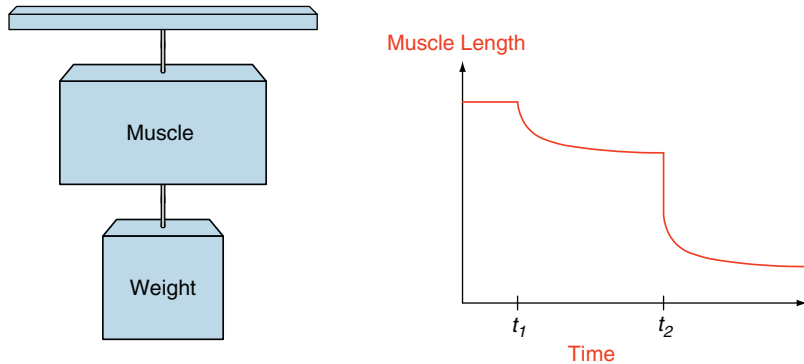


**FIGURE 13.17** The quick release experiment. The figure on the left depicts the physical setup of the experiment. The figure on the right shows typical data from the experiment. At time  $t_1$  the muscle is fully stimulated, and at time  $t_2$  the weight is released.

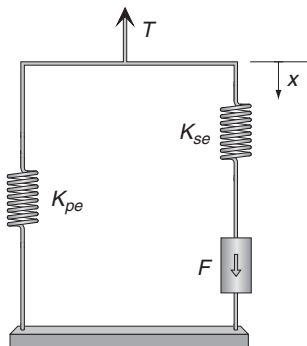


**FIGURE 13.18** A muscle model consisting of an active-state tension generator  $F$ , passive elastic element  $K_{pe}$  and series elastic element  $K_{se}$ . Upon stimulation of the active-state tension generator  $F$ , a tension  $T$  is exerted by the muscle.

investigators argue that this element is nonlinear, we will assume that it is linear for simplicity. The updated muscle model is shown in [Figure 13.18](#).

Based on the experiment carried out by Collins in 1975 on rectus eye muscle, an estimate for  $K_{se}$  was given as 125 N/m (2.5 gm/ $^{\circ}$ ). Since the value of  $K_{se}$  does not equal the value of  $K$ , another elastic element is needed to account for this behavior.

### Length Tension Elastic Element

Given the inequality between  $K_{se}$  and  $K$ , another elastic element, called the length-tension elastic element,  $K_{lt}$ , is placed in parallel with the active-state tension element as shown in the illustration on the left in [Figure 13.19](#). For ease of analysis,  $K_{pe}$  is subtracted out (removed) using the graphical technique shown in [Figure 13.15](#). To estimate a value for  $K_{lt}$ , the muscle model shown on the right in [Figure 13.19](#) is analyzed and reduced to an expression involving  $K_{lt}$ . Analysis begins by summing the forces acting on nodes 1 and 2.

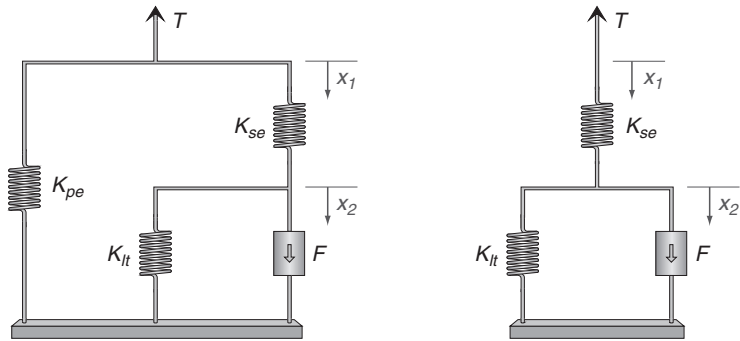


**FIGURE 13.19** Diagram on left illustrates a muscle model consisting of an active-state tension generator  $F$  in parallel to a length-tension elastic element  $K_{lt}$ , connected to a series elastic element  $K_{se}$ , all in parallel with the passive elastic element  $K_{pe}$ . Upon stimulation of the active-state tension generator  $F$ , a tension  $T$  is exerted by the muscle. The diagram on the right is the same muscle model except that  $K_{pe}$  has been removed.

$$T = K_{se}(x_2 - x_1) \quad (13.23)$$

$$F = K_{lt}x_2 + K_{se}(x_2 - x_1) \rightarrow x_2 = \frac{F + K_{se}x_1}{K_{se} + K_{lt}} \quad (13.24)$$

Substituting  $x_2$  from Eq. (13.24) into (13.23) gives

$$T = \frac{K_{se}}{K_{se} + K_{lt}}(F + K_{se}x_1) - K_{se}x_1 = \frac{K_{se}}{K_{se} + K_{lt}}F - \frac{K_{se}K_{lt}}{K_{se} + K_{lt}}x_1 \quad (13.25)$$

Equation (13.25) is an equation for a straight line with y-intercept  $\frac{K_{se}}{K_{se} + K_{lt}}F$  and slope  $\frac{K_{se}K_{lt}}{K_{se} + K_{lt}}$ . The slope of the length-tension curve in Figure 13.14 is given by  $K = 0.8 \text{ g/}^\circ = 40.86 \text{ N/m}$ . Therefore,

$$K = \frac{K_{se}K_{lt}}{K_{se} + K_{lt}} = 40.86 \frac{\text{N}}{\text{m}} \quad (13.26)$$

Solving Eq. (13.26) for  $K_{lt}$  yields

$$K_{lt} = \frac{K_{se}K}{K_{se} - K} = 60.7 \frac{\text{N}}{\text{m}} \quad (13.27)$$

### 13.5.4 The Force-Velocity Relationship

Early experiments indicated that muscle had elastic as well as viscous properties. Muscle was tested under isotonic (constant force) experimental conditions as shown in Figure 13.20 to investigate muscle viscosity. The muscle and load were attached to a lever with a high lever ratio. The lever reduced the gravity force (mass  $\times$  gravity) of the load at the muscle by one over the lever ratio, and the inertial force (mass  $\times$  acceleration) of the load by one over the lever ratio squared. With this arrangement, it was assumed that the inertial force exerted by the load during isotonic shortening could be ignored. The second assumption

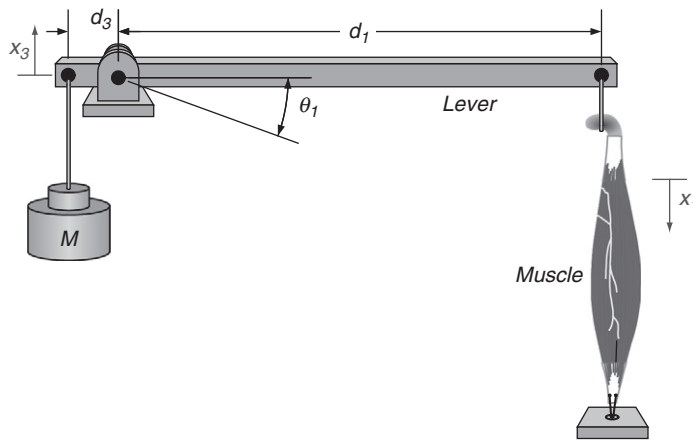


**FIGURE 13.20** Drawing of the classical isotonic experiment with inertial load and muscle attached to the lever. The muscle is stretched to its optimal length according to experimental conditions and attached to the ground.

was that if mass was not reduced enough by the lever ratio (enough to be ignored), then taking measurements at maximum velocity provided a measurement at a time when acceleration is zero, and, therefore, inertial force equals zero. If these two assumptions are valid, then the experiment would provide data free of the effect of inertial force as the gravity force is varied.

According to the experimental conditions, the muscle is stretched to its optimal length at the start of the isotonic experiment. The isotonic experiment begins by attaching a load  $M$ , stimulating the muscle, and recording position. The two curves in [Figure 13.21](#) depict the time course for the isotonic experiment for a small and large load. Notice that the durations of both responses are approximately equal regardless of the load, in spite of the apparent much longer time delay associated with the large load. Next, notice that the heavier the load, the less the total shortening. Maximum velocity is calculated numerically from the position data. To estimate muscle viscosity, this experiment is repeated with many loads at the same stimulation level, and maximum velocity is calculated. [Figure 13.22](#) illustrates the typical relationship between load ratio ( $P/P_o$ ) and maximum velocity, where  $P = Mg$

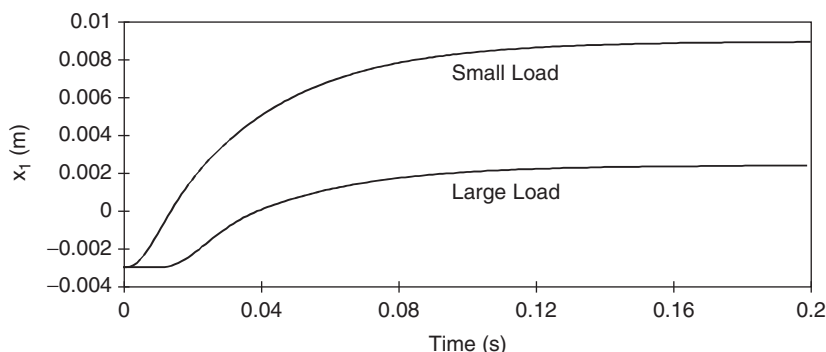


**FIGURE 13.21** The typical response of a muscle stimulated with a large and small load.

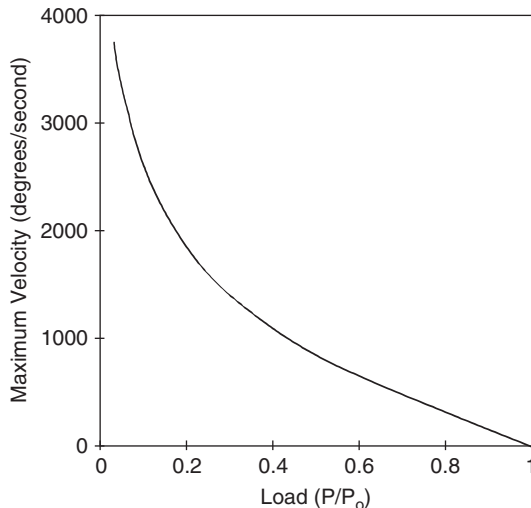


FIGURE 13.22 The force-velocity curve.

and  $P_o$  is the isometric tension (the largest weight that the muscle can move) for maximally stimulated muscle. This curve is usually referred to as the *force-velocity curve*.

Clearly, the force-velocity curve is nonlinear and follows a hyperbolic shape. If a smaller stimulus than maximum is used to stimulate the muscle, then a family of force-velocity curves results, as shown in Figure 13.23. Each curve is generated with a different active-state

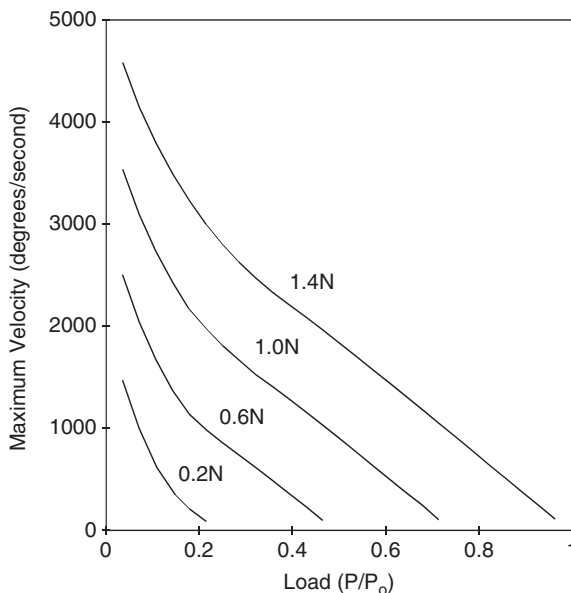
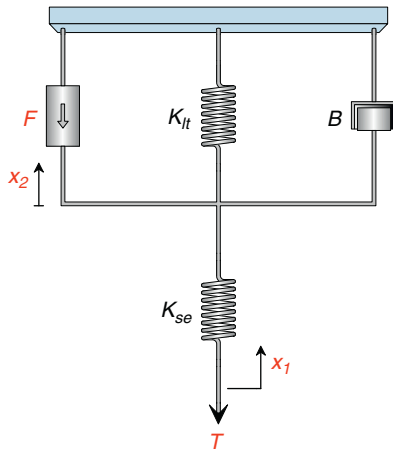


FIGURE 13.23 Family of force-velocity curves for active-state tensions ranging from 1.4 to 0.2 N.



**FIGURE 13.24** A muscle model consisting of an active-state tension generator  $F$ , in parallel with a length-tension elastic element  $K_{lt}$ , and viscous element  $B$ , connected to a series elastic element  $K_{se}$ . The passive elastic element  $K_{pe}$  has been removed from the model for simplicity. Upon stimulation of the active-state tension generator  $F$ , a tension  $T$  is exerted by the muscle.

tension as indicated. The force-velocity characteristics in Figure 13.23 are similar to those shown in Figure 13.22. In particular, the slope of the force-velocity curve for a small value of active-state tension is quite different from that for a large value of the active-state tension in the operating region of the eye muscle (i.e., approximately  $800^{\circ}/\text{s}$ ).

To include the effects of viscosity from the isotonic experiment in the muscle model, a viscous element is placed in parallel with the active-state tension generator and the length tension elastic element as shown in Figure 13.24. The impact of this element is examined by analyzing the behavior of the model in Example Problem 13.5 by simulating the conditions of the isotonic experiment. At this stage, it is assumed that the viscous element is linear in this example. For simplicity, the lever is removed along with the virtual acceleration term  $M\ddot{x}_1$ . A more thorough analysis including the lever is considered later in this chapter. For simplicity, the passive elastic element  $K_{pe}$  is removed from the diagram and analysis.

### EXAMPLE PROBLEM 13.5

Consider the system shown in Figure 13.25 that represents a model of the isotonic experiment. Assume that the virtual acceleration term  $M\ddot{x}_1$  can be ignored. Calculate and plot maximum velocity as a function of load.

#### Solution

Assume that  $\dot{x}_2 > \dot{x}_1$ , and that the mass is supported so  $x_1 > 0$ . Summing the forces acting on nodes 1 and 2 gives

*Continued*

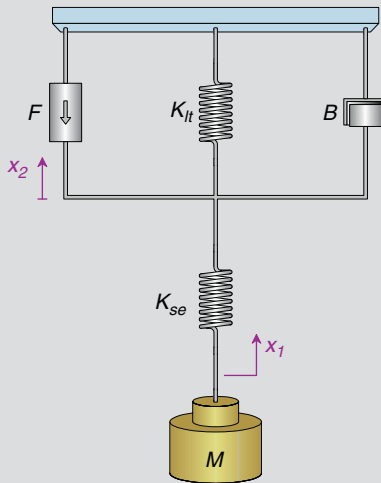


FIGURE 13.25 System for Example Problem 13.5.

$$Mg = K_{se}(x_2 - x_1) \rightarrow x_1 = x_2 - \frac{Mg}{K_{se}}$$

$$F = B\dot{x}_2 + K_{lt}x_2 + K_{se}(x_2 - x_1)$$

Substituting  $x_1$  into the second equation yields

$$F = B\dot{x}_2 + K_{lt}x_2 + Mg$$

Solving the previous equation for  $x_2$  and  $\dot{x}_2$  gives

$$x_2(t) = \frac{F - Mg}{K_{lt}} \left( 1 - e^{-\frac{K_{lt}t}{B}} \right)$$

$$\dot{x}_2(t) = \frac{F - Mg}{B} e^{-\frac{K_{lt}t}{B}}$$

Maximum velocity,  $V_{\max}$ , for all loads is given by  $V_{\max} = \frac{F - Mg}{B}$  and  $\dot{x}_1 = \dot{x}_2$ , since  $\dot{x}_1 = \frac{d}{dt} \left( x_2 - \frac{Mg}{K_{se}} \right)$ . Figure 13.26 depicts a linear relationship between maximum velocity and load.

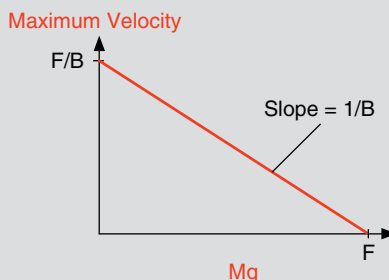


FIGURE 13.26 Result for Example Problem 13.5.

The assumption of a linear viscosity element appears to be in error, since the analysis in [Example Problem 13.5](#) predicts a linear relationship between load and maximum velocity (according to the assumptions of the solution), and the data from the isotonic experiment shown in [Figure 13.22](#) is clearly nonlinear. Thus, a reasonable assumption is that the viscosity element is nonlinear.

Traditionally, muscle viscosity is characterized by the nonlinear Hill hyperbola, given by

$$V_{\max}(P + a) = b(P_0 - P) \quad (13.28)$$

where  $V_{\max}$  is the maximum velocity,  $P$  is the external force,  $P_0$  the isometric tension, and  $a$  and  $b$  are the empirical constants representing the asymptotes of the hyperbola. As described previously,  $P_0$  represents the isometric tension, which is the largest weight that the muscle can move, and  $P$  is the weight  $Mg$ . Hill's data suggests that

$$a = \frac{P_0}{4} \quad \text{and} \quad b = \frac{V_{\max}}{4}$$

Therefore, with these values for  $a$  and  $b$ , the Hill equation is rewritten from [Eq. \(13.28\)](#) as

$$P = P_0 - \frac{V_{\max}(P_0 + a)}{b + V_{\max}} = P_0 - BV_{\max} \quad (13.29)$$

where

$$B = \frac{P_0 + a}{b + V_{\max}} \quad (13.30)$$

The term  $B$  represents the viscosity of the element. Clearly, the force due to viscosity is nonlinear due to the velocity term,  $V_{\max}$ , in the denominator of [Eq. \(13.29\)](#).

In oculomotor models,  $V_{\max}$  is usually replaced by  $\dot{x}_2$ ,  $P$  is replaced by muscle tension,  $T$ , and  $P_0$  is replaced by the active-state tension,  $F$ , as defined from [Figure 13.24](#). Therefore, [Eqs. \(13.29\)](#) and [\(13.30\)](#) are rewritten as

$$T = F - BV \quad (13.31)$$

where

$$B = \frac{F + a}{b + \dot{x}_2} \quad (13.32)$$

Some oculomotor investigators have reported values for  $a$  and  $b$  in the Hill equation that depend on whether the muscle is being stretched or contracted. There is some evidence to suggest that stretch dynamics are different from contraction dynamics. However, the form of the viscosity expression for muscle shortening or lengthening is given by [Eq. \(13.32\)](#), with values for  $a$  and  $b$  parameterized appropriately. For instance, Hsu and coworkers [33] described the viscosity for shortening and lengthening for oculomotor muscles as

$$B_{ag} = \frac{F_{ag} + AG_a}{\dot{x}_2 + AG_b} \quad (13.33)$$

$$B_{ant} = \frac{F_{ant} - ANT_a}{-\dot{x}_2 - ANT_b} \quad (13.34)$$

where  $AG_a$ ,  $AG_b$ ,  $ANT_a$ , and  $ANT_b$  are parameters based on the asymptotes for contracting (agonist) or stretching (antagonist), respectively.

### 13.5.5 A Linear Muscle Model

At this time, we will put all of the elements that have been discussed into a model of muscle as shown in Figure 13.27 (left), and then we will analyze this model to determine the tension created by the muscle. Note that in the muscle model, we have subtracted out the effects of passive elasticity and assumed that  $\dot{x}_2 > \dot{x}_1$ .

Thus, starting with the free body diagram in Figure 13.27 (right), we have our two node equations as

$$\begin{aligned} T &= K_{se}(x_2 - x_1) \\ F &= B\dot{x}_2 + K_{lt}x_2 + K_{se}(x_2 - x_1) \end{aligned}$$

We solve for  $x_2$  from the node 1 equation as  $x_2 = \frac{T}{K_{se}} + x_1$ , and we substitute it into the node 2 equation, giving us

$$F = B\dot{x}_2 + (K_{se} + K_{lt})x_2 - K_{se}x_1 = B\dot{x}_2 + K_{st}\left(\frac{T}{K_{se}} + x_1\right) - K_{se}x_1$$

For convenience, we will let  $K_{st} = K_{se} + K_{lt}$ , and we will multiply the previous equation by  $K_{se}$  and rearrange terms, so we have

$$K_{se}F = K_{se}B\dot{x}_2 + K_{st}T + K_{se}K_{lt}x_1$$

or

$$T = \frac{K_{se}F}{K_{st}} - \frac{K_{se}K_{lt}}{K_{st}}x_1 - \frac{K_{se}B}{K_{st}}\dot{x}_2$$

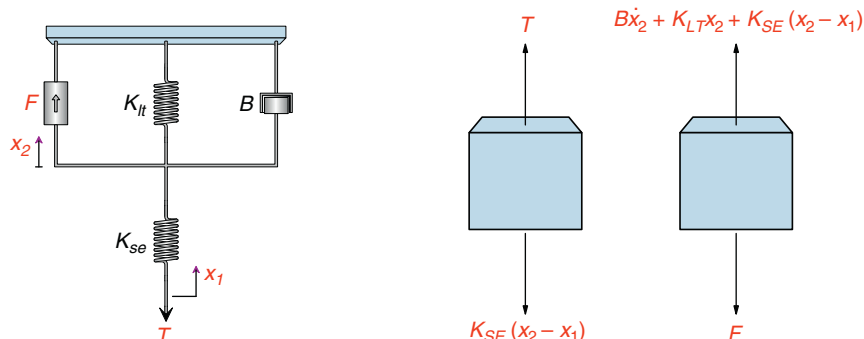


**FIGURE 13.27** (Left) Updated model of muscle with active-state tension generator, length-tension elastic element, series elastic element, and viscosity element. (Right) Free body diagram of the system on the left.

Equation (13.32) or Eqs. (13.33) and (13.34), depending on whether the muscle is contracting or lengthening, can be substituted for parameter  $B$  in the preceding equation to give a nonlinear model of oculomotor muscle.

### 13.5.6 Passive Tissues of the Eyeball

At this point, we return to modeling the eyeball. As previously discussed, Robinson not only described the passive properties of muscle, but he also determined the elasticity, viscosity, and inertia of the eyeball from his experiments during strabismus surgery. With the two horizontal muscles, Figure 13.28 describes the passive tissues of the eyeball. Note that the passive elasticity of the eyeball,  $K_p$ , is a combination of the effects due to the four other muscles, the optic nerve, and so on. The viscous element of the eyeball,  $B_p$ , is due to the friction of the eyeball within the eye socket.

### 13.5.7 Activation and Deactivation Time Constants

The control signal that the central nervous system sends to the oculomotor system during a saccade is a pulse-step signal as described in Figure 13.11. The signal the oculomotor system actually experiences is a low-pass filtered version of this signal. If we let  $C(s)$  = control signal,  $F(s)$  = active-state tension, and  $H(s)$  = low-pass filter, then

$$F(s) = C(s)H(s) = \frac{C(s)}{(s\tau + 1)}$$

where  $\tau$  is the low-pass filter time constant.

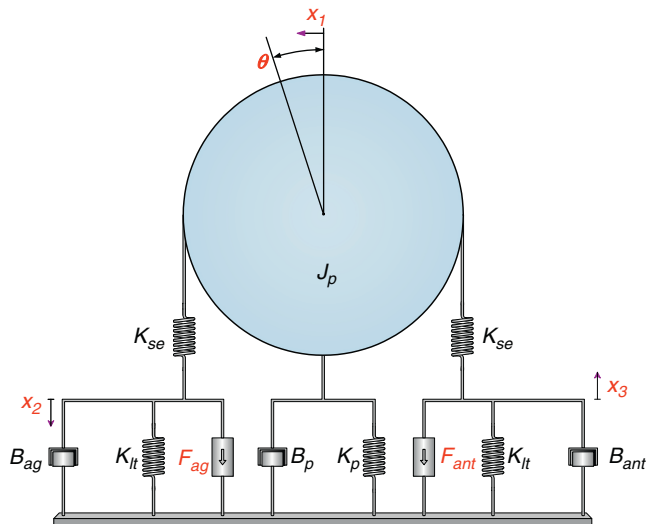


FIGURE 13.28 This model describes the two rectus muscles (agonist (ag) and antagonist (ant)), connected to the eyeball.  $\theta$  represents the angle that the eyeball is rotated, and  $x_1$  represents the length of arc rotated.

The agonist time constant reported by Bahill and coworkers [4] is a function of motoneuronal firing frequency; the higher the rate, the shorter the time constant. As explained, this is because large saccadic eye movements utilize fast muscle fibers and smaller saccadic eye movements utilize slow muscle fibers. There are two muscles involved with a horizontal eye movement: the agonist and the antagonist muscles. The agonist muscle forcibly contracts and moves the eyeball (fovea) to the target location. The antagonist muscle is completely inhibited during the pulse phase of the trajectory. Keep in mind that muscles are always under tension (tonic state at primary position) to avoid slack.

The control signal from the CNS to each muscle is a series of pulses or spikes due to the action potentials of the motoneurons, as illustrated in [Figure 13.10](#). This diagram illustrates a typical pattern observed during a series of fast eye movements in both horizontal directions. Notice that during a movement in the “on” direction (lateral), the rate of firing increases greatly; in the “off” direction (medial), the firing rate is zero. Also, notice that the burst firing starts approximately 5 ms before the saccade begins and that the longer the neurons fire, the larger the saccade. There is a large, nonconstant time delay between the time a target moves and when the eye actually starts to move. This is due to the CNS system calculating the forces necessary to bring the fovea to the target location. This movement is *ballistic* (not guided) to the extent that there are no known stretch receptors indicating muscle activity.

### **13.6 THE 1984 LINEAR RECIPROCAL INNERVATION SACCADIC EYE MOVEMENT MODEL**

---

Based on physiological evidence, Bahill and coworkers in 1980 presented a linear fourth-order model of the horizontal oculomotor plant that provides an excellent match between model predictions and horizontal eye movement data. This model eliminates the differences seen between velocity and acceleration predictions of the Westheimer and Robinson models, and the data. For ease in this presentation, the 1984 modification of this model by Enderle and coworkers is used. (A more thorough presentation of this model is given in Enderle, 2010a.)

In the previous analysis,  $B_{ag}$  and  $B_{ant}$  are nonlinear functions of velocity. We can linearize these functions by approximating the force-velocity family of curves with straight line segments as illustrated in [Figure 13.29](#). Antagonist activity is typically at the 5 percent level, and agonist activity is at the 100 percent level. Thus, we can assume that  $B_{ag}$  and  $B_{ant}$  are constants with different values, since the slopes are different in the linearization.

Using the linearized viscosity elements in our model of the eye movement system, we write the linear differential equation that describes saccades as a function of  $\theta$ . The updated model is shown in [Figure 13.30](#). The material presented here is based on the work published by Bahill and coworkers [4], and Enderle and coworkers [20].

To begin the analysis, we first draw the free body diagrams and write the node equations as shown in [Figure 13.31](#).

$$\text{Node 1: } rK_{se}(x_2 - x_1) - rK_{se}(x_4 - x_3) = J_p \ddot{\theta} + B_p \dot{\theta} + K_p \theta$$

$$\text{Node 2: } F_{ag} = B_{ag} \dot{x}_2 + K_{se}(x_2 - x_1) + K_{lt} x_2$$

$$\text{Node 3: } K_{se}(x_4 - x_3) = F_{ant} + K_{lt} x_3 + B_{ant} \dot{x}_3$$

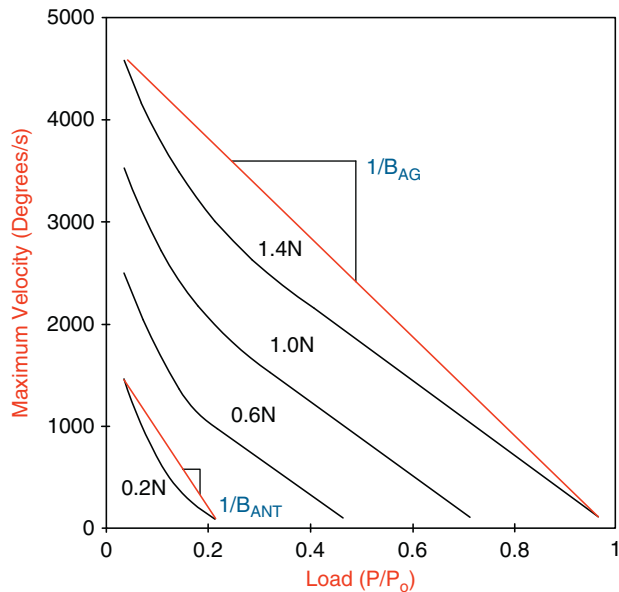


FIGURE 13.29 Linearization of nonlinear force-velocity curves.

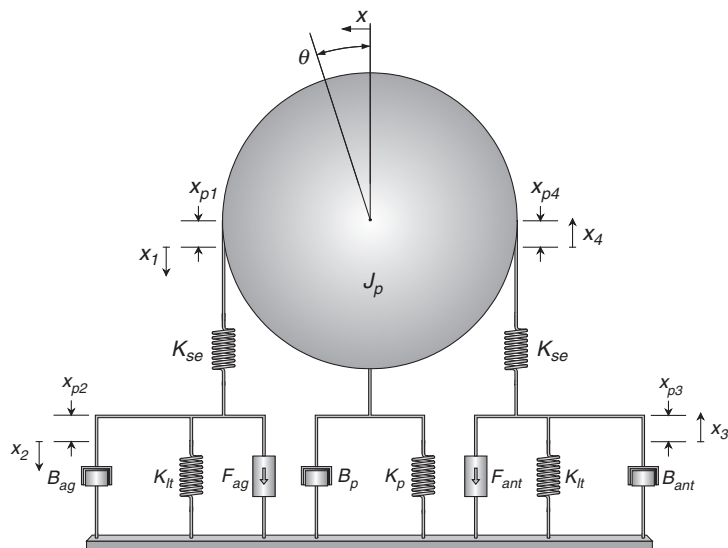


FIGURE 13.30 Linear eye movement model.

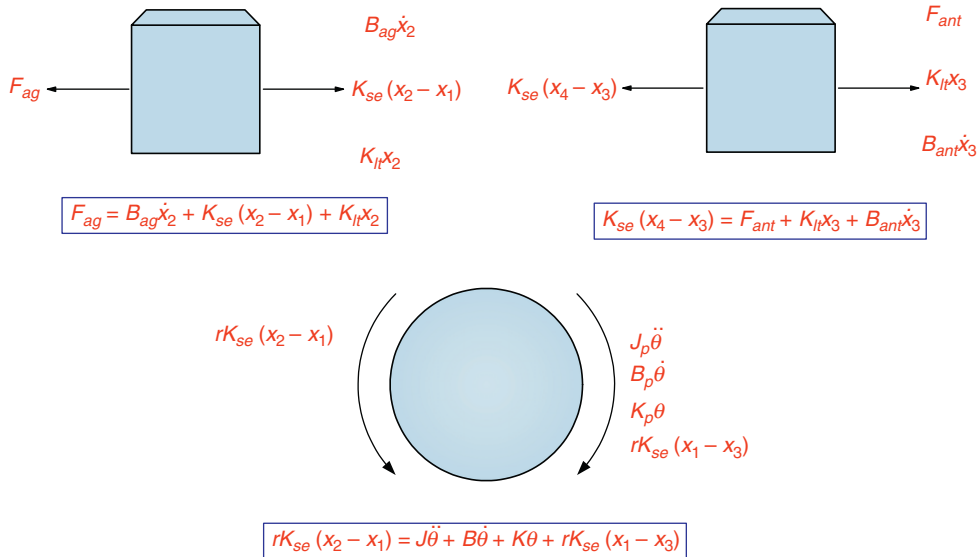


FIGURE 13.31 Free body diagrams for the system in Figure 13.30.

To solve for  $\theta$ , we use the Laplace transform analysis (details omitted here; see Enderle, 1984, or Enderle, 2010a).

$$\delta(K_{st}(F_{ag} - F_{ant}) + B_{ant}\dot{F}_{ag} - B_{ag}\dot{F}_{ant}) = \ddot{\theta} + C_3\ddot{\theta} + C_2\dot{\theta} + C_1\dot{\theta} + C_0\theta \quad (13.35)$$

where

$$J = \frac{J_p}{r} \times 5.2087 \times 10^3, \quad B = \frac{B_p}{r} \times 5.2087 \times 10^3, \quad K = \frac{K_p}{r} \times 5.2087 \times 10^3,$$

$$\theta = \frac{x}{r} \times \frac{180}{\pi} = 5.2087 \times 10^3 x, \text{ and } \delta = \frac{57.296 K_{se}}{r J B_{ant} B_{ag}}$$

$$C_3 = \frac{J K_{st} (B_{ag} + B_{ant}) + B B_{ant} B_{ag}}{J B_{ant} B_{ag}}$$

$$C_2 = \frac{J K_{st}^2 + B K_{st} (B_{ag} + B_{ant}) + B_{ag} B_{ant} (K + 2K_{se})}{J B_{ant} B_{ag}}$$

$$C_1 = \frac{B K_{st}^2 + (B_{ag} + B_{ant})(K K_{st} + 2K_{se} K_{st} - K_{se}^2)}{J B_{ant} B_{ag}}$$

$$C_0 = \frac{K K_{st}^2 + 2K_{se} K_{st} K_{lt}}{J B_{ant} B_{ag}}$$

The agonist and antagonist active-state tensions are given by the following low-pass filtered pulse-step waveforms and are illustrated along with their corresponding neurological control signals in [Figure 13.11](#).

$$\begin{aligned}
 F_{ag} &= F_{g0}u(-t) + \left( F_p + (F_{g0} - F_p)e^{\frac{-t}{\tau_{ac}}} \right) (u(t) - u(t - t_1)) \\
 &\quad + \left( F_{gs} + (F_p + (F_{g0} - F_p))e^{\frac{-t_1}{\tau_{ac}}} - F_{gs} \right) e^{\frac{-(t-t_1)}{\tau_{de}}} u(t - t_1) \\
 F_{ant} &= F_{t0}u(-t) + F_{t0}e^{\frac{-t}{\tau_{de}}} (u(t) - u(t - t_1)) \\
 &\quad + \left( F_{ts} + \left( F_{t0}e^{\frac{-t_1}{\tau_{de}}} - F_{ts} \right) e^{\frac{-(t-t_1)}{\tau_{ac}}} \right) u(t - t_1)
 \end{aligned} \tag{13.36}$$

where

- $F_{g0}$  = initial magnitude of the agonist active-state tension
- $F_p$  = pulse magnitude of the agonist active-state tension
- $F_{gs}$  = step magnitude of the agonist active-state tension
- $F_{t0}$  = initial magnitude of the antagonist active-state tension
- $F_{ts}$  = step magnitude of the antagonist active-state tension
- $\tau_{ac}$  = activation time constant
- $\tau_{de}$  = deactivation time constant
- $t_1$  = duration of the agonist pulse active-state tension

Final parameter estimates for the saccadic eye movement model are found using the system identification technique, a frequency response method. The oculomotor system operates in an open-loop mode while executing a saccade. After completing the saccade, the central nervous system operates in a closed-loop mode and compares eye and target position [5]. [Figure 13.32](#) presents a block diagram illustrating the open-loop, closed-loop operation of the oculomotor system, with the feedback element H operating only during discrete time intervals when a saccade is not being executed. The system identification is used to estimate the parameters and the input during the open-loop mode of the saccade.

The steady-state active-state tensions are given by

$$\begin{aligned}
 F_{ag} &= \begin{cases} 0.14 + 0.0185\theta & \text{N for } \theta < 14.23^\circ \\ 0.0283\theta & \text{N for } \theta \geq 14.23^\circ \end{cases} \\
 F_{ant} &= \begin{cases} 0.14 - 0.0098\theta & \text{N for } \theta < 14.23^\circ \\ 0 & \text{N for } \theta \geq 14.23^\circ \end{cases}
 \end{aligned} \tag{13.37}$$

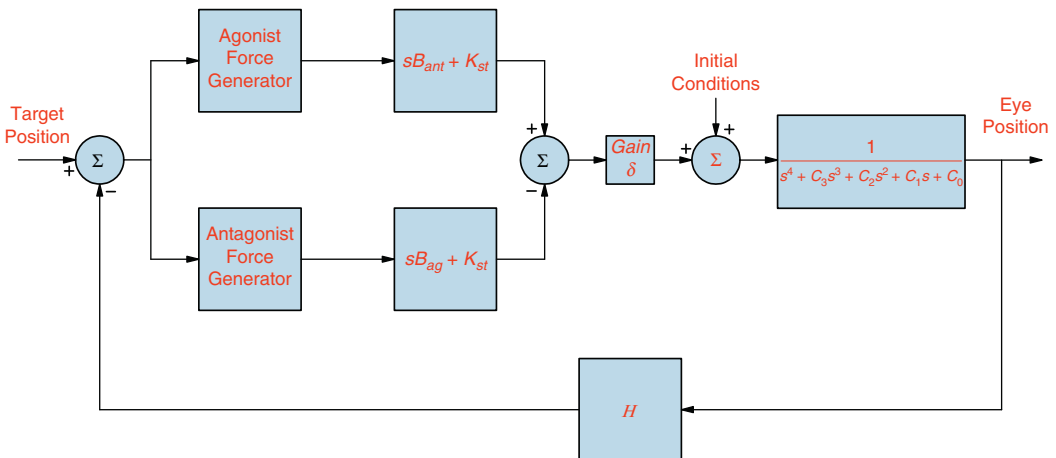


FIGURE 13.32 Block diagram of the modified linear homeomorphic eye movement model in Eq. (13.35).

A set of parameter estimates for the oculomotor plant from the system identification technique are

$$K_{se} = 125 \text{ Nm}^{-1}$$

$$K_{lt} = 32 \text{ Nm}^{-1}$$

$$K = 66.4 \text{ Nm}^{-1}$$

$$B = 3.1 \text{ Nsm}^{-1}$$

$$J = 2.2 \times 10^{-3} \text{ Ns}^2 \text{ m}^{-1}$$

$$B_{ag} = 3.4 \text{ Nsm}^{-1}$$

$$B_{ant} = 1.2 \text{ Nsm}^{-1}$$

$$\tau_{ac} = 0.009 \text{ s}$$

$$\tau_{de} = 0.0054 \text{ s}$$

$$\delta = 5.80288 \times 10^5$$

The eigenvalues for the oculomotor plant using the parameter values above are  $-15$ ,  $-66$ ,  $-173$ , and  $-1,293$ .

Figure 13.33 shows estimation routine results for a  $15^\circ$  target displacement. The accuracy of these results is typical for all target displacements with all subjects tested, except for saccades with glissadic or dynamic overshoot (saccades with glissadic or dynamic overshoot are discussed later in this chapter). Figures 13.34 and 13.35 further illustrate the accuracy of the system identification technique parameter estimation routine by the close agreement of the velocity and acceleration estimates with the two-point central differences estimates.

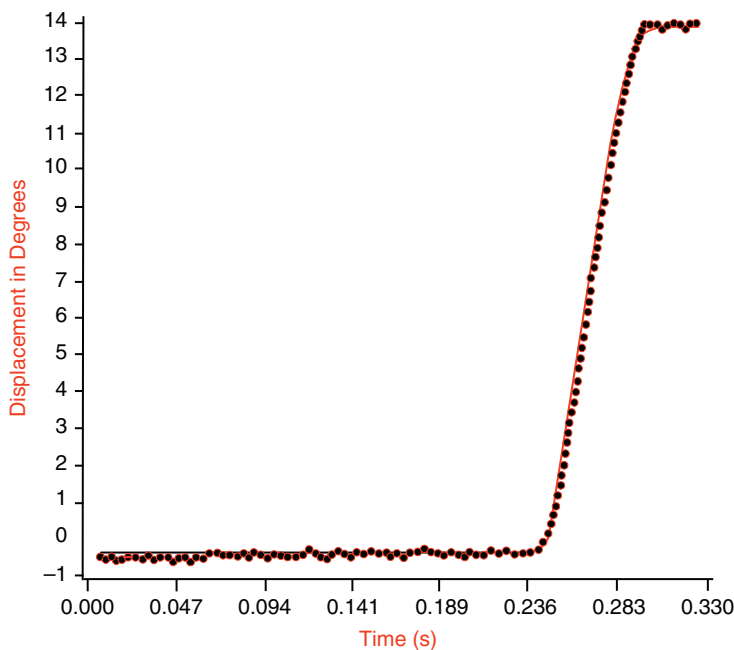


FIGURE 13.33 Response for a 15-degree saccadic eye movement. The solid line shows the predictions of the saccadic eye movement model, with final parameter estimates computed using the system identification technique. Dots are the data.

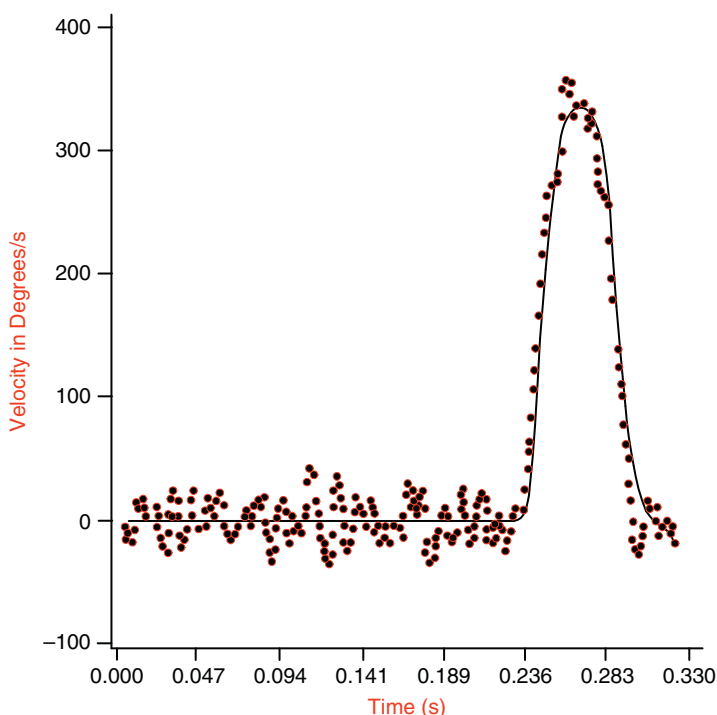
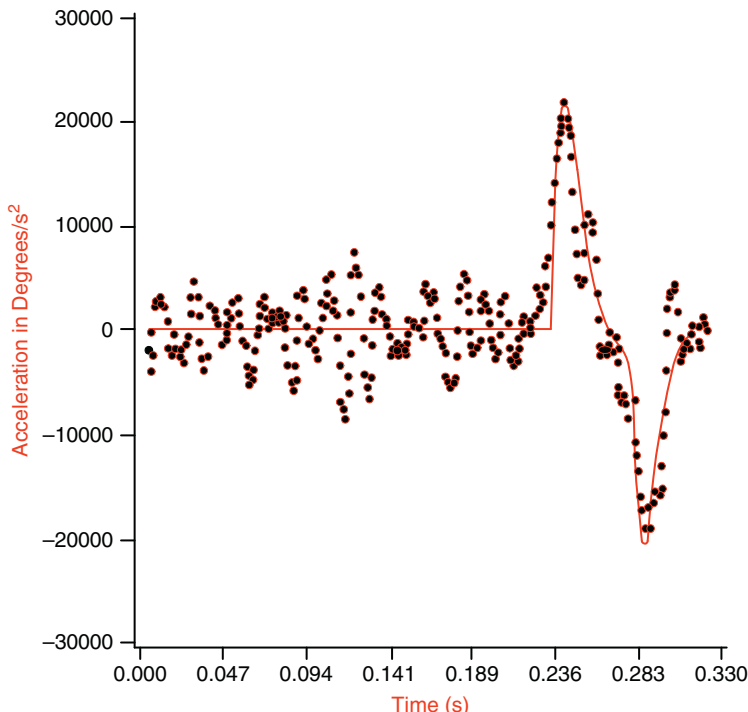


FIGURE 13.34 A plot of the velocity estimates (dots) and velocity simulation results (solid line) from the modified linear homeomorphic model.



**FIGURE 13.35** A plot of the acceleration estimates (dots) and acceleration simulation results (solid line) from the modified linear homeomorphic model.

### EXAMPLE PROBLEM 13.6

Using the oculomotor plant model described with Eq. (13.35) and the following parameters, simulate a 20° saccade.

$$\begin{aligned}
 K_{se} &= 125 \text{ Nm}^{-1}, K_{lt} = 32 \text{ Nm}^{-1}, K = 66.4 \text{ Nm}^{-1}, B = 3.1 \text{ Nsm}^{-1}, J = 2.2 \times 10^{-3} \text{ Ns}^2\text{m}^{-1} \\
 B_{ag} &= 3.4 \text{ Nsm}^{-1}, B_{ant} = 1.2 \text{ Nsm}^{-1}, \tau_{ac} = 0.009 \text{ s}, \tau_{de} = 0.0054 \text{ s}, \delta = 5.80288 \times 10^5, \\
 F_p &= 1.3 \text{ N}, t_1 = 31 \text{ ms}, \text{Latent Period} = 150 \text{ ms}.
 \end{aligned}$$

Plot the neural inputs, agonist and antagonist active-state tension, position, velocity, and acceleration versus time.

#### Solution

Using the given parameter values, the following m-file provides the parameter values for the SIMULINK program.

```
Fp=1.3
t1=.031
theta=20
```

```
theta0=0
TDE=.0054
TAC=.009
tdeinv=1/TDE
tacinv=1/TAC
KSE=125
KLT=32
K=66.4
B=3.1
J=2.2 * 10^-3
BAG=3.4
BANT=1.2
DELTA=5.80261*10^5
KST=KLT+KSE
C0=((K*KST^2)+(2*KSE*KST*KLT))/(J*BANT*BAG)
C1=((B*KST^2)+(BAG+BANT)*((K*KST)+(2*KSE*KST)-KSE^2))/(
(J*BANT*BAG))
C2=((J*KST^2)+((B*KST)*(BAG+BANT))+((BANT*BAG)*(K+(2*KSE))))/(
(J*BANT*BAG))
C3=((J*KST)*(BAG+BANT))+(B*BANT*BAG)/(J*BANT*BAG)
if theta0 < 14.23
    Fag0=0.14+0.0185*theta0
else
    Fag0=0.0283*theta0
end
if theta0 < 14.23
    Fant0=0.14-0.0098*theta0
else
    Fant0=0
end
if theta < 14.23
    Fagss=0.14+0.0185*theta
else
    Fagss=0.0283*theta
end
if theta < 14.23
    Fantss=0.14-0.0098*theta
else
    Fantss=0
end
latent=.15
sstart=latent+t1
agstep=Fp-Fagss
```

*Continued*

Figure 13.36 shows the SIMULINK program. The main program is shown in Figure 13.36 (a), based on Eq. (13.35). The input to the system is shown in Figure 13.36 (b), and the agonist and antagonist inputs are shown in Figures 13.36(c) and (d). Figure 13.37 shows the plots of position, velocity, acceleration, agonist neural input and active-state tension, and antagonist neural input and active-state tension.

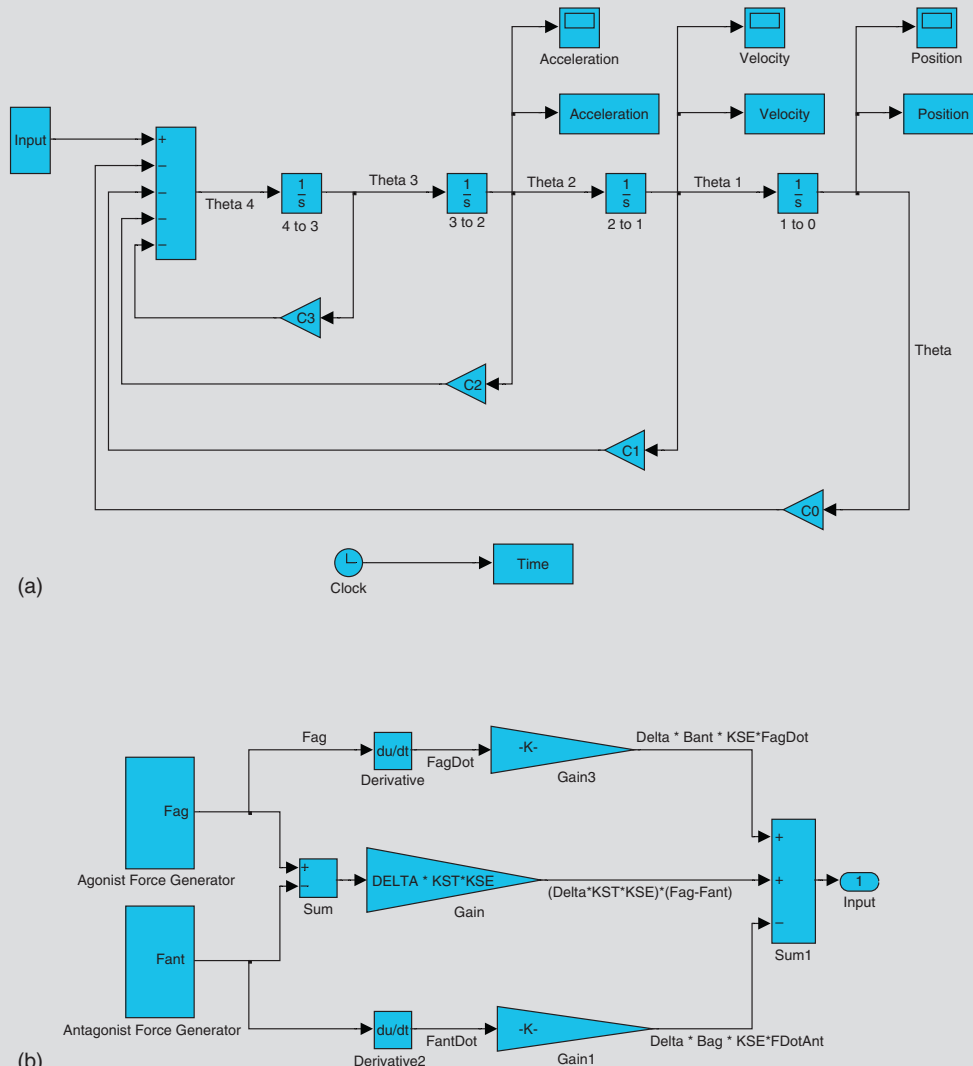


FIGURE 13.36 SIMULINK program for Example Problem 13.6.

*Continued*

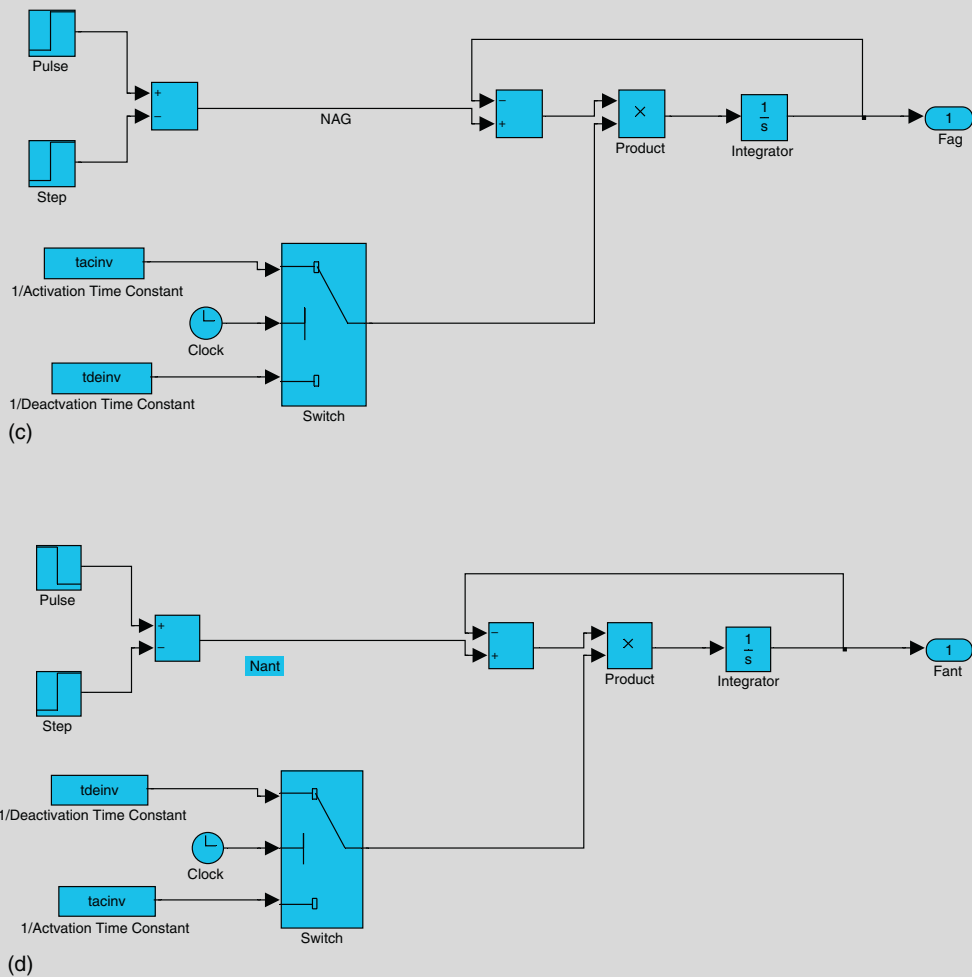


FIGURE 13.36, cont'd

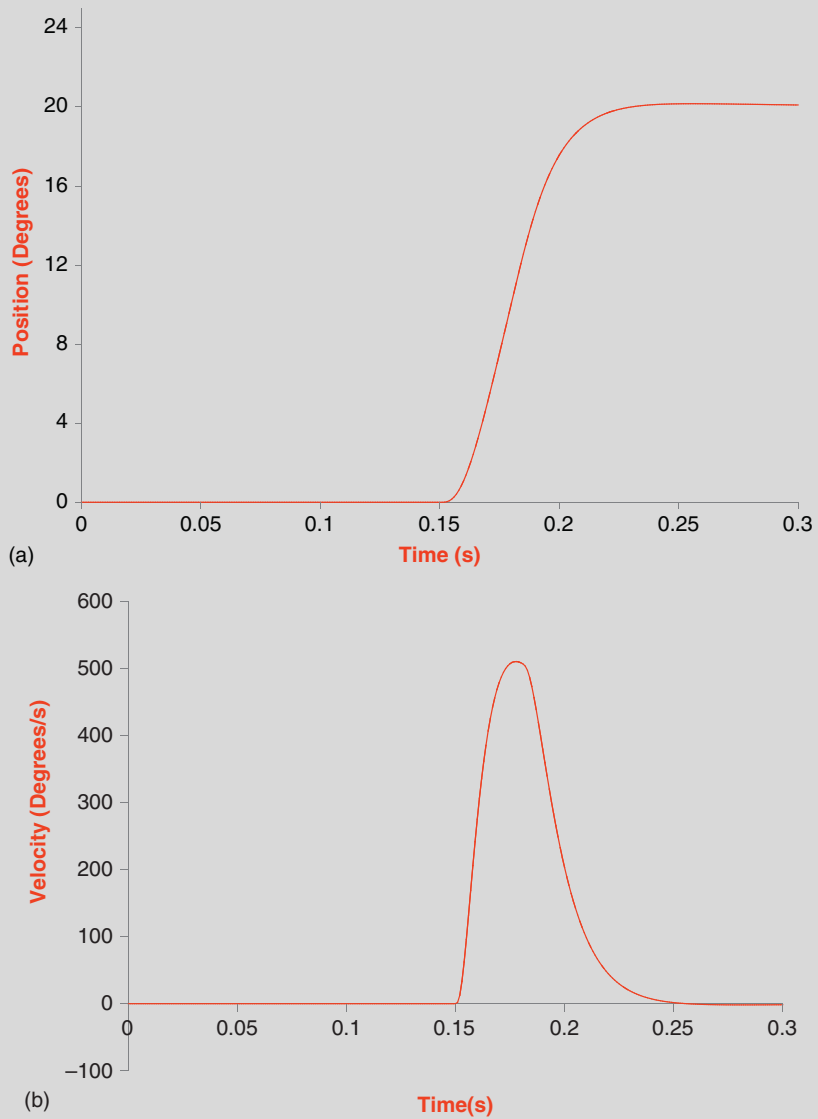


FIGURE 13.37 Plots of position, velocity, acceleration, agonist neural input (dotted line) and active-state tension (solid line), and antagonist neural input and active-state tension for Example Problem 13.6.

*Continued*

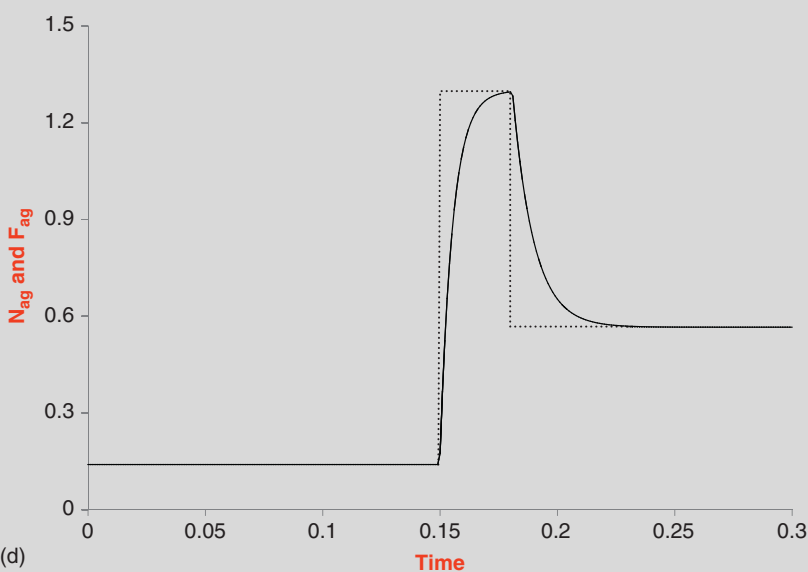
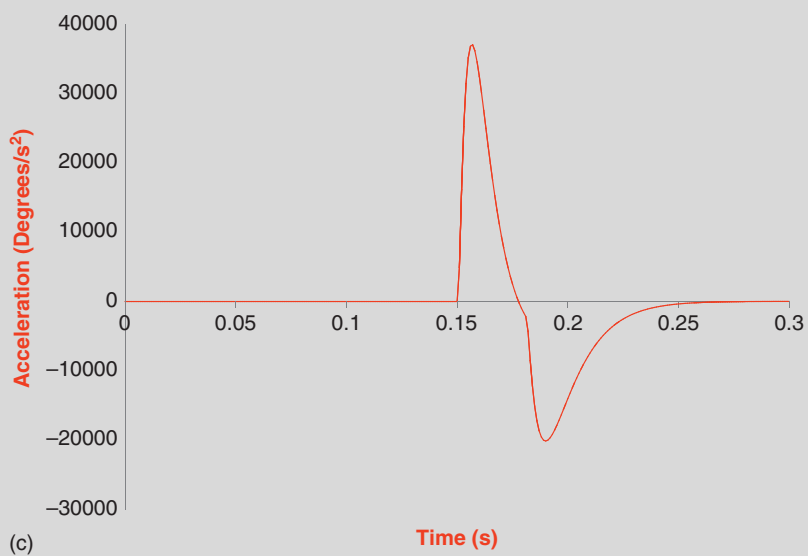


FIGURE 13.37, cont'd

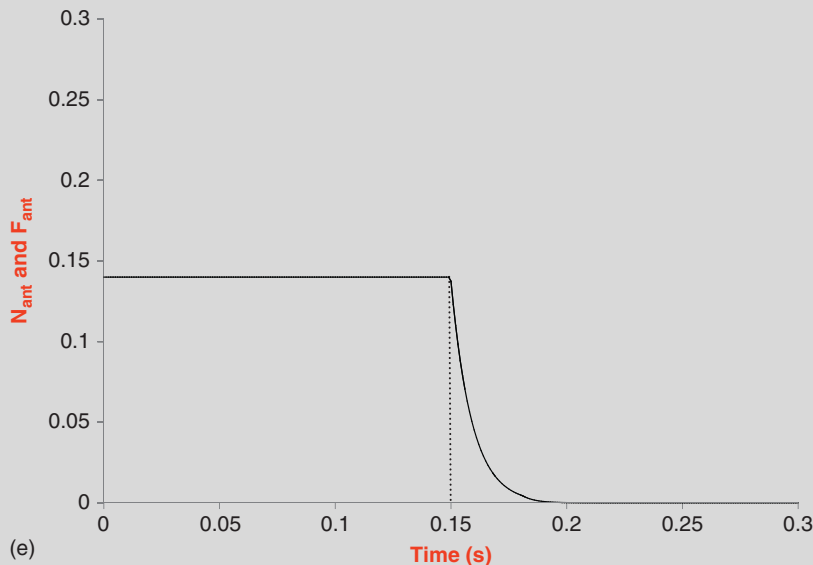


FIGURE 13.37, cont'd

### 13.7 THE 1995 LINEAR HOMEOMORPHIC SACCADIC EYE MOVEMENT MODEL

In the previous section, we presented a linear model of the oculomotor plant developed by linearizing the force-velocity curve. We then derived a linear differential equation to describe the system. Here we reexamine the static and dynamic properties of muscle in the development of a new linear model of oculomotor muscle. With the updated linear model of oculomotor muscle, the model of the oculomotor system will also be updated.

#### 13.7.1 The Linear Muscle Model

The updated linear model for oculomotor muscle is shown in Figure 13.38. Each of the elements in the model is linear and supported with physiological evidence. The muscle is modeled as a parallel combination of viscosity  $B_2$  and series elasticity  $K_{se}$ , connected to the parallel combination of active-state tension generator  $F$ , viscosity element  $B_1$ , and length tension elastic element  $K_{lt}$ . Variables  $x_1$  and  $x_2$  describe the displacement from the equilibrium for the stiffness elements in the muscle model. The only structural difference between this model and the previous oculomotor muscle model is the addition of viscous element  $B_2$  and the removal of passive elasticity  $K_{pe}$ . As will be described, the viscous element  $B_2$  is vitally important to describe the nonlinear force-velocity characteristics of the muscle, and the elastic element  $K_{pe}$  is unnecessary.

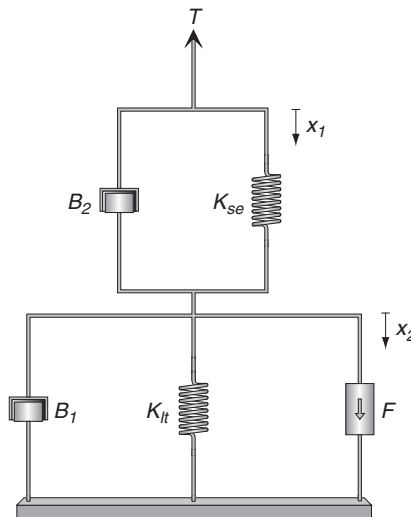


**FIGURE 13.38** An updated linear muscle model consisting of an active-state tension generator  $F$  in parallel with a length-tension elastic element  $K_{lt}$  and viscous element  $B_1$ , connected to a series elastic element  $K_{se}$  in parallel with a viscous element  $B_2$ . Upon stimulation of the active-state tension generator  $F$ , a tension  $T$  is exerted by the muscle.

The need for two elastic elements in the linear oculomotor muscle model is supported through physiological evidence. As described previously, the use and value of the series elasticity  $K_{se}$  were determined from the isotonic-isometric quick release experiment by Collins. Length-tension elasticity  $K_{lt}$  was estimated in a slightly different fashion than before from the slope of the length-tension curve. Support for the two linear viscous elements is based on the isotonic experiment and estimated from simulation results presented in this chapter.

### 13.7.2 The Length-Tension Curve

The basis for assuming nonlinear elasticity is the nonlinear length-tension relation for excited and unexcited muscle for tensions below 10 g, as shown in Figure 13.14. Using a miniature "C" gauge force transducer, Collins in 1975 measured muscle tension in vivo at the muscle tendon during unrestrained human eye movements. Data shown in Figure 13.14 were recorded from the rectus muscle of the left eye by measuring the isometric tensions at different muscle lengths, ranging from eye positions of  $-45^\circ$  to  $45^\circ$ , and different levels of innervation, established by directing the subject to look at the corresponding targets with the unhampered right eye from  $-45^\circ$  temporal (T) to  $45^\circ$  nasal (N). The change in eye position during this experiment corresponds to a change in muscle length of approximately 18 mm. Collins described the length-tension curves as "straight, parallel lines above about 10 g. Below the 10 g level, the oculorotary muscles begin to go slack." He also reported that the normal range of tensions for the rectus muscle during all eye movements never falls below 10 g into the slack region when the in vivo force transducer is used.

In developing a muscle model for use in the oculomotor system, it is imperative that the model accurately exhibits the static characteristics of rectus eye muscle within the normal range of operation. Thus, any oculomotor muscle model must have length-tension characteristics consisting of straight, parallel lines above 10 g tension. Since oculomotor muscles do not operate below 10 g, it is not unimportant that the linear behavior of the model does not match this nonlinear portion in the length-tension curves observed in the data as was done in the development of the muscle model earlier. As demonstrated in this section, by concentrating on the operational region of the oculomotor muscles, accurate length-tension curves are obtained from the muscle model using just series elastic and length tension elastic elements, even when active-state tension is zero. Thus, there is no need to include a passive elastic element in the muscle model as previously required.

Since the rectus eye muscle is not in equilibrium at primary position (looking straight ahead, 0°) within the oculomotor system, it is necessary to define and account for the equilibrium position of the muscle. Equilibrium denotes the unstretched length of the muscle when the tension is zero, with zero input. It is assumed that the active-state tension is zero on the 45° T length-tension curve. Typically, the equilibrium position for rectus eye muscle is found from within the slack region, where the 45° T length-tension curve intersects the horizontal axis. Note that this intersection point was not shown in the data collected by Collins (see [Figure 13.14](#)) but is reported to be approximately 15° (3 mm short of primary position), a value that is typical of those reported in the literature.

Since the muscle does not operate in the slack region during normal eye movements, using an equilibrium point calculated from the operational region of the muscle provides a much more realistic estimate for the muscle. Here, the equilibrium point is defined according to the straight-line approximation to the 45° T length-tension curve above the slack region. The value at the intersection of the straight-line approximation with the horizontal axis gives an equilibrium point of -19.3°. By use of the equilibrium point at -19.3°, there is no need to include an additional elastic element  $K_{pe}$  to account for the passive elasticity associated with unstimulated muscle as others have done.

The tension exerted by the linear muscle model shown in [Figure 13.38](#) is given by

$$T = \frac{K_{se}}{K_{se} + K_{lt}} F - \frac{K_{se} K_{lt}}{K_{se} + K_{lt}} x_1 \quad (13.38)$$

With the slope of the length-tension curve equal to  $0.8 \text{ g/}^\circ = 40.86 \text{ N/m}$  in the operating region of the muscle (nonslack region),  $K_{se} = 2.5 \text{ g/}^\circ = 125 \text{ N/m}$ , and [Eq. \(13.38\)](#) has a slope of

$$\frac{K_{se} K_{lt}}{K_{se} + K_{lt}} \quad (13.39)$$

$K_{lt}$  is evaluated as  $1.2 \text{ g/}^\circ = 60.7 \text{ N/m}$ .

To estimate the static active-state tension for fixation at the locations detailed in [Figure 1](#) of Collins [7], we use the techniques by Enderle and coworkers [19] by taking [Eq. \(13.38\)](#) to solve for steady-state active-state tensions for each innervation level straight-line approximation, yielding for  $\theta > 0^\circ$  (N direction)

$$F = 0.4 + 0.0175\theta N \quad \text{for } \theta > 0^\circ (\text{N direction}) \quad (13.40)$$

and

$$F = 0.4 + 0.012\theta N \quad \text{for } \theta \leq 0^\circ (\text{T direction}) \quad (13.41)$$

where  $\theta$  is the angle that the eyeball is deviated from the primary position measured in degrees, and  $\theta = 5208.7 \times (x_1 - 3.705)$ . Note that  $5208.7 = \frac{180}{\pi r}$ , where  $r$  equals the radius of the eyeball with a value of 11 mm.

Figure 13.39 displays a family of static length-tension curves obtained using Eqs. (13.38)–(13.41), which depicts the length-tension experiment. No attempt is made to describe the activity within the slack region, since the rectus eye muscle does not normally operate in that region. The length-tension relationship shown in Figure 13.39 is in excellent agreement with the data shown in Figure 13.14 within the operating region of the muscle.

### 13.7.3 The Force-Velocity Relationship

The original basis for assuming nonlinear muscle viscosity is that the expected linear relation between external load and maximum velocity was not observed in early experiments by Fenn and Marsh [22]. As they reported, “If the muscle is represented accurately

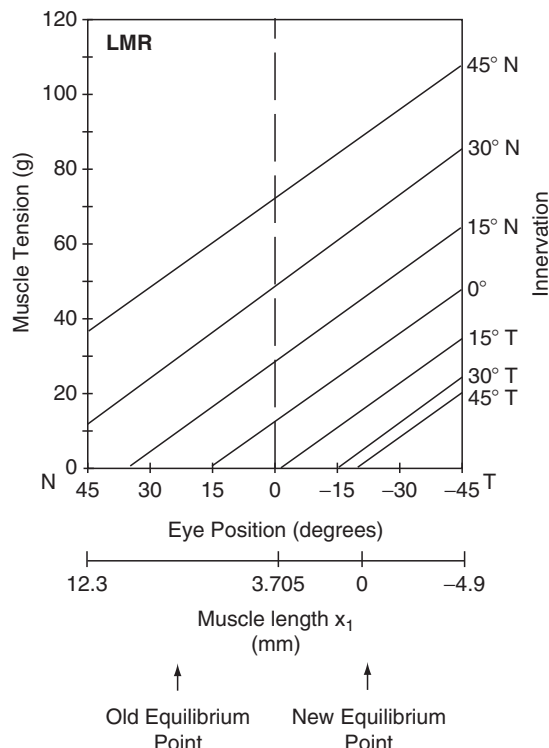


**FIGURE 13.39** Length-tension relationship generated using Equations (13.38)–(13.41) derived from the linear muscle model and inputs:  $F = 130$  g for  $45^\circ$  N,  $F = 94.3$  g for  $30^\circ$  N,  $F = 64.9$  g for  $15^\circ$  N,  $F = 40.8$  g for  $0^\circ$ ,  $F = 21.7$  g for  $15^\circ$  T,  $F = 5.1$  g for  $30^\circ$  T, and  $F = 0$  g for  $45^\circ$  T. These lines were parameterized to match Figure 13.14.

by a viscous elastic system, this force-velocity curve should have been linear, the loss of force being always proportional to the velocity. The slope of the curve would then represent the coefficient of viscosity." Essentially the same experiment was repeated for rectus eye muscle by Close and Luff in 1974 with similar results.

The classic force-velocity experiment was performed to test the viscoelastic model for muscle as described previously in [Section 13.5.4](#). Under these conditions, it was first assumed that the inertial force exerted by the load during isotonic shortening could be ignored. The second assumption was that if mass was not reduced enough by the lever ratio (enough to be ignored), then taking measurements at maximum velocity provided a measurement at a time when acceleration is zero, and, therefore, inertial force equals zero. If these two assumptions are valid, then the experiment would provide data free of the effect of inertial force as the gravity force is varied. Both assumptions are incorrect. The first assumption is wrong, since the inertial force is never minimal (minimal would be zero) and therefore has to be taken into account. The second assumption is wrong, since, given an inertial mass not equal to zero, the maximum velocity depends on the forces that act prior to the time of maximum velocity. The force-velocity relationship is carefully reexamined with the inertial force included in the analysis in this section.

The dynamic characteristics for the linear muscle model are described with a force-velocity curve calculated via the lever system presented in [Figure 13.20](#) and according to the isotonic experiment. For the rigid lever, the displacements  $x_1$  and  $x_3$  are directly proportional to the angle  $\theta_1$  and to each other, such that

$$\theta_1 = \frac{x_1}{d_1} = \frac{x_3}{d_3} \quad (13.42)$$

The equation describing the torques acting on the lever is given by

$$Mgd_3 + Md_3^2\ddot{\theta}_1 = d_1K_{se}(x_2 - x_1) + d_1B_2(\dot{x}_2 - \dot{x}_1) \quad (13.43)$$

The equation describing the forces at node 2, inside the muscle, is given by

$$F = K_{lt}x_2 + B_1\dot{x}_2 + B_2(\dot{x}_2 - \dot{x}_1) + K_{se}(x_2 - x_1) \quad (13.44)$$

[Equation \(13.43\)](#) is rewritten by removing  $\theta_1$  using [Eq. \(13.42\)](#), hence

$$Mg\frac{d_3}{d_1} + M\left(\frac{d_3}{d_1}\right)^2\ddot{x}_1 = K_{se}(x_2 - x_1) + B_2(\dot{x}_2 - \dot{x}_1) \quad (13.45)$$

Ideally, to calculate the force-velocity curve for the lever system,  $x_1(t)$  is found first. Then  $\dot{x}_1(t)$  and  $\ddot{x}_1(t)$  are found from  $x_1(t)$ . Finally, the velocity is found from  $V_{\max} = \dot{x}_1(T)$ , where time  $T$  is the time it takes for the muscle to shorten to the stop, according to the experimental conditions of Close and Luff. While this velocity may not be maximum velocity for all data points, the symbol  $V_{\max}$  is used to denote the velocities in the force-velocity curve for ease in presentation. Note that this definition of velocity differs from the Fenn and Marsh definition of velocity. Fenn and Marsh denoted maximum velocity as  $V_{\max} = \dot{x}_1(T)$ , where time  $T$  is found when  $\ddot{x}_1(T) = 0$ .

It should be noted that this is a third-order system and the solution for  $x_1(t)$  is not trivial and involves an exponential approximation (for an example of an exponential

approximation solution for  $V_{\max}$  from a fourth-order model, see the paper by [17], or [14]. It is more expedient, however, to simply simulate a solution for  $x_1(t)$  and then find  $V_{\max}$  as a function of load.

Using a simulation to reproduce the isotonic experiment, elasticities estimated from the length-tension curves as previously described, and data from rectus eye muscle, parameter values for the viscous elements in the muscle model are found as  $B_1 = 2 \text{ Nsm}^{-1}$  and  $B_2 = 0.5 \text{ Nsm}^{-1}$  as demonstrated by Enderle and coworkers in 1991. The viscous element  $B_1$  is estimated from the time constant from the isotonic time course. The viscous element  $B_2$  is calculated by trial and error so the simulated force-velocity curve matches the experimental force-velocity curve.

Figure 13.40 shows the force-velocity curves using the model described in Eq. (13.45) (with triangles), plotted along with an empirical fit to the data (solid line). It is clear that the force-velocity curve for the linear muscle model is hardly a straight line and that this curve fits the data well.

The muscle lever model described by Eqs. (13.43) and (13.44) is a third-order linear system and is characterized by three poles. Dependent on the values of the parameters, the eigenvalues (or poles) consist of all real poles or a real and a pair of complex conjugate poles. A real pole is the dominant eigenvalue of the system. Through a sensitivity analysis, viscous element  $B_1$  is the parameter that has the greatest effect on the dominant eigenvalue for this system, while viscous element  $B_2$  has very little effect on the dominant eigenvalue. Thus, viscous element  $B_1$  is estimated so the dominant time constant of the lever system model (approximately  $\frac{B_1}{K_{lt}}$  when  $B_1 > B_2$ ) matches the time constant from the isotonic experimental data. For rectus eye muscle data, the duration of the isotonic experiment is

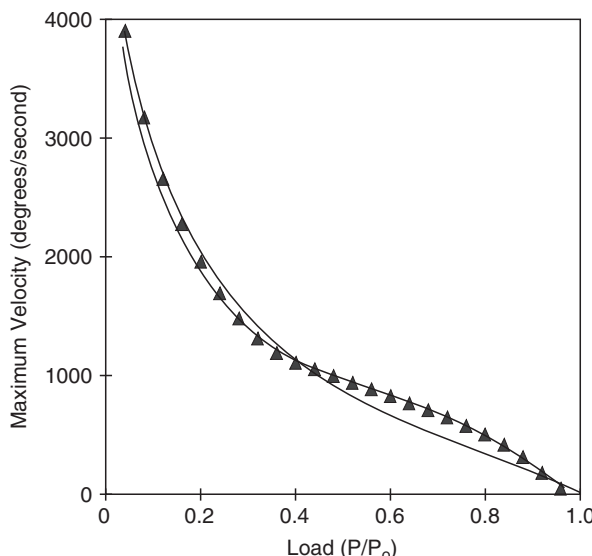


FIGURE 13.40 Force-velocity curve derived from simulation studies with the linear muscle model with an end stop. Shown with triangles indicating simulation calculation points and an empirical fit to the force-velocity data (solid line), as described by Close and Luff [6]. Adapted from Enderle et al. [19].

approximately 100 ms. A value for  $B_1 = 2 \text{ Nsm}^{-1}$  yields a simulated isotonic response with approximately the same duration. For skeletal muscle data, the duration of the isotonic experiment is approximately 400 ms, and a value for  $B_1 = 600 \text{ Nsm}^{-1}$  yields a simulated isotonic response with approximately the same duration. It is known that fast and slow muscle have differently shaped force velocity curves and that the fast muscle force-velocity curve data has less curvature. Interestingly, the changes in the parameter values for  $B_1$  as suggested here give differently shaped force velocity curves consistent with fast (rectus eye) and slow (skeletal) muscle.

The parameter value for viscous element  $B_2$  is selected by trial and error so the shape of the simulation force-velocity curve matches the data. As the value for  $B_2$  is decreased from  $0.5 \text{ Nsm}^{-1}$ , the shape of the force velocity curves changes to a more linear shaped function. Moreover, if the value of  $B_2$  falls below approximately  $0.3 \text{ Nsm}^{-1}$ , strong oscillations appear in the simulations of the isotonic experiment, which are not present in the data. Thus, the viscous element  $B_2$  is an essential component in the muscle model. Without it, the shape of the force-velocity curve is linear and the time course of the isotonic experiment does not match the characteristics of the data.

Varying the parameter values of the lever muscle model changes the eigenvalues of the system. For instance, with  $M = 0.5 \text{ kg}$ , the system's nominal eigenvalues (as defined with the parameter values previously specified) are a real pole at  $-30.71$  and a pair of complex conjugate poles at  $-283.9 \pm j221.2$ . If the value of  $B_2$  is increased, three real eigenvalues describe the system. If the value of  $B_2$  is decreased, a real pole and a pair of complex conjugate poles continue to describe the system. Changing the value of  $B_1$  does not change the eigenvalue composition, but it does significantly change the value of the dominant eigenvalue from  $-292$  with  $B_1 = 0.1$  to  $-10$  with  $B_1 = 6$ .

### 13.7.4 The 1995 Linear Homeomorphic Saccadic Eye Movement Model

The linear model of the oculomotor plant presented in [Section 13.6](#) is based on a nonlinear oculomotor plant model by Hsu and coworkers [33] using a linearization of the force-velocity relationship and elasticity curves. Using the linear model of muscle described earlier in this section, it is possible to avoid the linearization and to derive a truer linear homeomorphic saccadic eye movement model.

The linear muscle model described in this section has the static and dynamic properties of rectus eye muscle, a model without any nonlinear elements. As presented, the model has a nonlinear force-velocity relationship that matches eye muscle data using linear viscous elements, and the length tension characteristics are also in good agreement with eye muscle data within the operating range of the muscle. Some additional advantages of the linear muscle model are that a passive elasticity is not necessary if the equilibrium point  $x_e = -19.3^\circ$ , rather than  $15^\circ$ , and muscle viscosity is a constant that does not depend on the innervation stimulus level.

[Figure 13.41](#) shows the mechanical components of the updated oculomotor plant for horizontal eye movements, the lateral and medial rectus muscle, and the eyeball. The agonist muscle is modeled as a parallel combination of viscosity  $B_2$  and series elasticity  $K_{se}$ , connected to the parallel combination of active-state tension generator  $F_{ag}$ , viscosity element  $B_1$ , and length tension elastic element  $K_{lt}$ . For simplicity, agonist viscosity is set

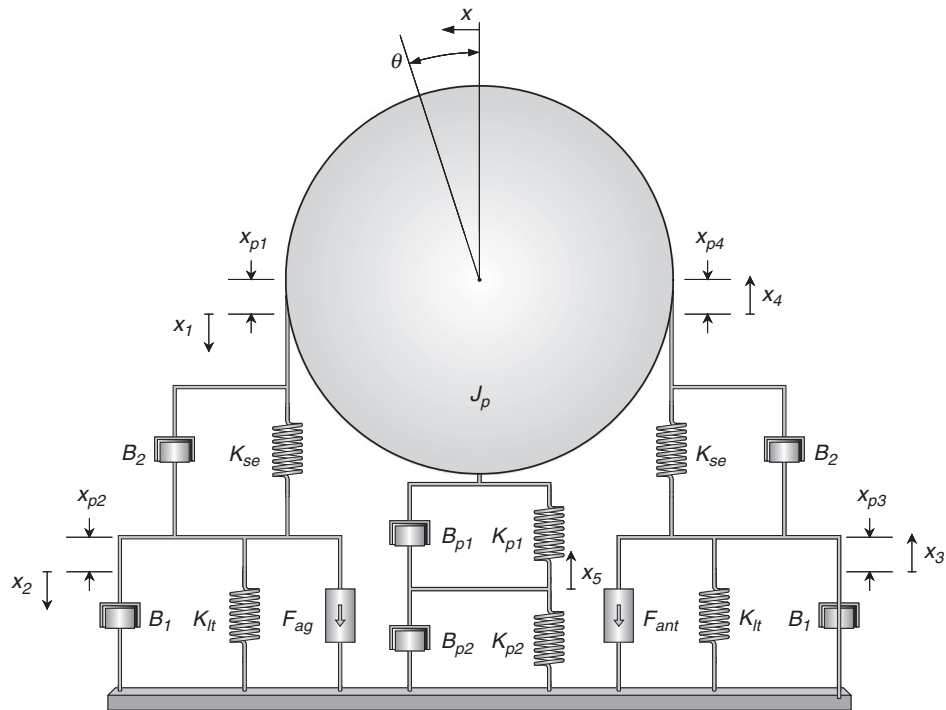


**FIGURE 13.41** The mechanical components of the updated oculomotor plant. The muscles are shown to be extended from equilibrium, a position of rest, at the primary position (looking straight ahead), consistent with physiological evidence. The average length of the rectus muscle at the primary position is approximately 40 mm and at the equilibrium position is approximately 37 mm.  $\theta$  is the angle the eyeball is deviated from the primary position, and variable  $x$  is the length of arc traversed. When the eye is at the primary position, both  $\theta$  and  $x$  are equal to zero. Variables  $x_1$  through  $x_4$  are the displacements from equilibrium for the stiffness elements in each muscle, and  $x_5$  is the rotational displacement for passive orbital tissues. Values  $x_{p1}$  through  $x_{p4}$  are the displacements from equilibrium for each of the variables  $x_1$  through  $x_4$  at the primary position. The total extension of the muscle from equilibrium at the primary position is  $x_{p1}$  plus  $x_{p2}$  or  $x_{p3}$  plus  $x_{p4}$ , which equals approximately 3 mm. It is assumed that the lateral and medial rectus muscles are identical, such that  $x_{p1}$  equals  $x_{p4}$  and  $x_{p3}$  equals  $x_{p2}$ . The radius of the eyeball is  $r$ .

equal to antagonist viscosity. The antagonist muscle is similarly modeled with a suitable change in active-state tension to  $F_{ant}$ . Each of the elements defined in the oculomotor plant is ideal and linear.

The eyeball is modeled as a sphere with moment of inertia  $J_p$ , connected to a pair of viscoelastic elements connected in series. The update of the eyeball model is based on observations by Robinson, presented in 1981, and the following discussion. In the model of the oculomotor plant described in Section 3.6, passive elasticity  $K_{pe}$  was combined with the passive elastic orbital tissues. In the new linear model muscle presented in this chapter, the elastic element  $K_{pe}$  is no longer included in the muscle model. Thus, the passive orbital tissue elasticity needs to be updated due to the elimination of  $K_{pe}$  and the observations by Robinson. As reported by Robinson in 1981, "When the human eye, with horizontal recti detached, is displaced and suddenly released, it returns rapidly about 61 percent of the

way with a time constant of about 0.02 sec, and then creeps the rest of the way with a time constant of about 1 sec." As suggested according to this observation, there are at least two viscoelastic elements. Here it is proposed that these two viscoelastic elements replace the single viscoelastic element of the previous oculomotor plant. Connected to the sphere, are  $B_{p1}||K_{p1}$  connected in series to  $B_{p2}||K_{p2}$ . As reported by Robinson, total orbital elasticity is equal to  $12.8 \times 10^{-7}$  g/ $^{\circ}$  (scaled for this model). Thus, with the time constants previously described, the orbital viscoelastic elements are evaluated as  $K_{p1} = 1.28 \times 10^{-6}$  g/ $^{\circ}$ ,  $K_{p2} = 1.98 \times 10^{-6}$  g/ $^{\circ}$ ,  $B_{p1} = 2.56 \times 10^{-8}$  gs/ $^{\circ}$ , and  $B_{p2} = 1.98 \times 10^{-6}$  gs/ $^{\circ}$ . For modeling purposes,  $\theta_5$  is the variable associated with the change from equilibrium for these two pairs of viscoelastic elements. Both  $\theta$  and  $\theta_5$  are removed from the analysis for simplicity using the substitution  $\theta = 57.296 \frac{x}{r}$  and  $\theta_5 = 57.296 \frac{x_5}{r}$ .

By summing the forces acting at junctions 2 and 3, and the torques acting on the eyeball and junction 5, a set of four equations is written to describe the oculomotor plant:

$$\begin{aligned} F_{ag} &= K_{lt}x_2 + B_1\dot{x}_2 + K_{se}(x_2 - x_1) + B_2(\dot{x}_2 - \dot{x}_1) \\ B_2(\dot{x}_4 - \dot{x}_3) + K_{se}(x_4 - x_3) &= F_{ant} + K_{lt}x_3 + B_1\dot{x}_3 \\ B_2(\dot{x}_2 + \dot{x}_3 - \dot{x}_1 - \dot{x}_4) + K_{se}(x_2 + x_3 - x_1 - x_4) &= J\ddot{x} + B_3(\dot{x} - \dot{x}_5) + K_1(x - x_5) \\ K_1(x - x_5) + B_3(\dot{x} - \dot{x}_5) &= B_4\dot{x}_5 + K_2x_5 \end{aligned} \quad (13.46)$$

where

$$J = \frac{57.296}{r^2}J_p, \quad B_3 = \frac{57.296}{r^2}B_{p1}, \quad B_4 = \frac{57.296}{r^2}B_{p2}, \quad K_1 = \frac{57.296}{r^2}K_{p1}, \quad K_2 = \frac{57.296}{r^2}K_{p2}$$

Using Laplace variable analysis about an operating point yields

$$\begin{aligned} K_{se}K_{12}(F_{ag} - F_{ant}) + (K_{se}B_{34} + B_2K_{12})(\dot{F}_{ag} - \dot{F}_{ant}) + B_2B_{34}\left(\ddot{F}_{ag} - \ddot{F}_{ant}\right) \\ = C_4\ddot{x} + C_3\ddot{x} + C_2\ddot{x} + C_1\dot{x} + C_0x \end{aligned} \quad (13.47)$$

where

$$\begin{aligned} B_{12} &= B_1 + B_2, \quad B_{34} = B_3 + B_4, \quad K_{12} = K_1 + K_2, \quad K_{st} = K_{se} + K_{lt} \\ C_4 &= JB_{12}B_{34} \\ C_3 &= B_3B_4B_{12} + 2B_1B_2B_{34} + JB_{34}K_{st} + JB_{12}K_{12} \\ C_2 &= 2B_1B_{34}K_{se} + JK_{st}K_{12} + B_3B_{34}K_{st} + B_3B_{12}K_{12} + K_1B_{12}B_{34} - B_3^2K_{st} - 2K_1B_3B_{12} \\ &\quad + 2B_2K_{lt}B_{34} + 2B_1K_{12}B_2 \\ C_1 &= 2K_{lt}B_{34}K_{se} + 2B_1K_{12}K_{se} + B_3K_{st}K_2 + K_1B_{34}K_{st} + K_1B_{12}K_{12} - K_{st}K_1B_3 \\ &\quad - K_1^2B_{12} + 2B_2K_{lt}K_{12} \\ C_0 &= 2K_{lt}K_{se}K_{12} + K_1K_{st}K_2 \end{aligned}$$

Converting from  $x$  to  $\theta$  gives

$$\begin{aligned} \delta\left(K_{se}K_{12}(F_{ag} - F_{ant}) + (K_{se}B_{34} + B_2K_{12})(\dot{F}_{ag} - \dot{F}_{ant}) + B_2B_{34}\left(\ddot{F}_{ag} - \ddot{F}_{ant}\right)\right) \\ = \ddot{\theta} + P_3\ddot{\theta} + P_2\dot{\theta} + P_1\dot{\theta} + P_0\theta \end{aligned} \quad (13.48)$$

where

$$\delta = \frac{57.296}{rJB_{12}B_{34}}, P_3 = \frac{C_3}{C_4}, P_2 = \frac{C_2}{C_4}, P_1 = \frac{C_1}{C_4}, P_0 = \frac{C_0}{C_4}$$

Based on an analysis of experimental data, suitable parameter estimates for the oculomotor plant are as follows:

$$\begin{aligned} K_{SE} &= 125 \text{ Nm}^{-1} \\ K_{LT} &= 60.7 \text{ Nm}^{-1} \\ B_1 &= 2.0 \text{ Nsm}^{-1} \\ B_2 &= 0.5 \text{ Nsm}^{-1} \\ J &= 2.2 \times 10^{-3} \text{ Ns}^2\text{m}^{-1} \\ B_3 &= 0.538 \text{ Nsm}^{-1} \\ B_4 &= 41.54 \text{ Nsm}^{-1} \\ K_1 &= 26.9 \text{ Nm}^{-1} \\ K_2 &= 41.54 \text{ Nm}^{-1} \end{aligned}$$

Based on the updated model of muscle and length tension data presented in the previous section, steady-state active-state tensions are determined as

$$F = \begin{cases} 0.4 + 0.0175\theta & \text{N for } \theta \geq 0^\circ \\ 0.4 + 0.0125\theta & \text{N for } \theta < 0^\circ \end{cases} \quad (13.49)$$

The agonist and antagonist active-state tensions follow from [Figure 13.11](#), which assume no latent period, and are given by the following low-pass filtered waveforms:

$$\dot{F}_{ag} = \frac{N_{ag} - F_{ag}}{\tau_{ag}} \quad \text{and} \quad \dot{F}_{ant} = \frac{N_{ant} - F_{ant}}{\tau_{ant}} \quad (13.50)$$

where  $N_{ag}$  and  $N_{ant}$  are the neural control inputs (pulse-step waveforms), and

$$\tau_{ag} = \tau_{ac}(u(t) - u(t - t_1)) + \tau_{de}u(t - t_1)$$

$$\tau_{ant} = \tau_{de}(u(t) - u(t - t_1)) + \tau_{ac}u(t - t_1)$$

are the time-varying time constants.

Saccadic eye movements simulated with this model have characteristics that are in good agreement with the data, including position, velocity and acceleration, and the main sequence diagrams. As before, the relationship between agonist pulse magnitude and pulse duration is tightly coupled.

### EXAMPLE PROBLEM 13.7

Using the oculomotor plant model described with [Eq. \(13.48\)](#), parameters given in this section, and the steady-state input from [Eq. \(13.49\)](#), simulate a  $10^\circ$  saccade. Plot agonist and antagonist active-state tension, position, velocity, and acceleration versus time. Compare the simulation with the main sequence diagram in [Figure 13.6](#).

*Continued*

### Solution

The solution to this example involves selecting a set of parameters ( $F_p$ ,  $t_1$ ,  $\tau_{ac}$ , and  $\tau_{de}$ ) that match the characteristics observed in the main sequence diagram shown in Figure 13.6. There is a great deal of flexibility in simulating a 10° saccade. The only constraints for the 10° saccade simulation results are that the duration is approximately 40 to 50 ms and peak velocity is in the 500 to 600°s<sup>-1</sup> range. For realism, a latent period of 150 ms has been added to the simulation results. A SIMULINK block diagram of Eq. (13.48) is shown in Figure 13.42.

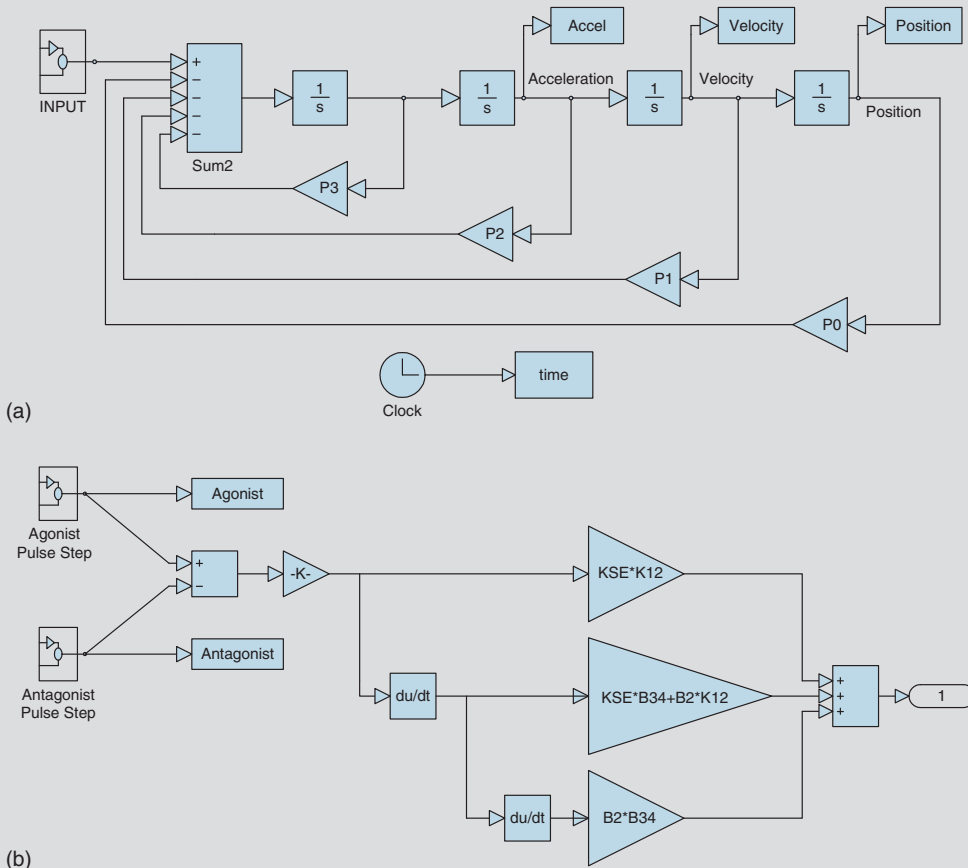


**FIGURE 13.42** SIMULINK block diagrams for Example Problem 13.7. (a) Model defined by Eq. (13.49). (b) The input.

*Continued*

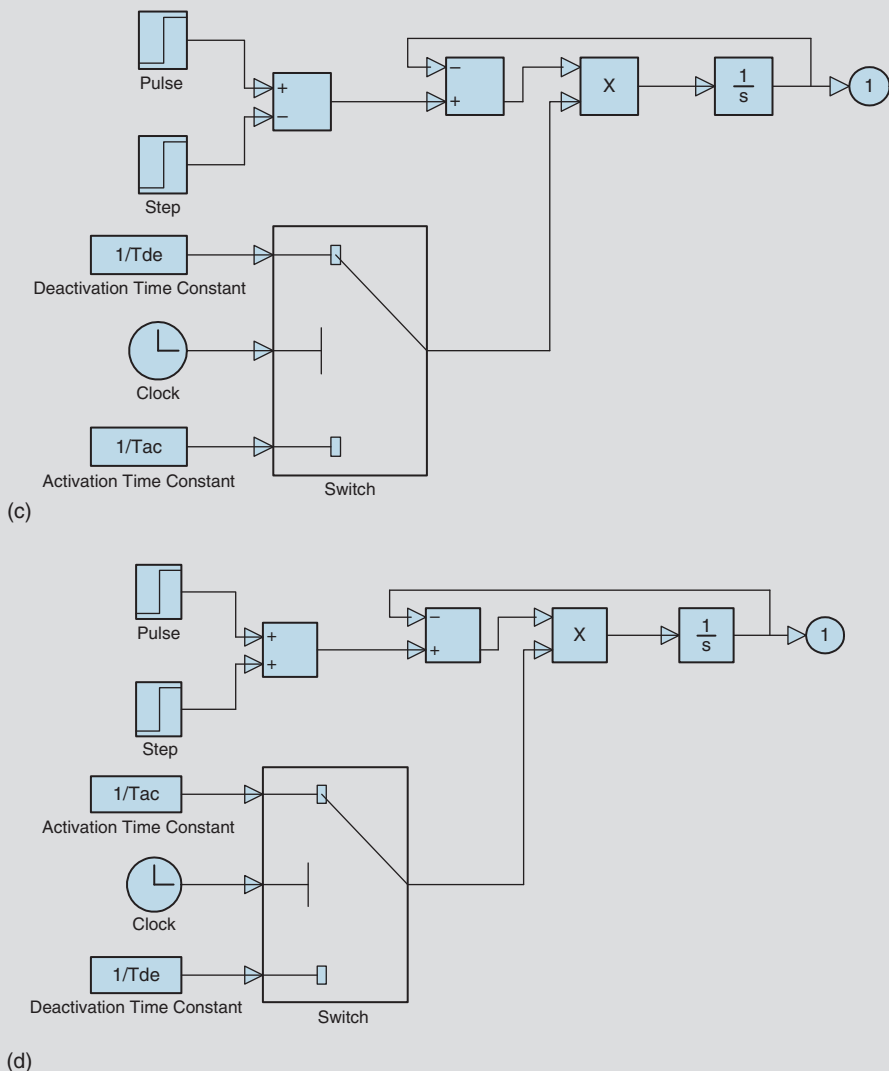
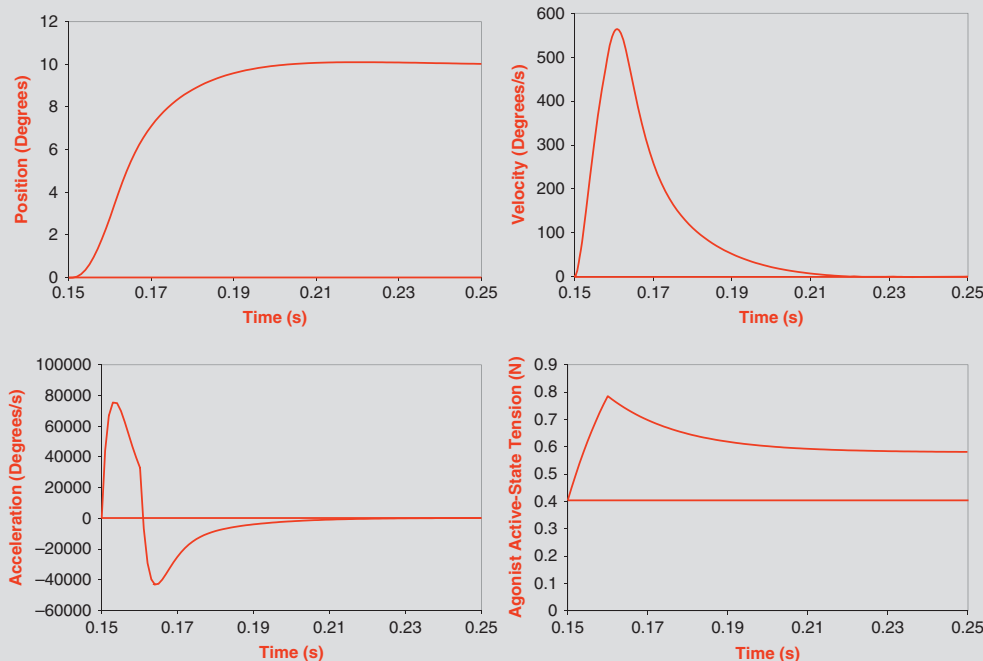


FIGURE 13.42, cont'd (c) Agonist pulse-step. (d) Antagonist pulse-step.

The response of the system is shown in Figure 13.43, with  $F_p = 1.3 \text{ N}$ ,  $t_1 = 0.01 \text{ s}$ ,  $\tau_{ac} = 0.018 \text{ s}$ , and  $\tau_{de} = 0.018 \text{ s}$ . These  $10^\circ$  simulation results have the main sequence characteristics with a peak velocity of  $568^\circ\text{s}^{-1}$  and a duration of 45 ms.

*Continued*



**FIGURE 13.43** Simulation for Example Problem 13.7, with  $F_p = 1.3 \text{ N}$ ,  $t_1 = 0.10 \text{ s}$ ,  $\tau_{ac} = 0.018 \text{ s}$ , and  $\tau_{de} = 0.018 \text{ s}$ .

Many other parameter sets can also simulate a 10° saccade. For instance, consider reducing  $\tau_{de}$  to .009 s. Because the antagonist active-state tension activity goes toward zero more quickly than in the last case, a greater total active-state tension ( $F_{ag} - F_{ant}$ ) results. Therefore, to arrive at 10° with the appropriate main sequence characteristics,  $F_p$  needs to be reduced to 1.0 N if  $\tau_{ac}$  remains at 0.018 s and  $t_1$  equals 0.0115 s. This 10° simulation is shown in Figure 13.44.

To simulate larger saccades with main sequence characteristics, the time constants for the agonist and antagonist active-state tensions can be kept at the same values as the 10° saccades or made functions of saccade amplitude (see [1] for several examples of amplitude-dependent time constants). Main sequence simulations for 15° and 20° saccades are obtained with  $F_p = 1.3 \text{ N}$  and the time constants are both fixed at 0.018 s (the first case) by changing  $t_1$  to 0.0155 and 0.0223 s, respectively. For example, the 20° simulation results are shown in Figure 13.45, with a peak velocity of  $682^{\circ}\text{s}^{-1}$  and a duration of 60 ms.

In general, as  $F_p$  increases,  $t_1$  decreases to maintain the same saccade amplitude. Additionally, peak velocity increases as  $F_p$  increases. For the saccade amplitude to remain a constant as either or both of the time constants increase,  $F_p$  should also increase.

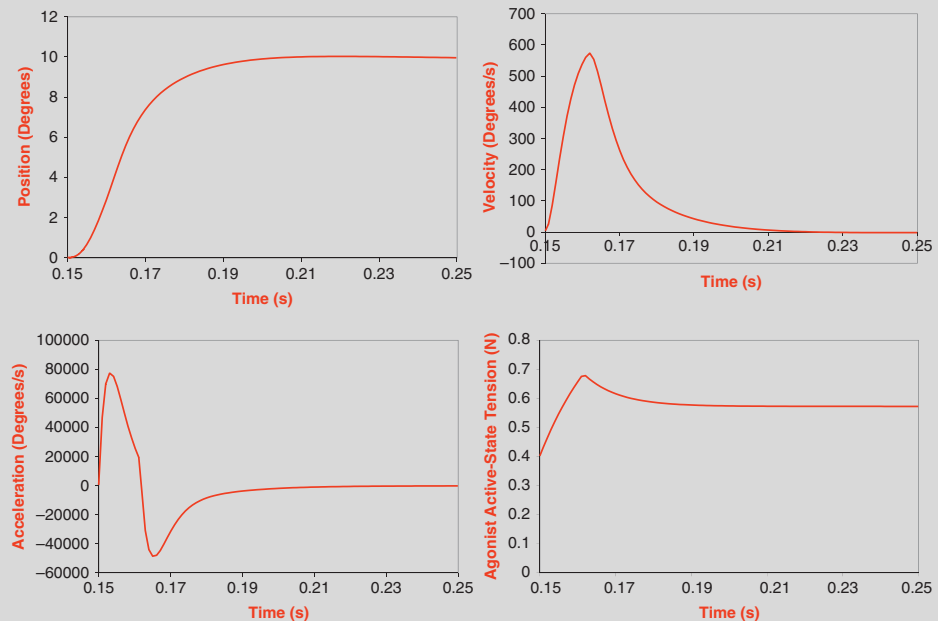


FIGURE 13.44 Simulation for Example Problem 13.7, with  $F_p = 1.0 \text{ N}$ ,  $t_I = 0.010 \text{ s}$ ,  $\tau_{ac} = 0.018 \text{ s}$ , and  $\tau_{de} = 0.009 \text{ s}$ .

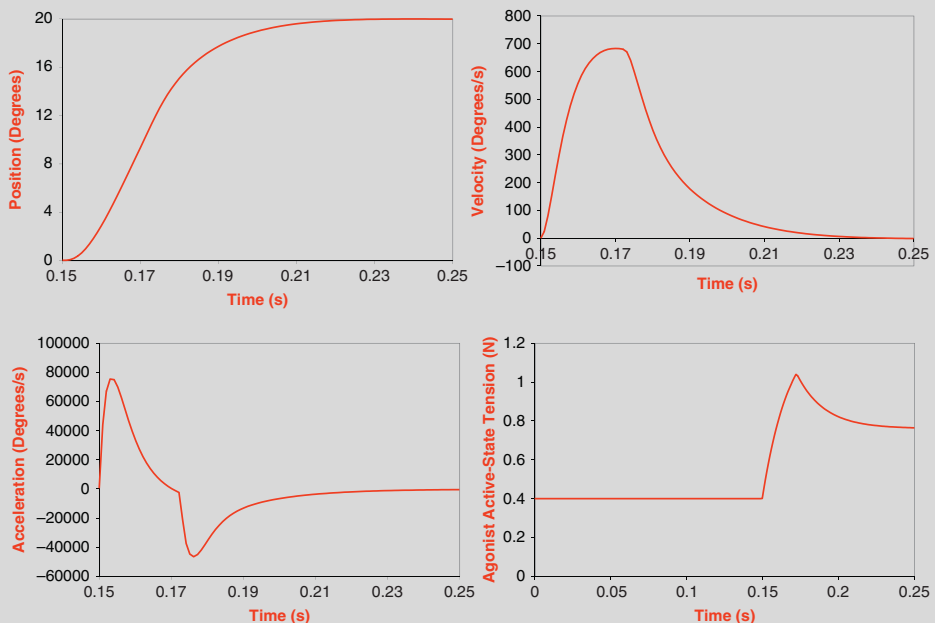


FIGURE 13.45 Simulation for Example Problem 13.7, with  $F_p = 1.3 \text{ N}$ ,  $t_I = 0.0223 \text{ s}$ ,  $\tau_{ac} = 0.018 \text{ s}$ , and  $\tau_{de} = 0.018 \text{ s}$ .

### 13.8 THE 2009 LINEAR HOMEOMORPHIC SACCADIC EYE MOVEMENT MODEL

In this section, we further explore the fast eye movement system that has postsaccade behavior, including normal saccades and those with a dynamic or a glissadic overshoot based on a model by Zhou, Chen, and Enderle [50] and Enderle and Zhou [18]. Postsaccade phenomena, such as a dynamic or a glissadic overshoot, are usually observed during human saccades [47]. In dynamic overshoot, the eyes move beyond the target, and then, with a quick saccade-like return with no time delay, the eyes move back to the target. Glissadic overshoot is similar to dynamic overshoot but with a return that is slower. To analyze postsaccade behavior, the neural input to the muscles is now described by a pulse-slide-step of neural activity, supported by physiological evidence [26]. The slide is a slow exponential transition from the pulse to the step.

The oculomotor plant is shown in Figure 13.46. It should be noted that the passive elasticity of the eyeball in Figure 13.46 is changed from the model in Figure 13.41 that included two Voigt passive elements connected in series to a single Voigt element. The Voigt element with time constant 0.02 s is used in the model presented here. The other Voigt element, with a time constant of 1 s, is neglected, since it has an insignificant effect on the accuracy because we are modeling a single saccade and not a series of saccades. Further, eliminating

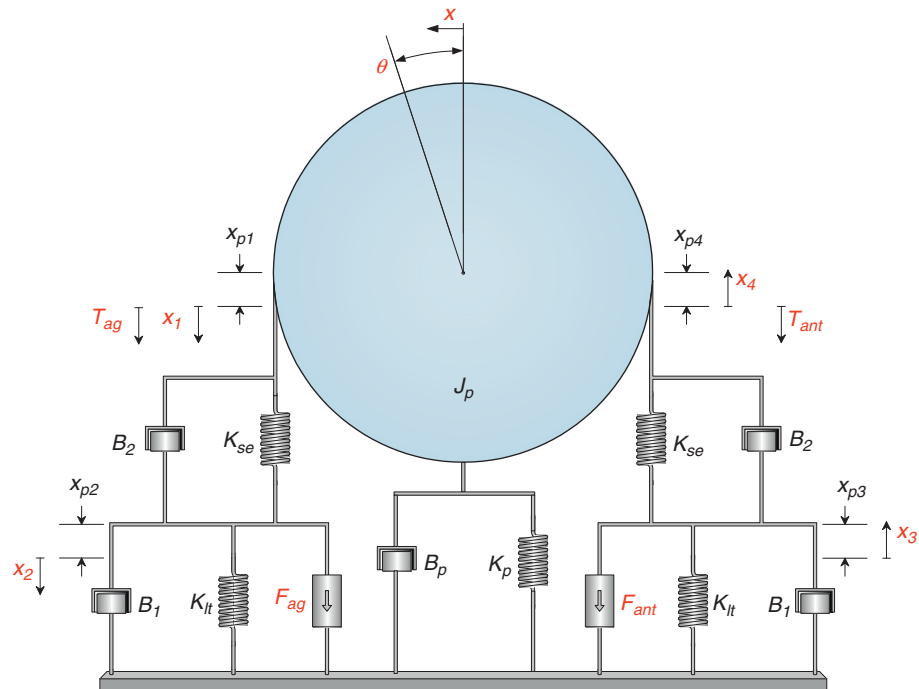


FIGURE 13.46 Oculomotor plant used for analyzing saccades with postsaccade behavior.

this Voigt element reduces the order of the model from fourth to third order and simplifies the system identification. The net torque generated by the muscles during a saccade rotates the eyeball to a new orientation and, after the saccade is completed, compensates the passive restraining torques generated by orbital tissues.

By summing the forces at junctions 2 and 3 (the equilibrium positions for  $x_2$  and  $x_3$ ) and the torques acting on the eyeball, using Laplace variable analysis about the operating point, the linear homeomorphic model, as shown in Figure 13.46, is derived as

$$\delta(B_2(\dot{F}_{ag} - \dot{F}_{ant}) + K_{se}(F_{ag} - F_{ant})) = \ddot{\theta} + P_2\ddot{\theta} + P_1\dot{\theta} + P_0\theta \quad (13.51)$$

where

$$\delta = \frac{5208.7}{JB_{12}}$$

$$P_2 = \frac{JK_{st} + B_{12}B + 2B_1B_2}{JB_{12}}$$

$$P_1 = \frac{2B_1K_{se} + 2B_2K_{lt} + B_{12}K + K_{st}B}{JB_{12}}$$

$$P_0 = \frac{K_{st}K + 2K_{lt}K_{se}}{JB_{12}}$$

Full details of the derivation are provided in Enderle and Zhou [18].

### 13.8.1 Neural Input

Previously, we modeled the neural input to the saccade system as a pulse-step waveform. This input has been used in many studies because of its simplicity and ease of use [4, 17, 20]. To create a more realistic input based on physiological evidence, a pulse-slide-step input is used as shown in Figure 13.47 (based on [26]). The slide is an exponential transition from the pulse to the step. This model is consistent with the data published in the literature (for example, see Figure 4 in [42], and Figure 2 in [46]). The diagram in Figure 13.47 (top) closely approximates the data shown in Figure 13.47 (bottom) for the agonist input.

At steady state, the eye is held steady by the agonist and antagonist inputs  $F_{g0}$  and  $F_{t0}$ . We typically define the time when the target moves as  $t = 0$ . This is a common assumption, since many simulation studies ignore the latent period and focus on the actual movement.

The overall agonist pulse occurs in the interval  $0 - T_2$ , with a more complex behavior than the pulse described earlier. We view the overall pulse process as the intention of the system, which is limited by its physical capabilities. The start of the pulse occurs with an exponential rise from the initial firing rate,  $F_{g0}$ , to peak magnitude,  $F_{p1}$ , with a time constant  $\tau_{gn1}$ . At  $T_1$ , the input decays to  $F_{p2}$ , with a time constant  $\tau_{gn2}$ . The slide occurs at  $T_2$ , with a time constant  $\tau_{gn3}$ , to  $F_{gs}$ , the force necessary to hold the eye at its destination. The input  $F_{gs}$  is applied during the step portion of the input.

At  $t = 0$ , the antagonist neural input is completely inhibited and exponentially decays to zero from  $F_{t0}$  with time constant  $\tau_{tn1}$ . At time  $T_3$ , the antagonist input exponentially increases with time constant  $\tau_{tn2}$ . The antagonist neural input shown in Figure 13.47 (middle)

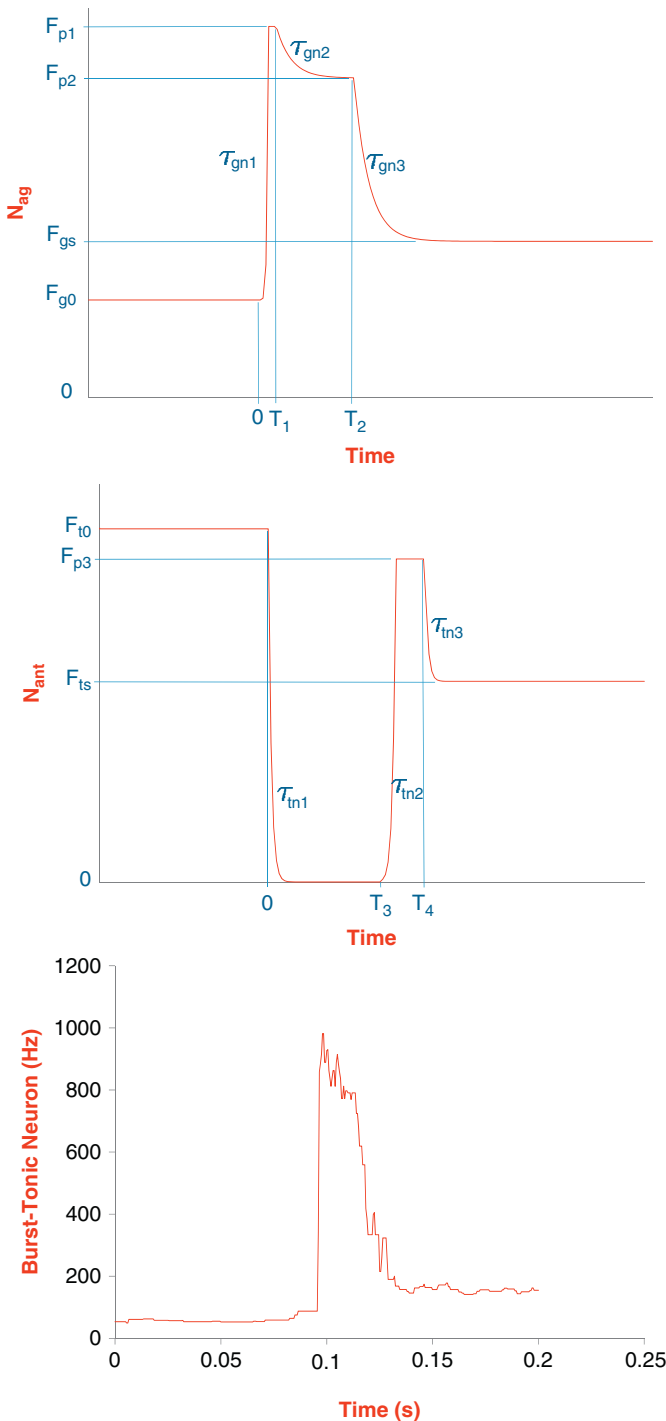


**FIGURE 13.47** Neural input to the horizontal saccade system. (Top) Agonist input. (Middle) Antagonist input. (Bottom) Discharge rate of a single burst-tonic neuron during a saccade (agonist input). Details of the experiment and training for the bottom diagram are reported elsewhere. *From Sparks et al. [44]. Data provided personally by Dr. David Sparks.*

includes a PIRB pulse with duration of  $T_4 - T_3$ . At  $T_4$ , the antagonist input exponentially decays to  $F_{ts}$ , with a time constant  $\tau_{tn3}$ . If no PIRB occurs in the antagonist input, the input exponentially rises to  $F_{ts}$  with time constant  $\tau_{tn2}$ .

The agonist pulse includes an interval ( $T_1$ ) that is constant for saccades of all sizes as supported by physiological evidence [11, 50]. We choose to model the change in the firing rate with an exponential function because this seems to match the data fairly well.

After complete inhibition, the antagonist neural input has a brief excitatory pulse starting at  $T_3$  with duration of approximately 10 ms. Enderle proposed that this burst is generated by PIRB, a property that contributes to the postsaccade phenomena such as dynamic and glissadic overshoot (2002). The active-state tensions are again defined as low-pass filtered neural signals:

$$\dot{F}_{ag} = \frac{N_{ag} - F_{ag}}{\tau_{ag}} \quad (13.52)$$

$$\dot{F}_{ant} = \frac{N_{ant} - F_{ant}}{\tau_{ant}} \quad (13.53)$$

where

$$\tau_{ag} = \tau_{gac}(u(t - T_1) - u(t - T_2)) + \tau_{gde}u(t - T_2) \quad (13.54)$$

$$\tau_{ant} = \tau_{tde}(u(t) - u(t - T_3)) + \tau_{tac}(u(t - T_3) - u(t - T_4)) + \tau_{tde}u(t - T_4) \quad (13.55)$$

The activation and deactivation time constants represent the different dynamic characteristics of muscle under increasing and decreasing stimulation.

### 13.8.2 Parameter Estimation and System Identification

The model presented here involves a total of 25 parameters describing the oculomotor plant, neural inputs, and active-state tensions that are estimated by system identification. Initial estimates of the model parameters are important, since they affect the convergence of the estimation routine. In this model, the initial estimates are derived from previously published experimental observations, with a more detailed discussion of the parameter estimates for human and monkey given in Zhou, Chen, and Enderle [50] and Enderle and Zhou [18]. Oculomotor parameters are given in [Table 13.1](#). The transfer function for the oculomotor plant is

$$H(s) = \frac{\theta}{\Delta F} = \frac{\delta B_2 \left( s + \frac{K_{se}}{B_2} \right)}{s^3 + P_2 s^2 + P_1 s + P_0} \quad (13.56)$$

where  $\Delta F = F_{ag} - F_{ant}$ . Using the parameter values in [Table 13.1](#), we have the transfer function for humans as

$$H(s) = \frac{1.9406 \times 10^5 (s + 250)}{s^3 + 596s^2 + 1.208 \times 10^5 s + 1.3569 \times 10^6} \quad (13.57)$$

**TABLE 13.1** Comparison of Parameters for Monkeys and Humans

| Parameter         | Human   | Rhesus Monkey   |
|-------------------|---|---|
| Radius of eyeball | 11 mm (11.8 mm in model)  | 10 mm   |
| $K_{se}$          | 125 N/m   | 125 N/m   |
| $K_{lt}$          | 60.7 N/m  | 77.66 N/m   |
| $B_1$             | 5.6 Ns/m  | 4 Ns/m  |
| $B_2$             | 0.5 Ns/m  | 0.4 Ns/m  |
| $F$               | $F = \begin{cases} 0.4 + 0.0175 \theta , & \text{for } \theta > 0 \\ 0.4 - 0.0125 \theta , & \text{for } \theta \leq 0 \end{cases}$ | $F = \begin{cases} 0.55 + 0.0175 \theta , & \text{for } \theta > 0 \\ 0.55 - 0.0125 \theta , & \text{for } \theta \leq 0 \end{cases}$ |
| $K$               | 16.34 N/m   | 10.21 N/m   |
| $B$               | 0.327 Ns/m  | 0.204 Ns/m  |
| $J$               | $2.2 \times 10^{-3}$ Ns <sup>2</sup> /m   | $1.76 \times 10^{-3}$ Ns <sup>2</sup> /m  |

and for monkeys

$$H(s) = \frac{2.6904 \times 10^5(s + 312.5)}{s^3 + 575.2s^2 + 1.4829 \times 10^5s + 2.7743 \times 10^6} \quad (13.58)$$

There are three poles and the one zero in the transfer function. Using the parameter values in [Table 13.1](#) for humans, the poles are

$$\begin{aligned} &-292.22 + j168.63 \\ &-292.22 - j168.63 \\ &-11.92 \end{aligned}$$

and the zero is

$$250$$

For monkeys, the poles are

$$\begin{aligned} &-277.48 + j245.09 \\ &-277.48 - j245.09 \\ &-20.24 \end{aligned}$$

and the zero is

$$312.5$$

For humans, the time constant for the real pole is 3.4 ms, and the time constant for the complex pole is -83.9 ms. Similarly, for monkeys we have 3.6 and 49.4 ms.

## EXAMPLE PROBLEM 13.8

Consider the oculomotor system shown in Figure 13.46 and Eq. (13.51). Given the following initial conditions and parameter, create a SIMULINK program and plot the neural inputs, active-state tensions, position, velocity, and acceleration.

$$\begin{aligned} \theta(0) &= 0^\circ, \dot{\theta}(0) = 0^\circ\text{s}^{-1}, \ddot{\theta}(0) = 0^\circ\text{s}^{-2}, T_1 = 0.0044 \text{ s}, T_2 = 0.0259 \text{ s}, T_3 = 0.0293 \text{ s}, \\ T_4 &= 0.0462 \text{ s}, F_{p1} = 1.06 \text{ N}, F_{p2} = 0.9331 \text{ N}, F_{p3} = 0.3790 \text{ N}, F_{g0} = 0.4 \text{ N}, F_{gs} = 0.5546 \text{ N}, \\ F_{t0} &= 0.4 \text{ N}, F_{ts} = 0.2895 \text{ N}, \tau_{gn1} = 0.000287 \text{ s}, \tau_{gn2} = 0.0034 \text{ s}, \tau_{gn3} = 0.0042 \text{ s}, \\ \tau_{gac} &= 0.0112 \text{ s}, \tau_{tn1} = 0.000939 \text{ s}, \tau_{tn2} = 0.0012 \text{ s}, \tau_{tn3} = 0.001 \text{ s}, \tau_{tac} = 0.0093 \text{ s}, \\ \tau_{tde} &= 0.0048 \text{ s}, K_{se} = 124.9582 \text{ Nm}, K_{lt} = 60.6874 \text{ Nm}, K = 16.3597 \text{ Nm}, \\ B_1 &= 5.7223 \text{ Nms}^{-1}, B_2 = 0.5016 \text{ Nms}^{-1}, B = 0.327 \text{ Nms}^{-1}, J = 0.0022 \text{ Nms}^{-1}, \\ \text{and radius} &= 0.0118 \text{ m}. \end{aligned}$$

### Solution

We first compute the following intermediate results in MATLAB:

```
b12=b1+b2=6.2239
kst=kse+klt=185.6456
c3=b12*j=0.0137
c2=b12*bp+kst*j+2*b1*b2=8.1855
c1=b12*kp+kst*bp+2*(b2*klt+b1*kse)=1.6535e+003
c0=kst*kp+2*kse*klt=1.8204e+004
delta=57.296/(r*c3)= 3.5397e+005
p2=c2/c3=596.7159
p1=c1/c3=1.2054e+005
p0=c0/c3=1.3271e+006
```

The SIMULINK model is shown in Figure 13.48. The diagram in (a) is implemented using Eq. (13.51). The input to the oculomotor plant is shown in diagram (b), with the agonist and antagonist active-state tensions shown in (c) and (d) based on Eqs. (13.52) and (13.53), respectively. The agonist and antagonist neural input is shown in Figures 13.48e and f.

Figure 13.49 shows plots of position, velocity, acceleration, agonist neural input and active-state tension, and antagonist neural input and active-state tension. From the antagonist neural input and active-state tension plot, it is clear that the eye movement has postsaccade behavior. Peak return velocity is  $-20^\circ\text{s}^{-1}$  in Figure 13.49b, which makes it a glissade.

*Continued*

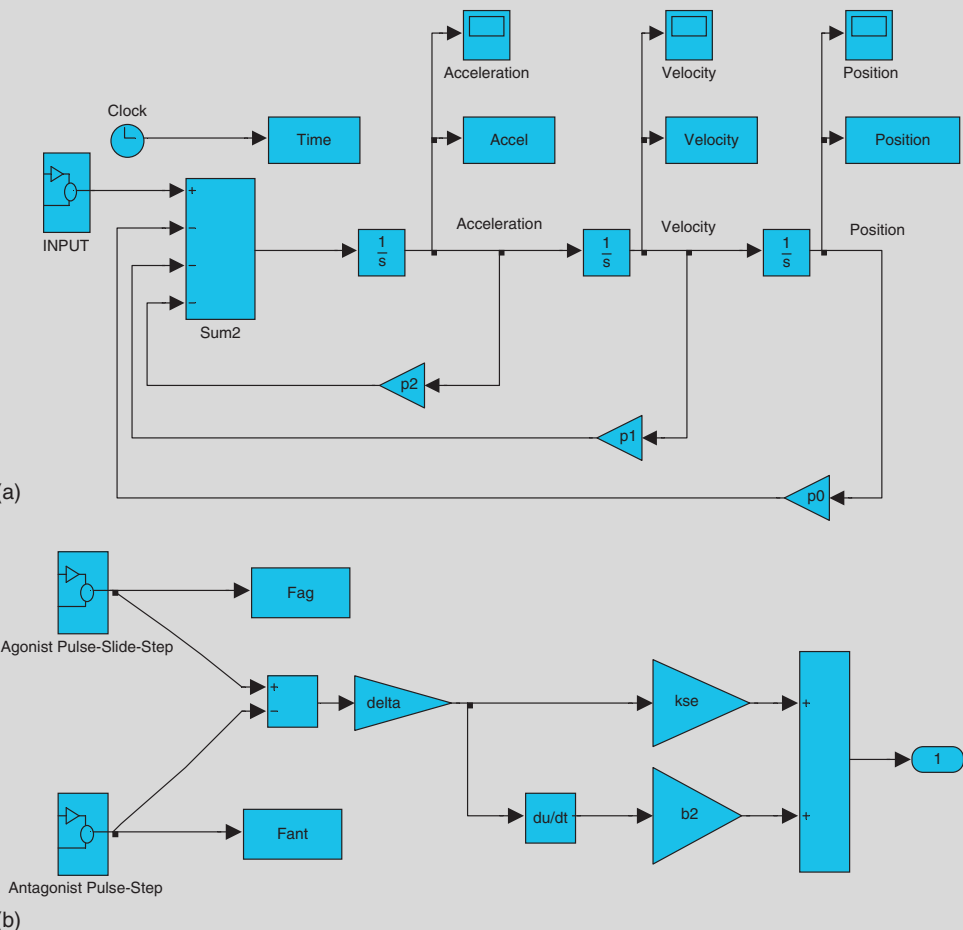


FIGURE 13.48 SIMULINK program for Example 13.8. (a) Main program. (b) Input to plant.

*Continued*

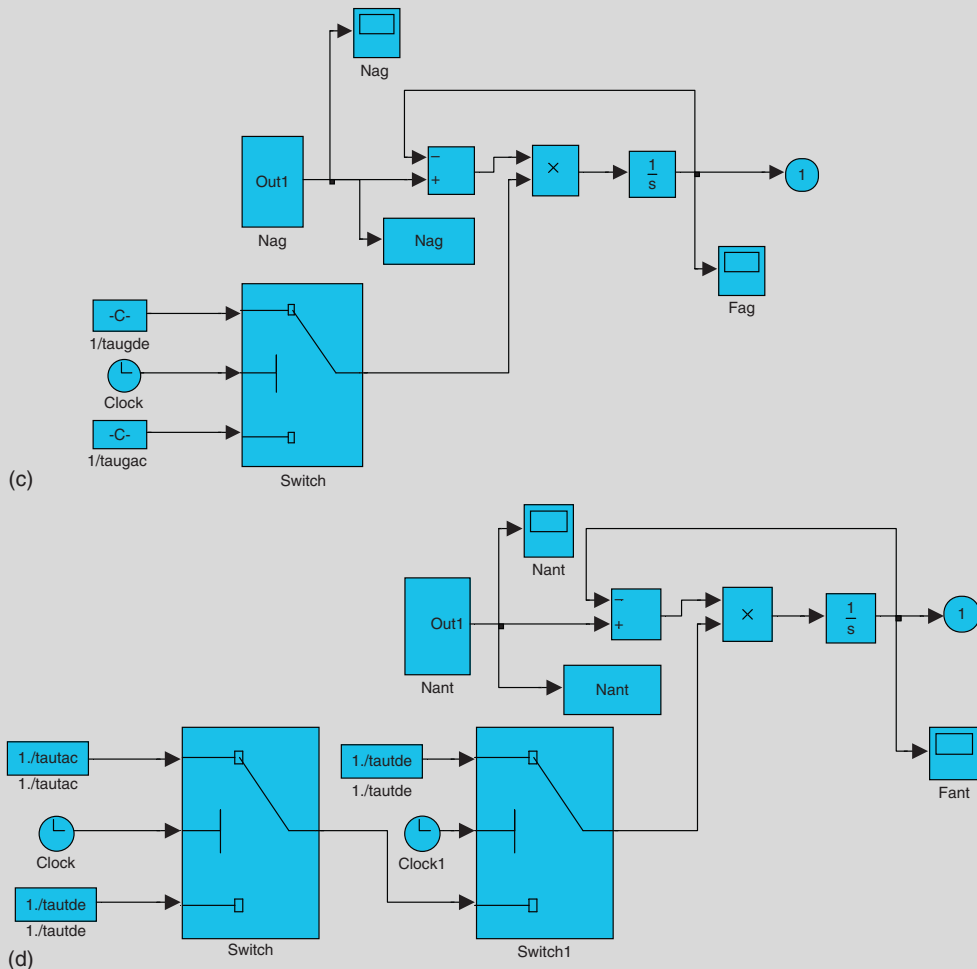


FIGURE 13.48, cont'd (c) Agonist active-state tension. (d) Antagonist active-state tension.

*Continued*

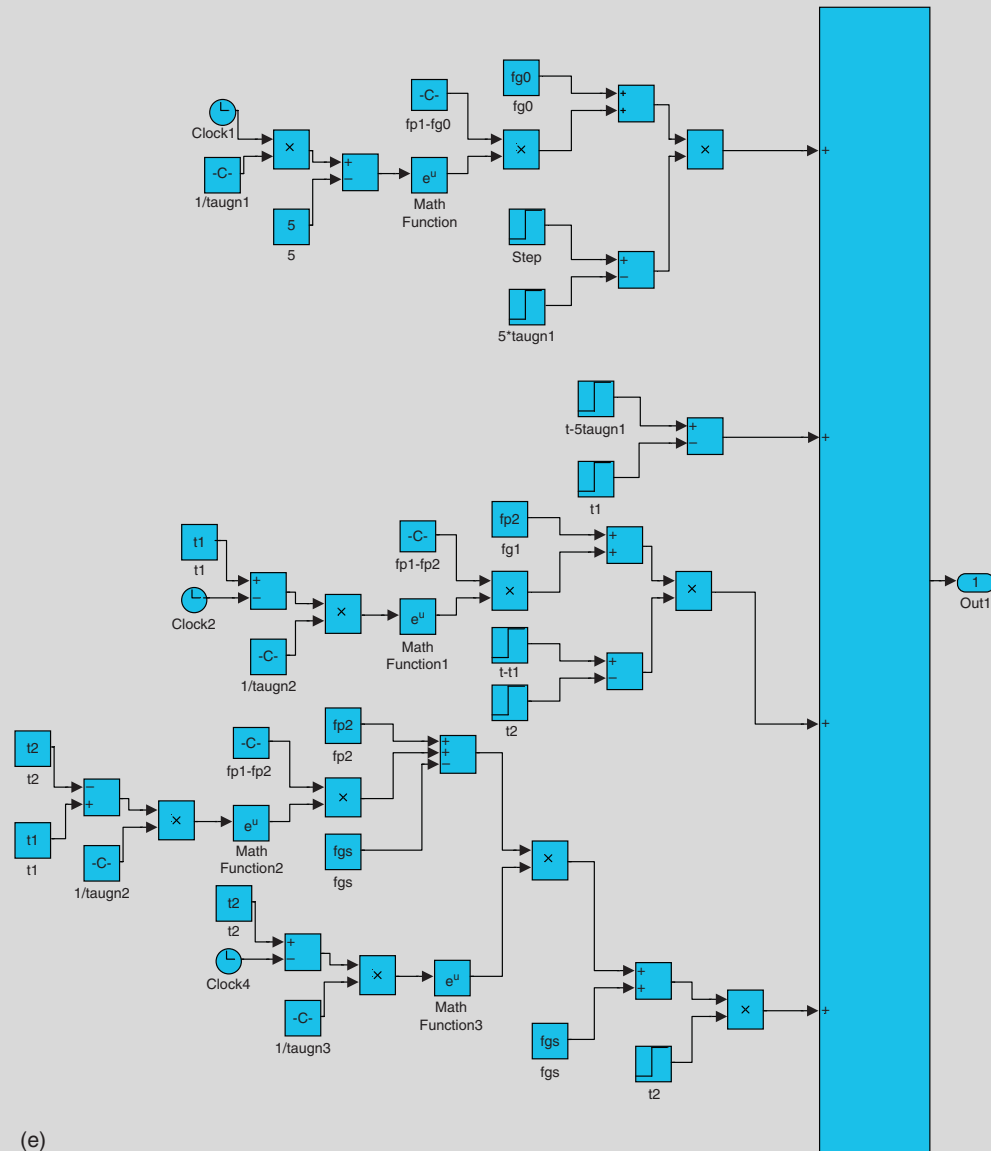


FIGURE 13.48, cont'd (e) Agonist neural input.

*Continued*

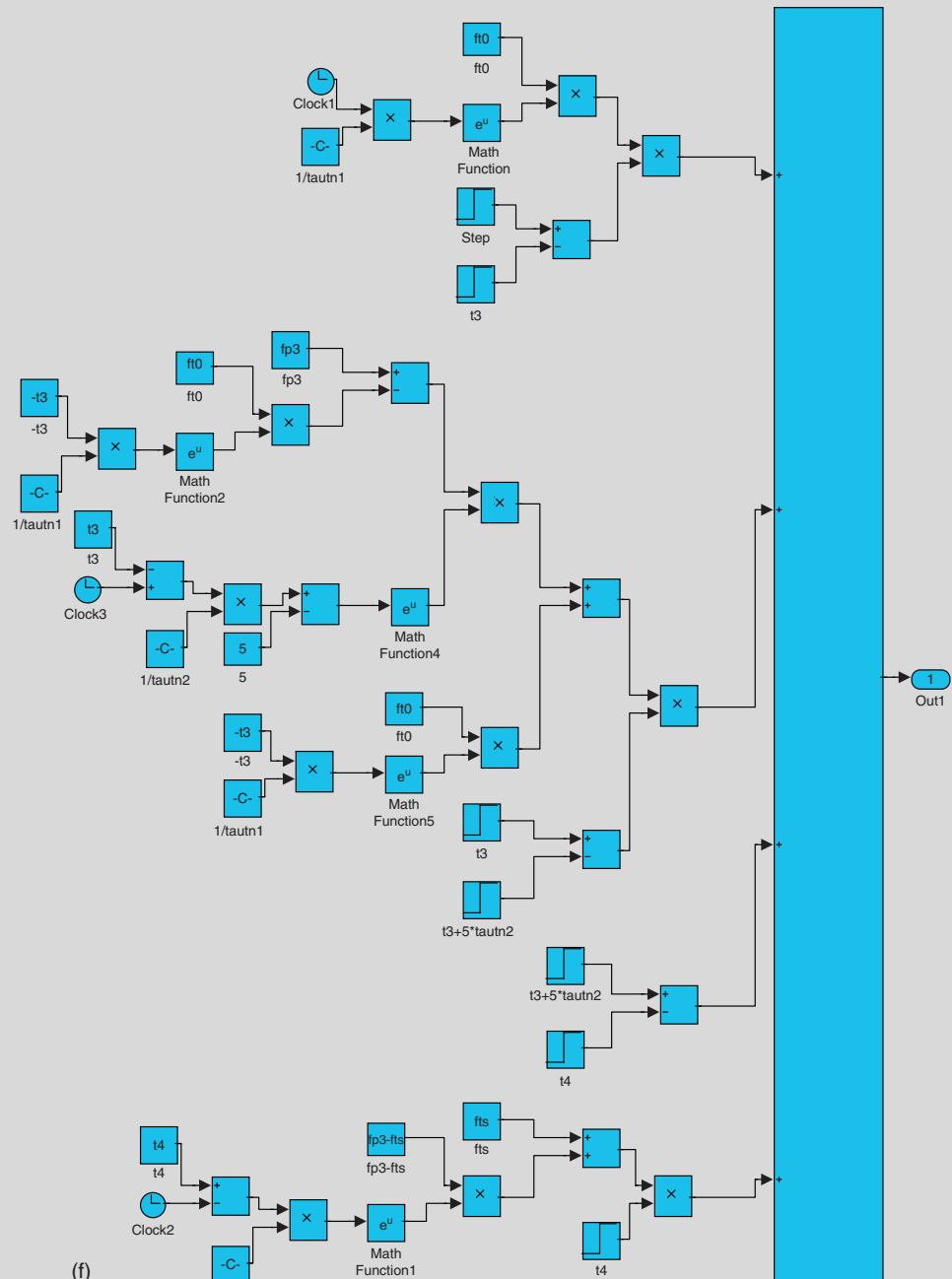
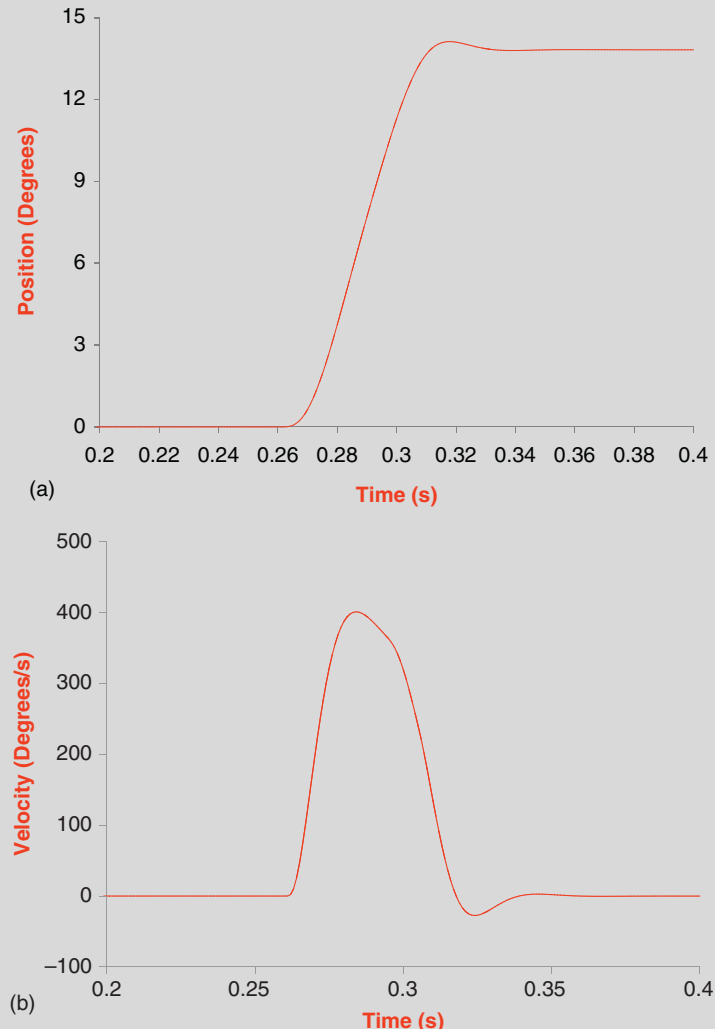


FIGURE 13.48, cont'd (f) Antagonist neural input.



**FIGURE 13.49** Plots of position, velocity, and acceleration (a–c) for Example Problem 13.8. Plots of agonist neural input and active-state tension, and antagonist neural input and active-state tension for Example Problem 13.8, (d) and (e).

*Continued*

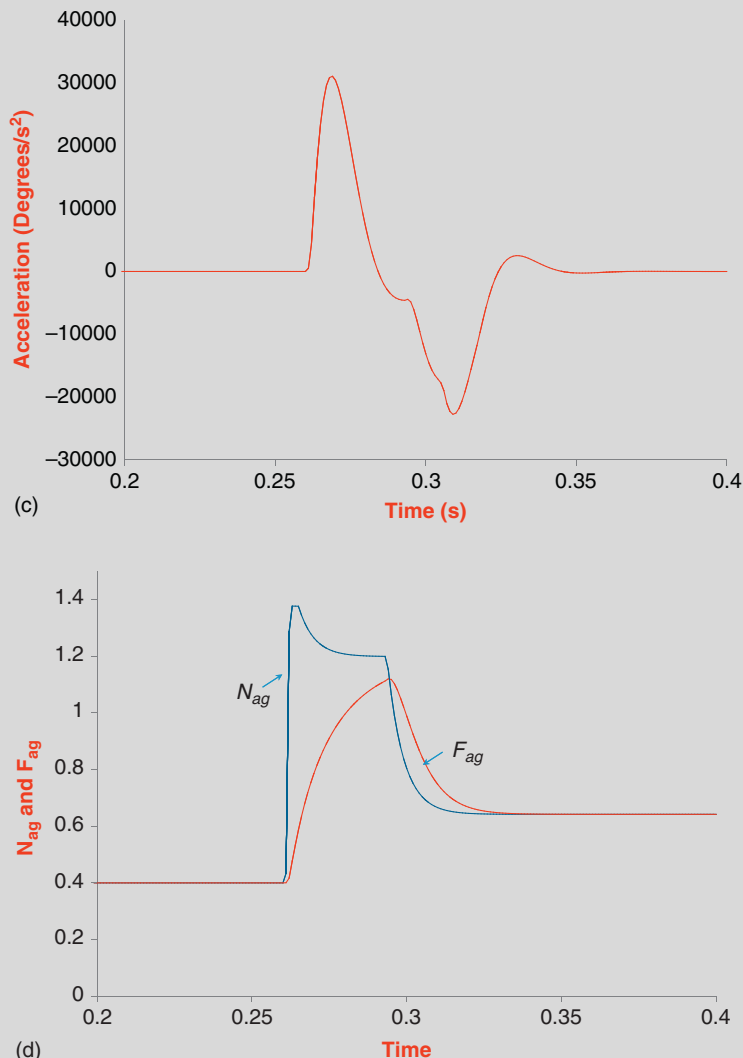


FIGURE 13.49, cont'd

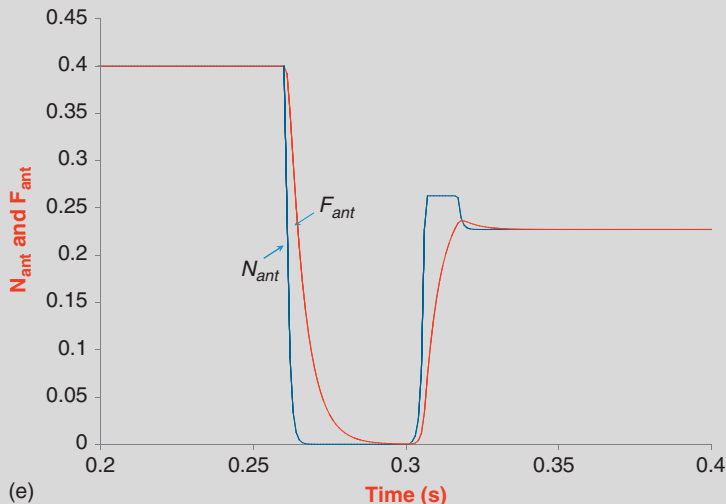


FIGURE 13.49, cont'd

### 13.8.3 Monkey Data and Results

Data<sup>1</sup> were collected from a rhesus monkey that executed a total of 27 saccades in our data set for 4°, 8°, 16°, and 20° target movements. Neuron data were recorded from the long lead burst neuron (5 saccades), excitatory burst neuron (17 saccades), and the agonist burst-tonic neuron (5 saccades) (the neuron types are described in Section 13.9). The firing of the burst-tonic neuron is similar to the motoneuron that drives the agonist muscle during a saccade. Figure 13.50 shows the estimation results for three saccades (4°, 8°, and 15°).

Figure 13.51 shows the estimated neural inputs and active-state tensions that generate the saccades shown in Figure 13.50. Also shown are the firing rates recorded from a single burst-tonic cell in a rhesus monkey for these saccades, scaled to match the height of  $N_{ag}$ . The shapes of the model's neural inputs approximate the burst-tonic data during the pulse and slide very closely. The estimated agonist neural input  $N_{ag}$  clearly has a similar shape to the firing rate data. It should be noted that the firing activity in the data comes from a single burst-tonic neuron. The neural input to the oculomotor plant is actually due to the firing of more than 1,000 motoneurons.

### 13.8.4 Human Data and Results

Data<sup>2</sup> were collected from three human subjects executing 127 saccades, many with dynamic overshoots or glissades. Figure 13.52 shows representative model estimates of saccades generated with a dynamic overshoot, a glissadic overshoot, and normal characteristics.

<sup>1</sup>Details of the experiment and training are reported in Sparks et al. [44]. Data provided personally by Dr. David Sparks.

<sup>2</sup>Details of the experiment are reported in Enderle and Wolfe [17].

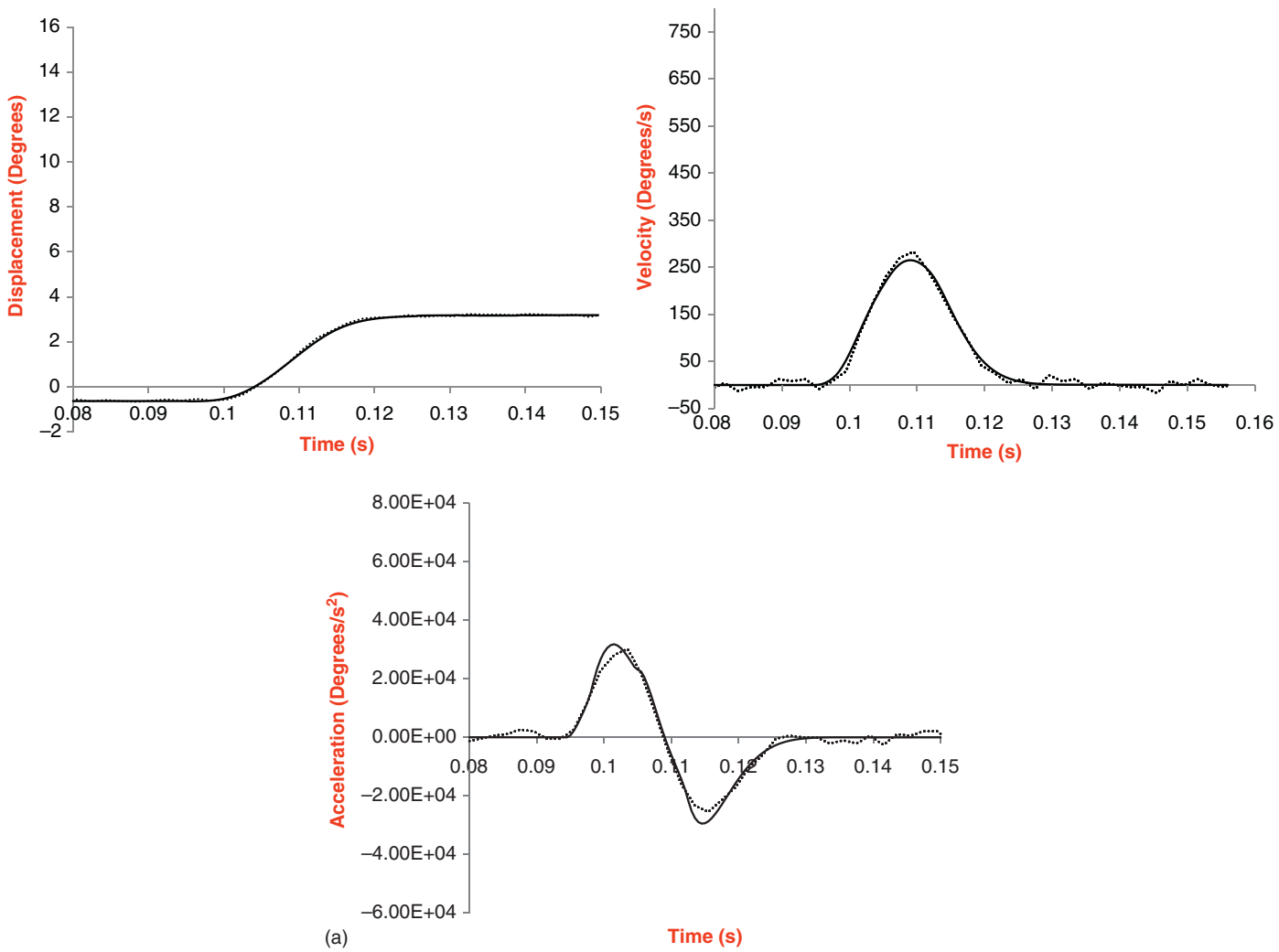


**FIGURE 13.50** Eye position, velocity, and acceleration for three different saccades in a rhesus monkey (a:  $4^\circ$ , b:  $8^\circ$ , and c:  $15^\circ$ ). The solid lines are the model predictions, and the dotted lines are the experimental data during the saccadic eye movement.

*Continued*

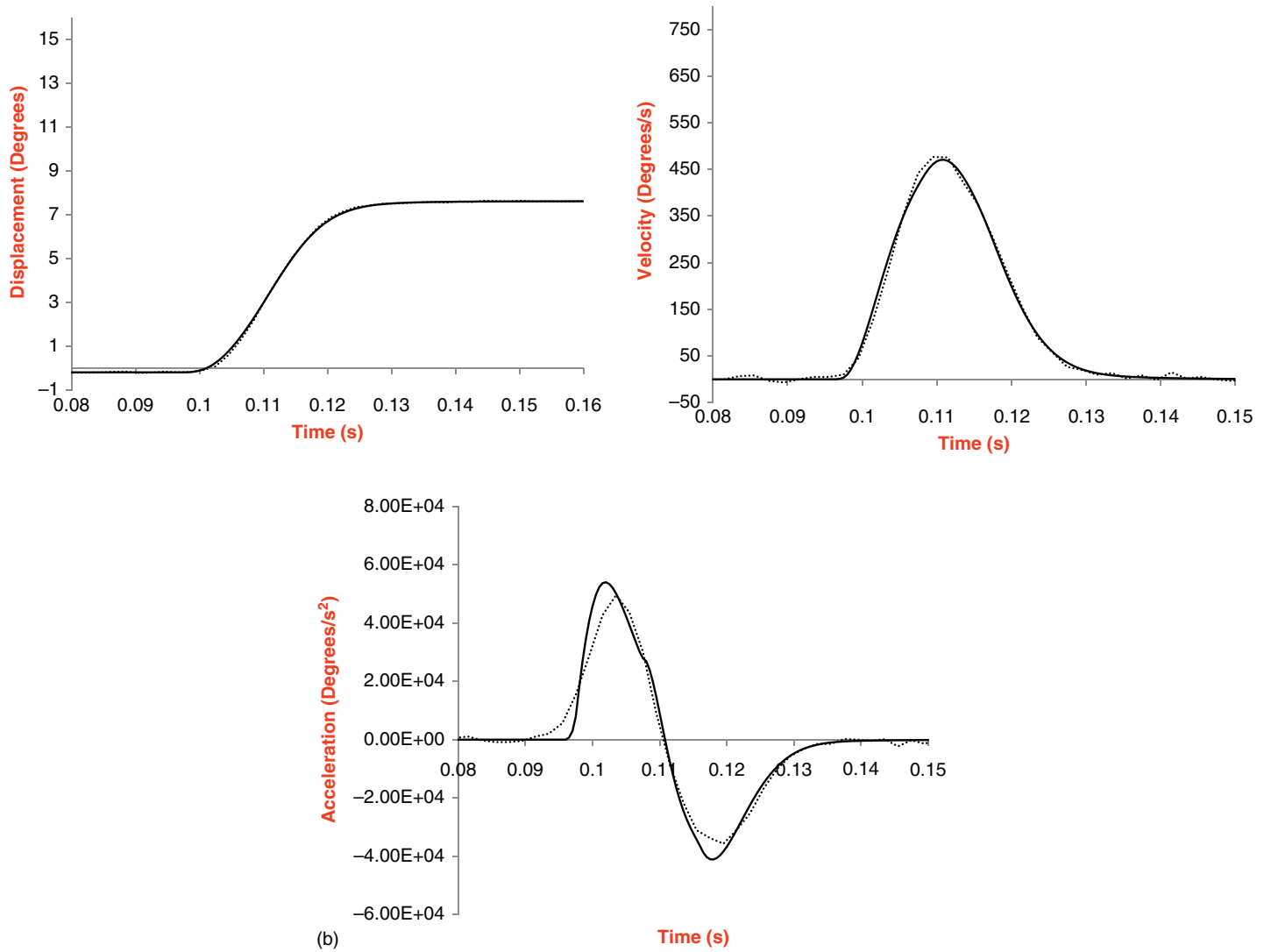


FIGURE 13.50, cont'd

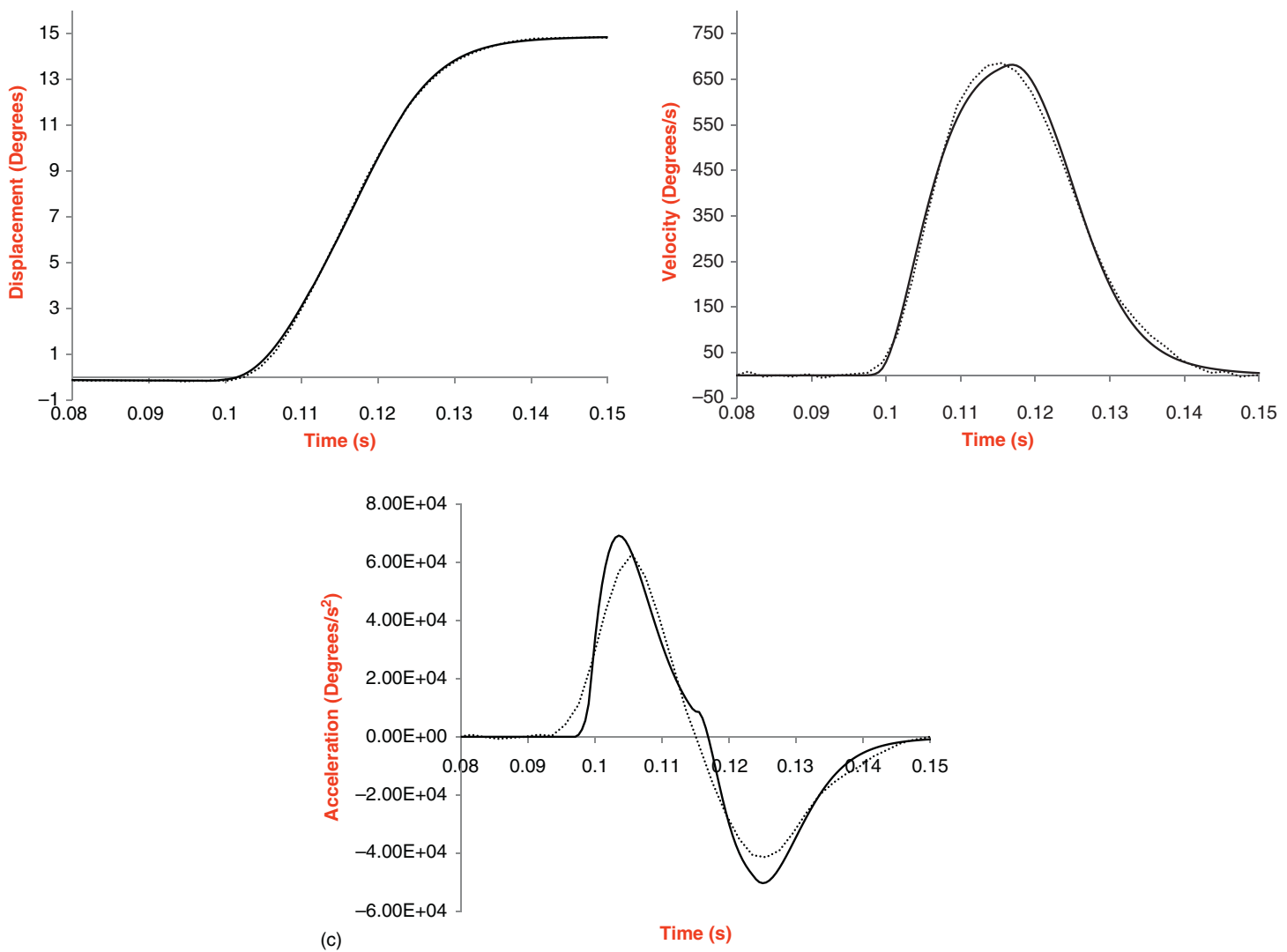


FIGURE 13.50, cont'd

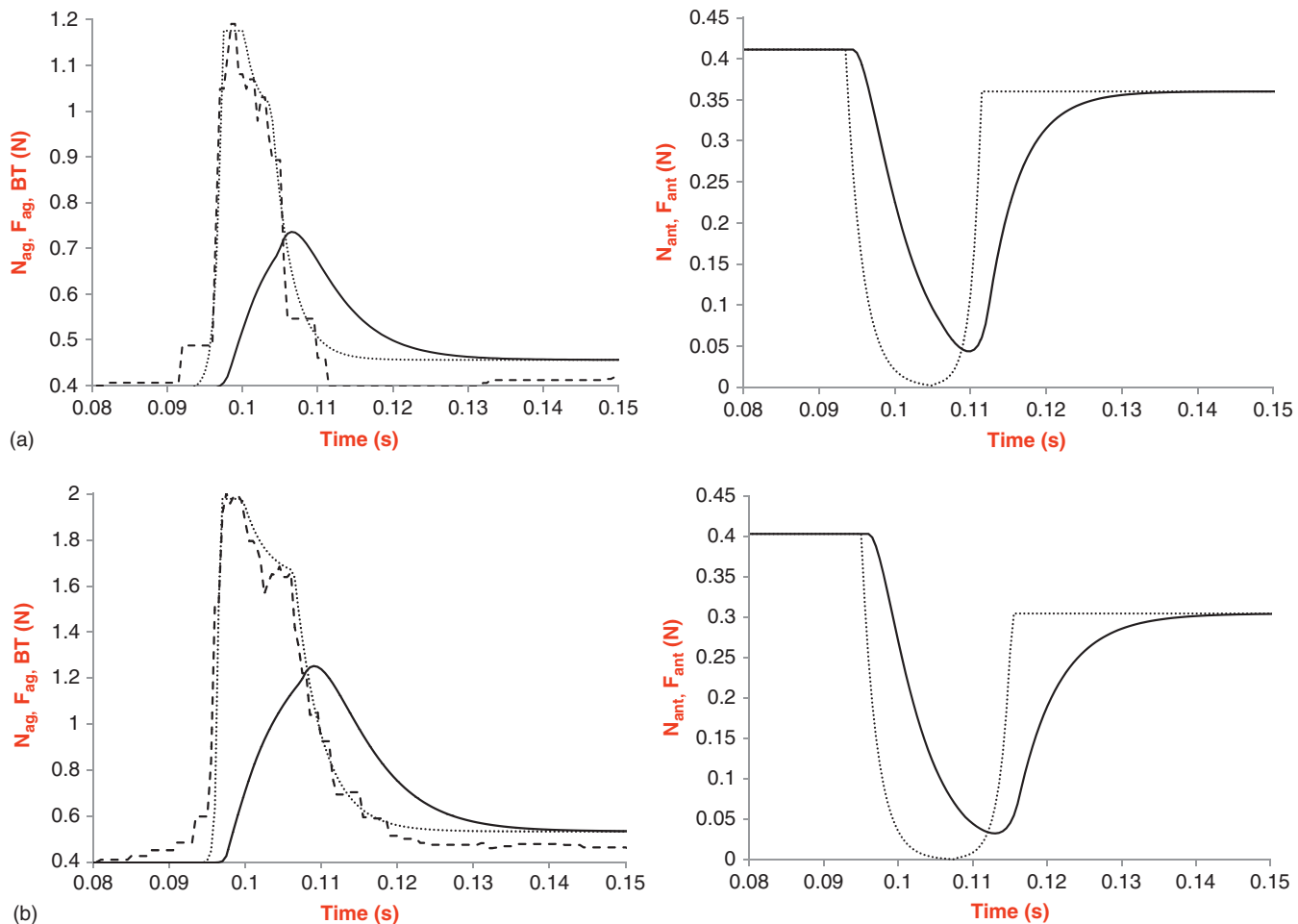


FIGURE 13.51 The estimated agonist and antagonist neural inputs  $N_{ag}$  and  $N_{ant}$  (dotted line), and active-state tension  $F_{ag}$  and  $F_{ant}$  (solid line) for the three saccades (a: 4°, b: 8°, and c: 15°) shown in Figure 13.52. Also shown are the firing rates recorded from a single burst-tonic cell in a rhesus monkey (dashed line) for these saccades, scaled to match the height of  $N_{ag}$ .

Continued

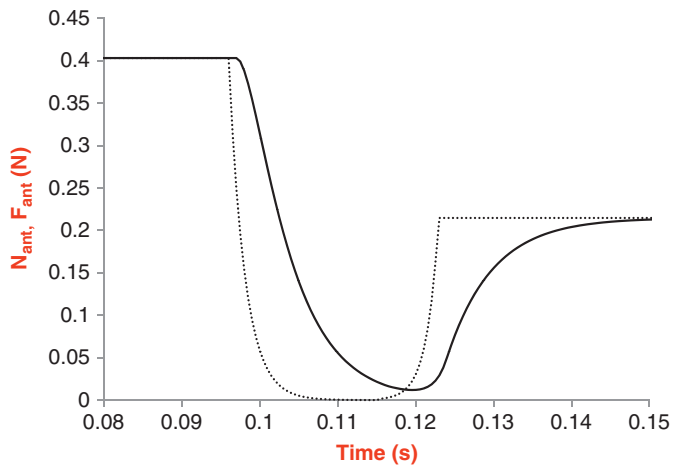
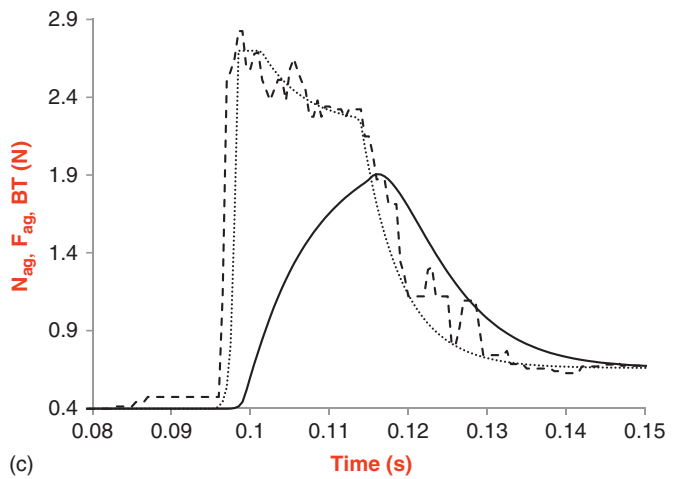
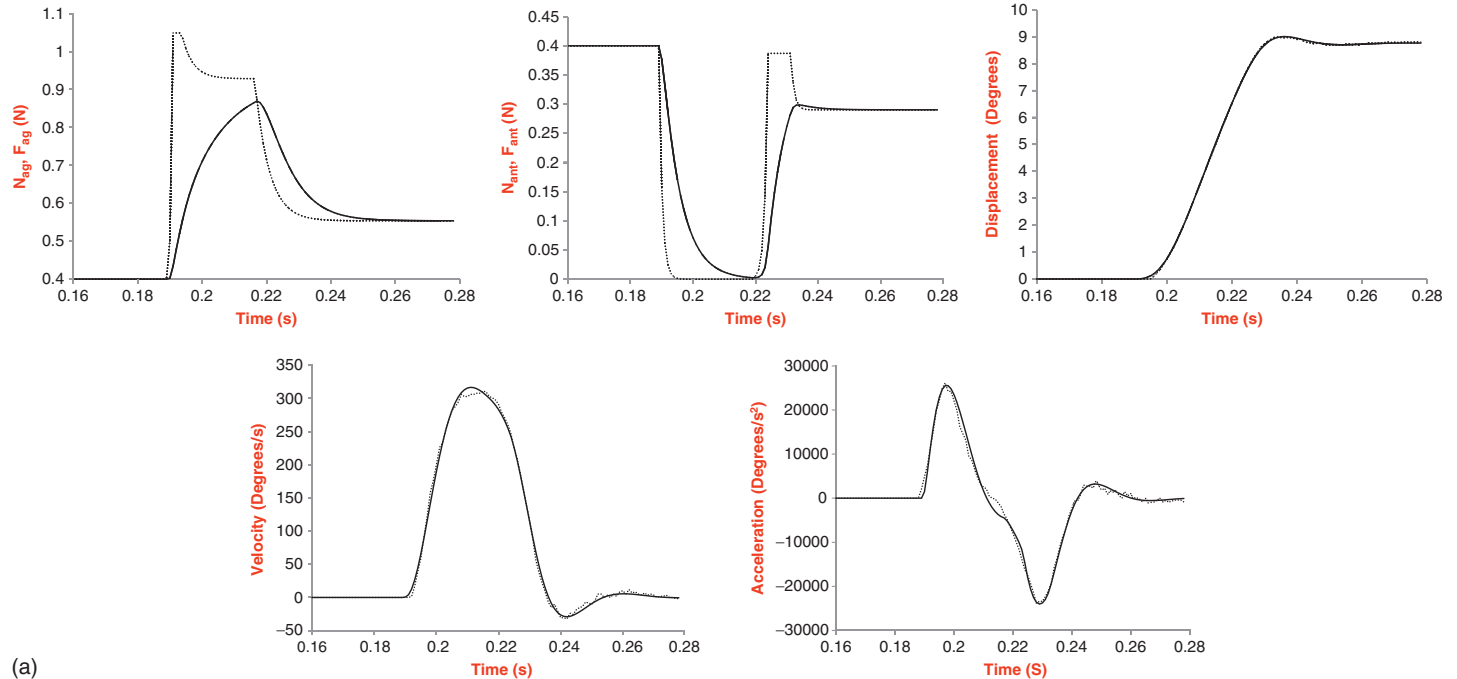


FIGURE 13.51, cont'd



**FIGURE 13.52** (a) Dynamic overshoot saccade of  $8^\circ$ , (b) glissadic overshoot saccade of  $8^\circ$ , and (c) normal  $-12^\circ$  saccade. The first two lines of graphs are the active-state tension (solid line) and neural input (dotted line) calculated from the parameter estimation. Also shown are the model predictions using the parameter estimates from the system identification technique for displacement, velocity, and acceleration and the data (dotted line is the data and solid line is the model predictions).

*Continued*

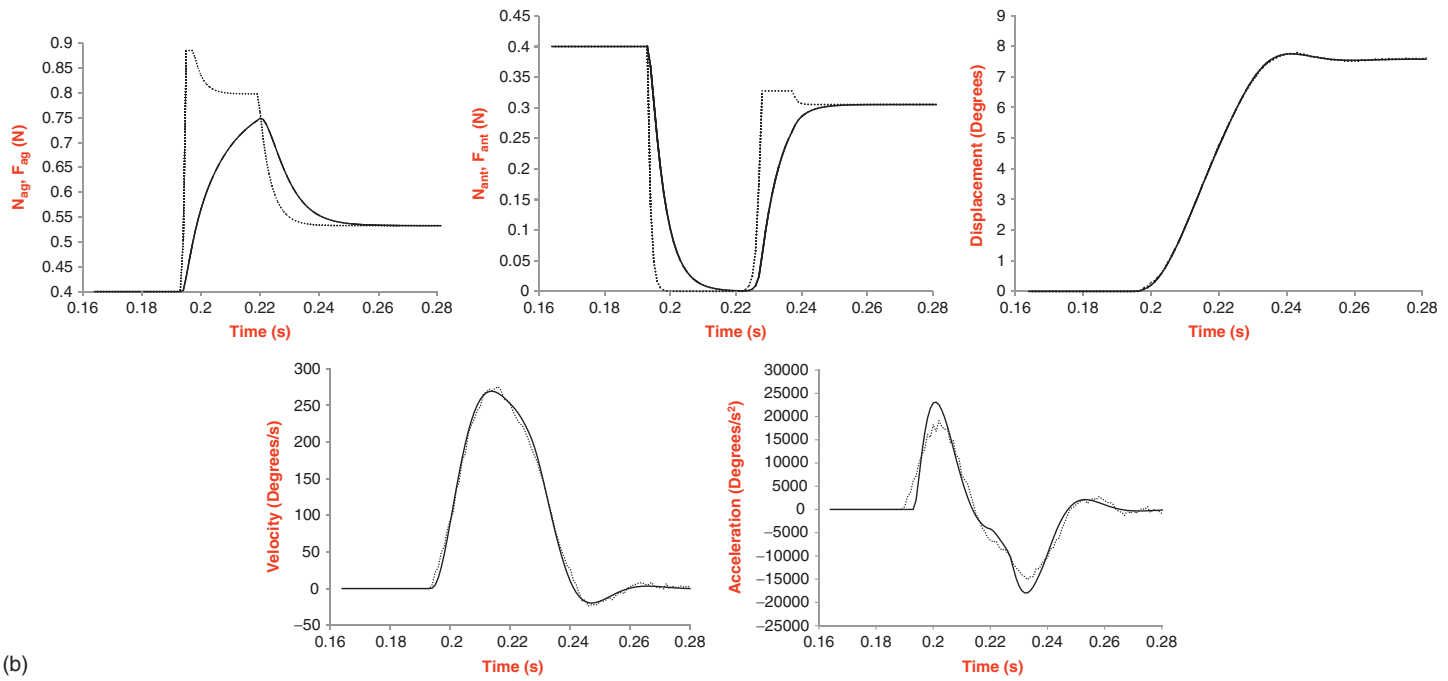


FIGURE 13.52, cont'd

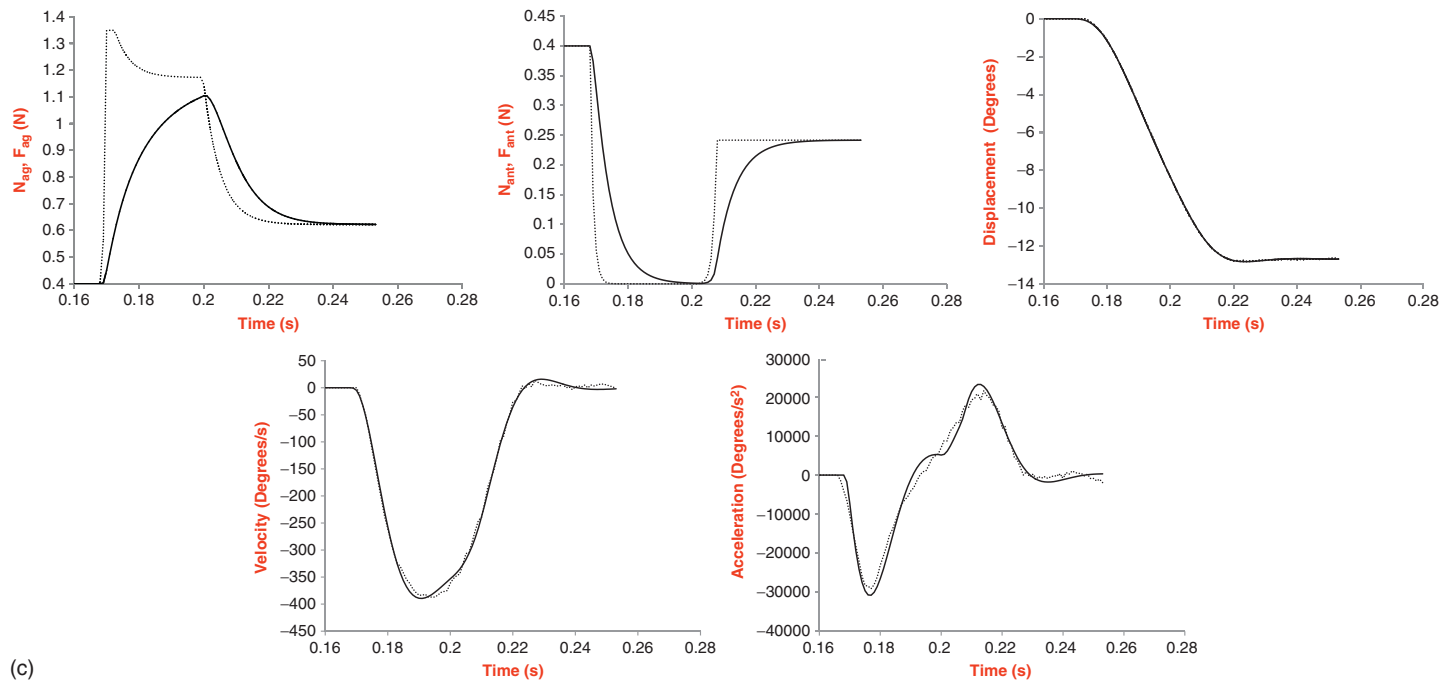


FIGURE 13.52, cont'd

The model predictions for all saccades match displacement data and estimates of velocity very well, including saccades with a dynamic or a glissadic overshoot, with accuracy similar to those in [Figure 13.52](#).

The  $8^\circ$  saccade shown in [Figure 13.52a](#) of data and model predictions has dynamic overshoot. Note that the saccade with dynamic overshoot is caused by a PIRB firing in the antagonist neural input at approximately 220 ms. The PIRB induces prominent reverse peak velocity as shown.

[Figure 13.52b](#) shows model predictions and data for an  $8^\circ$  saccade with glissadic overshoot. The glissade is caused by the PIRB in the antagonist neural input at approximately 223 ms. Notice the peak firing for a saccade with glissadic overshoot is smaller than one with dynamic overshoot. The PIRB induces reverse peak velocity that is smaller than the one with dynamic overshoot. In glissadic overshoot, the eye has an overshoot that returns to steady state more gradually. As a result, the glissade has a smaller peak velocity.

A  $-12^\circ$  normal saccade is shown in [Figure 13.52c](#). Normal saccades usually do not have a PIRB, although this is not absolute, since the timing of the PIRB might offset the impact of the burst.

The main sequence diagram is shown in [Figure 13.53](#). Peak-velocity estimates from the model are in close agreement with the data estimates of peak velocity and follow an exponential shape as a function of saccade magnitude. Duration has a linear relationship with saccade magnitude for saccades above  $7^\circ$ . For saccades between  $3$  to  $7^\circ$ , duration is approximately constant. It should be noted that saccade duration is difficult to determine, especially for small saccades, and may be a source of differences with other published data. The latent period is relatively independent of saccade magnitude.

The estimated agonist pulse magnitudes and durations are shown in [Figure 13.54](#) for all 127 saccades. The agonist pulse magnitude does not significantly increase as a function of saccade magnitude for saccades larger than  $7^\circ$ , consistent with the time-optimal controller proposed by Enderle [11], Zhou and coworkers [50], and Enderle and Zhou [18]. For saccades under  $7^\circ$ , agonist pulse magnitude shows a linear increase in pulse magnitude versus saccade magnitude, again in agreement with our theory for the saccade controller. A great variability is observed in the pulse magnitude estimates for saccades of the same magnitude, which is also observed by Hu and coworkers [34] in their analysis of the firing rates in the monkey EBN. The agonist pulse duration increases as a function of saccade magnitude for saccades larger than  $7^\circ$ . For saccades between  $3$  to  $7^\circ$ , the duration of the agonist pulse is relatively constant as a function of saccade magnitude. Note that for all saccades, the pulse magnitude is tightly coordinated with the pulse duration.

### 13.8.5 Postinhibitory Rebound Burst and Postsaccade Phenomena

Inhibition of antagonist burst neurons<sup>3</sup> is postulated to cause an unplanned postinhibitory rebound burst (PIRB) toward the end of a saccade that causes dynamic overshoots or glissades [11]. While some studies do not observe the rebound firing in the abducens neurons in monkeys [24, 38, 45], PIRB are observed in the abducens motoneurons at the

<sup>3</sup>The neurons described in this section are fully described in Section 14.9, including a neural network. Only a brief description of the neurons involved in PIRB is given here.

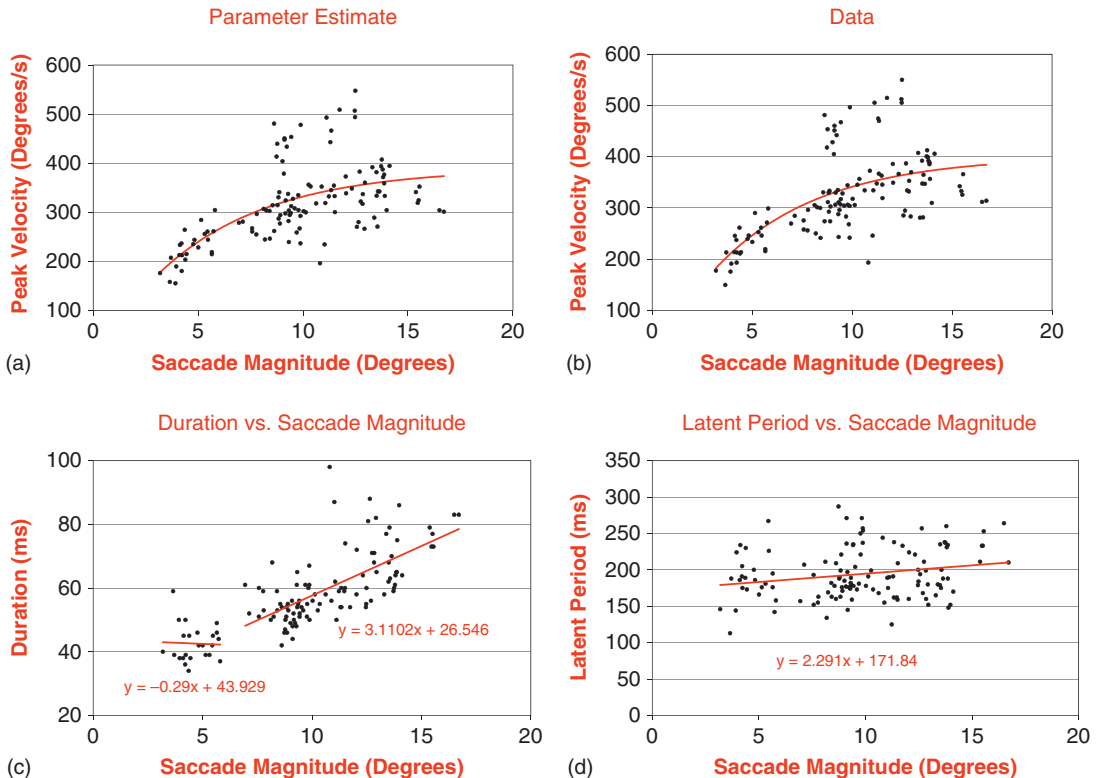


**FIGURE 13.53** Main sequence diagram for all 127 saccades from three human subjects. (a) Peak velocity versus saccade magnitude from the model estimates, with regression fit  $\dot{\theta}_{pv} = 390(1 - e^{-0.2\theta_{ss}})$ . (b) Peak velocity versus saccade magnitude from the data, with regression fit  $\dot{\theta}_{pv} = 401(1 - e^{-0.2\theta_{ss}})$ . (c) Duration versus saccade magnitude based on the data. (d) Latent period versus saccade magnitude based on the data. Note that the parameter estimation program did not update the duration or the latent period, so a single graph for each is drawn.

end of off-saccades in monkeys in other studies (for examples, see [42] and [46]). It was noted earlier that saccades with dynamic overshoots or glissades do not occur with the same frequency in the monkey as in humans, and that they are absent from our monkey data.

The theory presented here is that, at least in humans, the antagonist PIRB causes a reverse peak velocity during dynamic overshoots or glissades in humans. The model predictions accurately match the velocity data for the entire saccade, including saccades with dynamic or glissadic overshoot. We were unable to generate saccades with postsaccade behavior based on just the timing of the antagonist step, but we needed the PIRB to generate saccades with dynamic or glissadic overshoot.

Figures 13.55 and 13.56 summarize the characteristics of the 127 saccades collected from the three human subjects. The number of saccades with a glissade is larger than the number of normal saccades or those with a dynamic overshoot. Additionally, the incidence of dynamic overshoot decreases as saccade size increases. As shown, saccades with a dynamic overshoot typically have larger rebound burst magnitude than those with a glissade or with

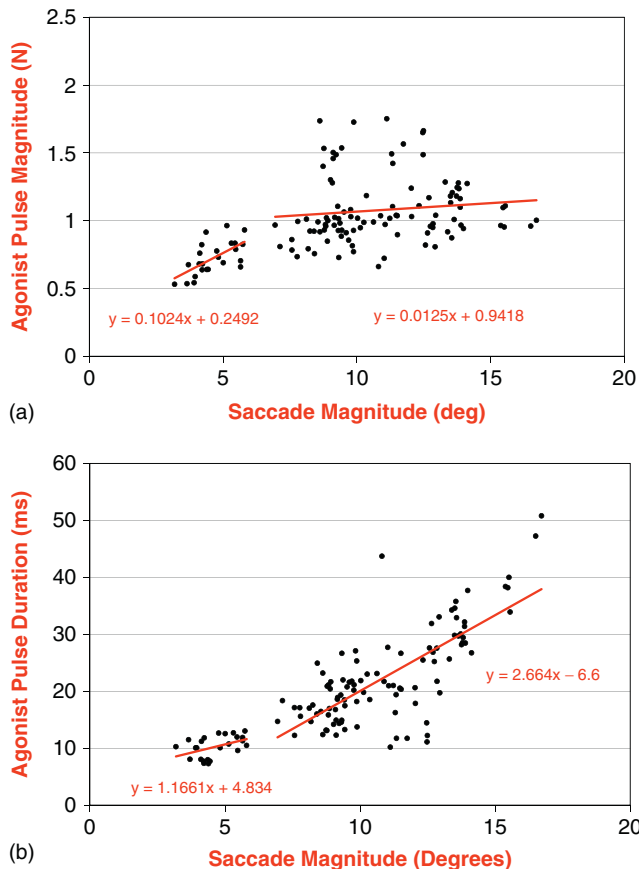


**FIGURE 13.54** Agonist pulse magnitude (a) and duration (b) as functions of saccade magnitude.

normal characteristics. The antagonist onset delay varies from 3 ms to approximately 25 ms. With a larger rebound burst, the onset delay is typically shorter for each type of saccade.

An inherent coordination error exists between the return to tonic firing levels in the abducens and oculomotor motoneurons during the completion of a saccade. During an abducting saccade, ipsilateral abducens motoneurons fire without inhibition and oculomotor motoneurons are inhibited during the pulse phase. Because the IBN inhibits antagonist motoneurons, resumption of tonic firing and PIRB activity in the motoneurons does not begin until shortly after the ipsilateral IBNs cease firing. This same delay exists in the abducens motoneurons for adducting saccades.

There are significantly more internuclear neurons between the contralateral EBN and the TN and the ipsilateral oculomotor motoneurons (antagonist neurons during an abducting saccade) than the ipsilateral EBN and TN and ipsilateral abducens motoneurons (antagonist neurons during an adducting saccade). Due to the greater number of internuclear neurons operating during an abducting saccade, a longer time delay exists before the resumption of activity in the oculomotor motoneurons after the pulse phase for abducting than adducting saccades.

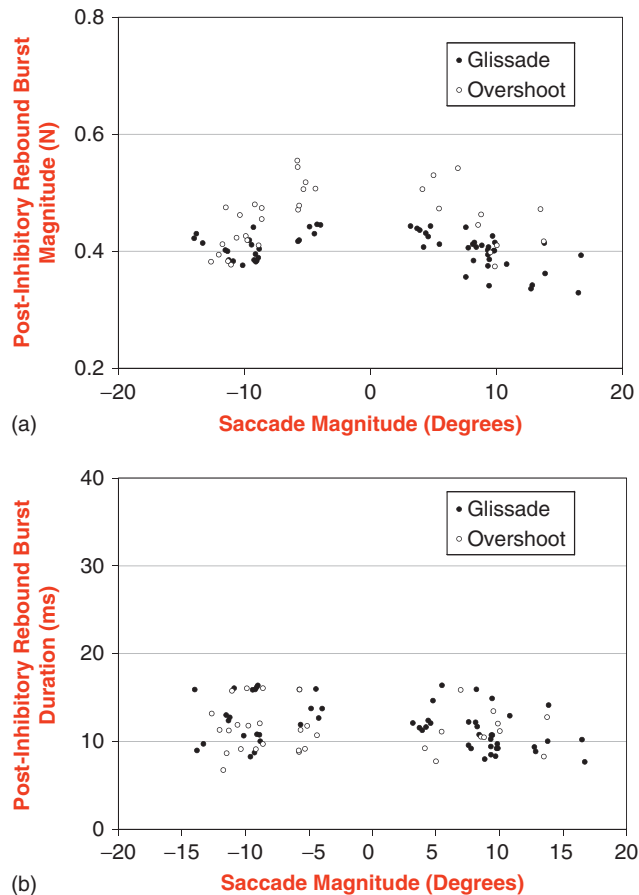


FIGURE 13.55 Postinhibitory rebound burst magnitude (a) and duration (b) as functions of saccade magnitude.

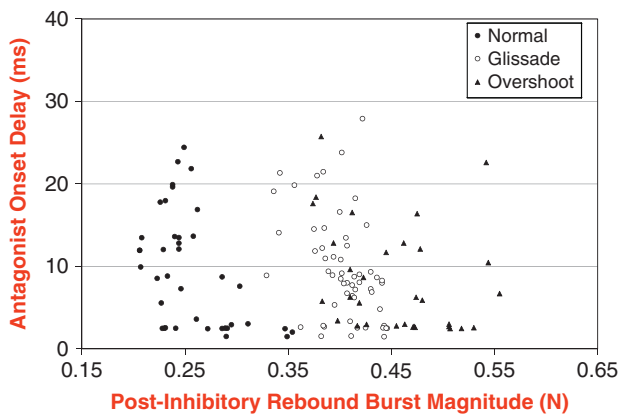


FIGURE 13.56 Postsaccade phenomena involving normal, glissade, and dynamic overshoot saccades.

Since the time delay before the resumption of activity in the oculomotor motoneurons after the pulse phase of a saccade is greater for abducting saccades than with adducting saccades, the incidence of saccades with dynamic overshoot should be greater for abducting saccades than adducting saccades. This is precisely what is observed in saccadic eye movement recordings; most saccades with dynamic overshoot occur in the abducting direction. Additionally, because the contralateral TN's firing rate decreases as ipsilateral saccade amplitude increases, the rate of dynamic overshoot decreases, since fewer saccades have sufficiently high PIRB magnitudes. This is also what is observed in saccadic eye movement recordings.

It is possible for a normal saccade to have a small PIRB as long as the onset delay is small. As the onset delay increases, the PIRB must decrease or a saccade with dynamic or glissadic overshoot occurs.

### 13.8.6 Time-Optimal Controller

The general principle for a time-optimal controller for the horizontal saccade system is that the eyes reach their destination in minimum time that involves over 1,000 neurons. Each neuron contributes to the neural input to the oculomotor plant. Enderle and Wolfe [16] described the time-optimal control of saccadic eye movements with a single switch-time using a linear homeomorphic oculomotor plant for the lateral and medial rectus muscles. Here, we reexamine the 1987 study using the updated oculomotor plant and a time-optimal controller constrained by a more realistic pulse-slide-step motoneuron stimulation of the agonist muscle with a pause and step in the motoneuron stimulation of the antagonist muscle, and physiological constraints.

The time-optimal controller proposed here has a firing rate in individual neurons that is maximal during the agonist pulse and independent of eye orientation, while the antagonist muscle is inhibited. We refer to maximal firing in the neuron as the intent of the system, which, because of biophysical properties of the neuron membrane, slowly decays over time, as described in Enderle [11]. The type of time-optimal controller described here is more complex than the one in 1987 due to physiological considerations. The time-optimal controller operates in two modes: one for small saccades and one for large saccades.

The duration of small saccades has been reported as approximately constant [23, 50, Enderle and Zhou, 2010b], and also as a function of saccade amplitude (e.g., [4]). Estimating the saccade start and end time is quite difficult because it is contaminated by noise. Enderle and coworkers have used a Kaiser filter to reduce the impact of noise, which others may not have implemented, and possibly introduced a difference in results. Moreover, synchrony of firing will have a greater impact on the start time for small saccades than larger saccades, since the beginning of the saccades is much more drawn out, making detection more difficult. In our analysis, a regression fit for the data is carried out in two intervals: one between 3 and 7°, and one for those greater than 7°. Our results indicate an approximately constant duration for small saccades and a duration that increases with saccade size for large saccades. Other investigators have used a single interval for the regression fit to a straight line or a nonlinear function. It is possible that using the technique used here will result in a similar conclusion to ours. Since we did not analyze saccades less than 3°, judgment on saccade duration in this interval is delayed and supports future investigation.

We propose that there is a minimum time period that EBNs can be switched on and off and that this is a physical constraint of the system. As shown in Figure 13.53c, small saccades have approximately the same duration of 44 ms, and they do not significantly change as a function of saccade magnitude. Also note that there is randomness in the response, where saccades with large pulse magnitudes are matched with shorter durations, and vice versa. As the saccade size increases for small saccades, we propose that additional neurons are added to the agonist neural input up to  $7^\circ$ , where above this, all neurons are engaged.

In our model, we sum the input of all active motoneurons into the firing of a single neuron. Thus, as the magnitude of the saccades increases, the firing rate of the single neuron in our model increases up to  $7^\circ$ , after which it is maximal, since all neurons are firing. Keep in mind, however, that the firing rate of a real neuron is maximal and does not change as a function of saccade magnitude, as is easily seen in Figure 4 in Robinson [42] and Figure 2 in Van Gisbergen and coworkers [46]. The overall neural input for the agonist pulse is given by

$$N_{ag} = \begin{cases} N(\theta_T)N_{ag_i} & \theta < 7^\circ \\ N_{ag_{max}} & \theta \geq 7^\circ \end{cases} \quad (13.59)$$

where  $N(\theta_T)$  is the number of neurons firing for a saccade of  $\theta_T$  degrees,  $N_{ag_i}$  is the contribution from an individual neuron, and  $N_{ag_{max}}$  is the combined input from all neurons. For small saccades, the commencement of firing of the individual neurons, or synchrony of firing, has a great impact on the overall neural input, since the period of firing during the pulse is small (10 ms for the estimate in Figure 13.54b). Randomness in the start time among the active neurons means that the beginning of the saccade is more drawn out than if they all started together. For smaller saccades, this may result in an incorrect start time, which then effects the duration. Any lack of synchrony can cause the overall agonist input to be smaller; this is a much larger factor for a small saccade than a large saccade, since the pulse duration is much larger. It is very likely that during a saccade, neurons do not all commence firing at the same instant. This is seen in Figure 13.54b, where there is a small slope to the regression fit.

Above  $7^\circ$ , the magnitude of the saccade is dependent on the duration of the agonist pulse with all neurons firing maximally. The agonist pulse magnitude as shown in Figure 13.54a is approximately a constant according to the regression fit. The duration of the agonist pulse increases as a function of saccade magnitude, as shown in Figure 13.54b.

The saccade controller described here is a time-optimal controller that differs from the one described by Enderle and Wolfe [16] because of the physiology of the system. Active neurons during the pulse phase of the saccade all fire maximally. For saccades greater than  $7^\circ$ , this is the same time-optimal controller described earlier by Enderle and Wolfe [16]. For saccades from 3 to  $7^\circ$ , the system is constrained by a minimum duration of the agonist pulse; saccade magnitude is dependent on the number of active neurons, all firing maximally, consistent with physiological evidence. In terms of control, it is far easier to operate the system for small saccades based on the number of active neurons firing maximally, rather than adjusting the firing rate for all neurons as a function of saccade magnitude as proposed by others. Thus, the system described here is still time-optimal based on physiological constraints.

Generally, saccades recorded for any size magnitude are extremely variable, with wide variations in the latent period, time to peak velocity, peak velocity, and duration. Furthermore, this variability is well coordinated by the neural controller. Saccades with lower peak velocity are matched with longer saccade durations, and saccades with higher peak velocity are matched with shorter saccade durations. Thus, saccades driven to the same destination usually have different trajectories.

### 13.9 SACCADE NEURAL PATHWAYS

Clinical evidence, lesion, and stimulation studies all point toward the participation of vitally important neural sites in the control of saccades, including the cerebellum, superior colliculus (SC), thalamus, cortex, and other nuclei in the brain stem, and that saccades are driven by two parallel neural networks [10, 11, 15, 18, 50]. From each eye, the axons of retinal ganglion cells exit and join other neurons to form the optic nerve. The optic nerves from each eye then join at the optic chiasm, where fibers from the nasal half of each retina cross to the opposite side. Axons in the optic tract synapse in the lateral geniculate nucleus (a thalamic relay) and continue to the visual cortex. This portion of the saccade neural network is concerned with the recognition of visual stimuli. Axons in the optic tract also synapse in the SC. This second portion of the saccade neural network is concerned with the location of visual targets and is primarily responsible for goal-directed saccades.

Saccadic neural activity of the SC and cerebellum, in particular, have been identified as the saccade initiator and terminator, respectively, for a goal-directed saccade. The impact of the frontal eye field and the thalamus, while very important, have less important roles in the generation of goal-directed saccades to visual stimuli. The frontal eye fields are primarily concerned with voluntary saccades, and the thalamus appears to be involved with corrective saccades. [Figure 13.57](#) shows the important sites for the generation of a conjugate goal-directed horizontal saccade in both eyes. Each of the sites and connections detailed in [Figure 13.57](#) is fully supported by physiological evidence. Some of these neural sites will be briefly described herein, with abbreviations provided in [Table 13.2](#).

The Paramedian Pontine Reticular Formation (PPRF) has neurons that burst at frequencies up to 1,000 Hz during saccades and are silent during periods of fixation, and neurons that fire tonically during periods of fixation. Neurons that fire at steady rates during fixation are called tonic neurons (TN) and are responsible for holding the eye steady. The TN firing rate depends on the position of the eye (presumably through a local integrator type network). The TNs are thought to provide the step component to the motoneuron. There are two types of burst neurons in the PPRF: the long-lead burst neuron (LLBN) and a medium-lead burst neuron (MLBN). During periods of fixation, these neurons are silent. The LLBN burst at least 12 ms before a saccade and the MLBN burst less than 12 ms (typically 6–8 ms) before the saccade. The MLBNs are connected monosynaptically with the Abducens Nucleus.

The two types of neurons in the MLBN are the excitatory burst neurons (EBN) and the inhibitory burst neurons (IBN). The EBN and IBN labels describe the synaptic activity upon the motoneurons; the EBNs excite and are responsible for the burst firing, and the IBNs inhibit and are responsible for the pause. A mirror image of these neurons exists on both sides of the midline. The IBNs inhibit the EBNs on the contralateral side.

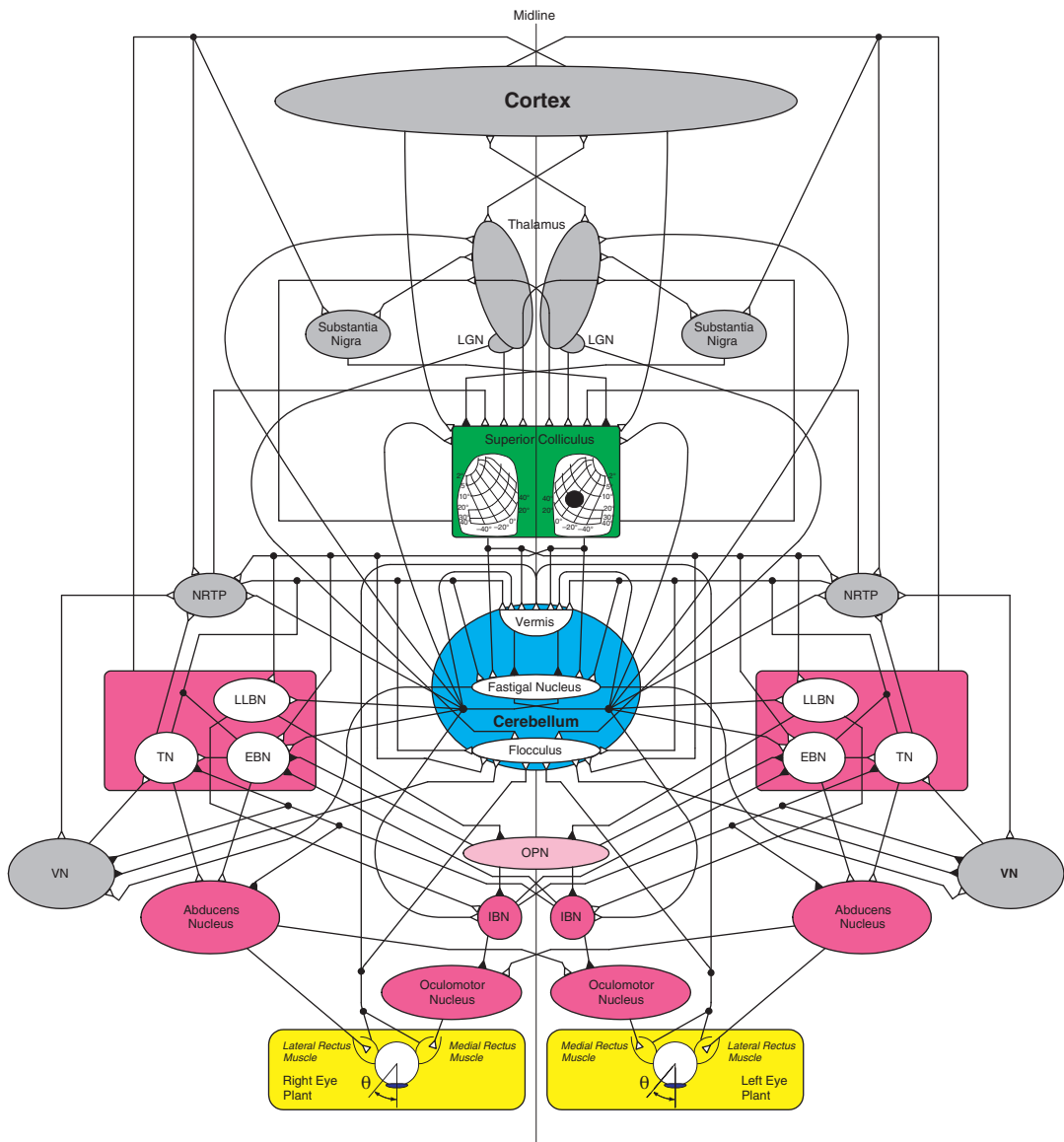


**FIGURE 13.57** The important sites for the generation of a conjugate horizontal saccade in both eyes. Excitatory inputs are shown with  $\nearrow$ , and inhibitory inputs are shown with  $\searrow$ . Consistent with current knowledge, the left and right structures of the neural circuit model are maintained. Since interest is in goal-directed visual saccades, the cortex has not been partitioned into the frontal eye field and posterior eye field (striate, prestriate, and inferior parietal cortices).

**TABLE 13.2** List of Abbreviations

| Neural Site                            | Abbreviation |
|--|--------------|
| Excitatory Burst Neuron                | EBN          |
| Fastigial Nucleus                      | FN           |
| Inhibitory Burst Neuron                | IBN          |
| Long Lead Burst Neuron                 | LLBN         |
| Medium Lead Burst Neuron               | MLBN         |
| Nucleus Reticularis Tegmenti Pontis    | NRTP         |
| Paramedian Pontine Reticular Formation | PPRF         |
| Omnipause Neuron                       | OPN          |
| Substantia Nigra                       | SN           |
| Superior Colliculus                    | SC           |
| Tonic Neuron                           | TN           |
| Vestibular Nucleus                     | VN           |

Also within the brain stem is another type of saccade neuron called the omnipause neuron (OPN). The OPN fires tonically at approximately 200 Hz during periods of fixation and is silent during saccades. The OPN stops firing approximately 10–12 ms before a saccade and resumes tonic firing approximately 10 ms before the end of the saccade. The OPNs are known to inhibit the MLBNs and are inhibited by the LLBNs. The OPN activity is responsible for the precise timing between groups of neurons that causes a saccade.

The SC contains two major functional divisions: a superficial division and an intermediate or deep. Inputs to the superficial division are almost exclusively visual and originate from the retina and the visual cortex. The deep layers provide a site of convergence for sensory signals from several modalities and a source of efferent commands for initiating saccades. The SC is the initiator of the saccade and is thought to translate visual information into motor commands.

The deep layers of the SC initiate a saccade based on the distance between the current position of the eye and the desired target. The neural activity in the SC is organized into movement fields that are associated with the direction and saccade amplitude and does not involve the initial position of the eyeball whatsoever. The movement field is shown in [Figure 13.58](#) for a 20° and 2° saccade. Neurons that are active during a particular saccade are shown as the dark circle. Notice that the movement field for the 2° saccade is smaller than that of the 20° saccade.

Active neurons in the deep layers of the SC generate a high-frequency burst of activity beginning 18–20 ms before a saccade and ending sometime toward the end of the saccade; the exact timing for the end of the burst firing is quite random and can occur slightly before or slightly after the saccade ends. Neurons discharging for small saccades have smaller movement fields, and those for larger saccades have larger movement fields. All of the movement fields are connected to the same set of LLBNs.

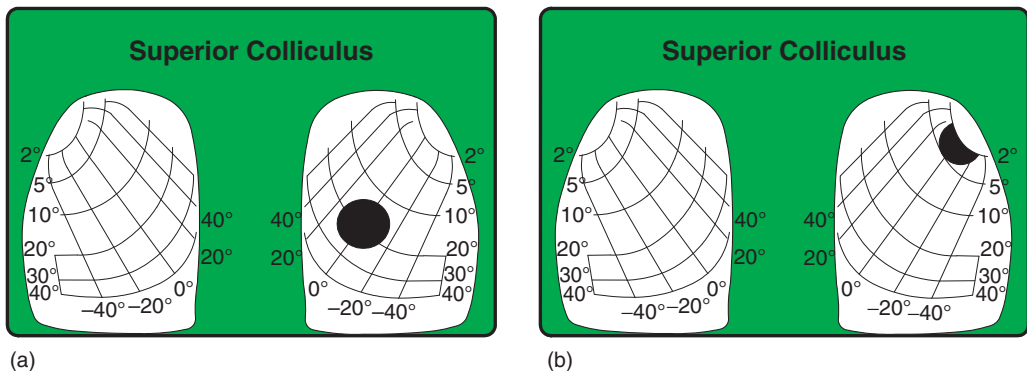


**FIGURE 13.58** A detailed view of the retinotopic mapping over of the superior colliculus for a (a) 20° movement and a (b) 2° movement. Notice the locus of points for the 2° movement is smaller than that for the 20° movement, which implies that fewer neurons are firing for the smaller movement. The movement fields within the superior colliculus also reflect that the number of neurons firing for saccades less than 7° is smaller than those firing for saccades greater than 7°. For saccades above 7°, the movement field is approximately constant.

The cerebellum is responsible for the coordination of movement and is composed of a cortex of gray matter, internal white matter, and three pairs of deep nuclei: fastigial nucleus (FN), the interposed and globose nucleus, and dentate nucleus. The deep cerebellar nuclei and the vestibular nuclei transmit the entire output of the cerebellum. Output of the cerebellar cortex is carried through Purkinje cells. Purkinje cells send their axons to the deep cerebellar nuclei and have an inhibitory effect on these nuclei. The cerebellum is involved with both eye and head movements, and both tonic and phasic activities are reported in the cerebellum. The cerebellum is not directly responsible for the initiation or execution of a saccade but contributes to saccade precision. Sites within the cerebellum important for the control of eye movements include the oculomotor vermis, FN, and the flocculus. Consistent with the operation of the cerebellum for other movement activities, the cerebellum is postulated here to act as the coordinator for a saccade and as a precise gating mechanism.

The cerebellum is included in the saccade generator as a time-optimal gating element, using three active sites during a saccade: the vermis, FN, and flocculus. The vermis is concerned with the absolute starting position of a saccade in the movement field and corrects control signals for initial eye position. Using proprioceptors in the oculomotor muscles and an internal eye position reference, the vermis is aware of the current position of the eye. The vermis is also aware of the signals (dynamic motor error) used to generate the saccade via the connection with the Nucleus Reticularis Tegmenti Pontis (NRTP) and the SC.

With regard to the oculomotor system, the cerebellum has inputs from SC, lateral geniculate nucleus (LGN), oculomotor muscle proprioceptors, and striate cortex via NRTP. The cerebellum sends inputs to the NRTP, LLBN, EBN, VN, thalamus, and SC. The oculomotor vermis and fastigial nuclei are important in the control of saccade amplitude, and the flocculus, perihypoglossal nuclei of the rostral medulla, and possibly the pontine and mesencephalic reticular formation are thought to form the integrator within the cerebellum. One important function of the flocculus may be to increase the time constant of the neural integrator for saccades starting at locations different from primary position.

The FN receives input from the SC, as well as other sites. The output of the FN is excitatory and projects ipsilaterally and contralaterally, as shown in [Figure 13.58](#). During fixation, the FN fires tonically at low rates. Twenty ms prior to a saccade, the contralateral FN bursts, and the ipsilateral FN pauses and then discharges with a burst. The pause in ipsilateral firing is due to Purkinje cell input to the FN. The sequential organization of Purkinje cells along beams of parallel fibers suggests that the cerebellar cortex might function as a delay, producing a set of timed pulses that could be used to program the duration of the saccade. If one considers nonprimary position saccades, different temporal and spatial schemes, via cerebellar control, are necessary to produce the same-size saccade. It is postulated here that the cerebellum acts as a gating device that precisely terminates a saccade based on the initial position of the eye in the orbit.

To execute a saccade, a sequence of complex activities takes place within the brain, beginning from the detection of an error on the retina to the actual movement of the eyes. A saccade is directly caused by a burst discharge (pulse) from motoneurons stimulating the agonist muscle and a pause in firing from motoneurons stimulating the antagonist muscle. During periods of fixation, the motoneurons fire at a rate necessary to keep the eye stable (step). The pulse discharge in the motoneurons is caused by the EBN, and the step discharge is caused by the TN in the PPRF.

Consider the saccade network in [Figure 13.57](#) that is programmed to move the eyes 20°. Qualitatively, a saccade occurs according to the following sequence of events:

1. The deep layers of the SC initiate a saccade based on the distance between the current position of the eye and the desired target. The neural activity in the SC is organized into movement fields that are associated with the direction and saccade amplitude, and it does not involve the initial position of the eyeball whatsoever. Neurons active in the SC during this particular saccade are shown as the dark circle, representing the desired 20° eye movement. Active neurons in the deep layers of the SC generate an irregular high-frequency burst of activity that changes over time, beginning 18–20 ms before a saccade and ending sometime toward the end of the saccade; the exact timing for the end of the SC firing is quite random and can occur either before or after the saccade ends.
2. The ipsilateral LLBN and EBN are stimulated by the contralateral SC burst cells. The LLBN then inhibits the tonic firing of the OPN. The contralateral FN also stimulates the ipsilateral LLBN and EBN.
3. When the OPN cease firing, the MLBN (EBN and IBN) is released from inhibition. Some report that the ipsilateral EBN is probably not stimulated by the SC [25, 39]. This conflict doesn't impact our model as we propose the stimulation of the EBN by other sites does not reflect the firing rate of the EBN, but that the EBN fire autonomously given weak stimulation.
4. The ipsilateral IBN is stimulated by the ipsilateral LLBN and the contralateral FN of the cerebellum. When released from inhibition, the ipsilateral EBN responds with a PIRB for a brief period of time. The EBN when stimulated by the contralateral FN (and perhaps the SC) enables a special membrane property that causes a high-frequency burst that decays slowly until inhibited by the contralateral IBN. The IBN may also have the same type of special membrane properties.
5. The burst firing in the ipsilateral IBN inhibits the contralateral EBN and Abducens Nucleus, and the ipsilateral Oculomotor Nucleus.

6. The burst firing in the ipsilateral EBN causes the burst in the ipsilateral Abducens Nucleus, which then stimulates the ipsilateral lateral rectus muscle and the contralateral Oculomotor Nucleus. With the stimulation of the ipsilateral lateral rectus muscle by the ipsilateral Abducens Nucleus and the inhibition of the ipsilateral rectus muscle via the Oculomotor nucleus, a saccade occurs in the right eye. Simultaneously, the contralateral medial rectus muscle is stimulated by the Contralateral Oculomotor Nucleus, and with the inhibition of the contralateral lateral rectus muscle via the Abducens Nucleus, a saccade occurs in the left eye. Thus, the eyes move conjugately under the control of a single drive center.
7. At the termination time, the cerebellar vermis, operating through the Purkinje cells, inhibits the contralateral FN and stimulates the ipsilateral FN. Some of the stimulation of the ipsilateral LLBN and IBN is lost because of the inhibition of the contralateral FN. The ipsilateral FN stimulates the contralateral LLBN, EBN, and IBN. Further simulation of the contralateral IBN occurs from the contralateral LLBN. The contralateral EBN then stimulates the contralateral Abducens Nucleus. The contralateral IBN then inhibits the ipsilateral EBN, TN, Abducens Nucleus, and contralateral Oculomotor Nucleus. With this inhibition, the stimulus to the agonist muscles ceases. In most saccades, the SC continues to fire even though the saccade has ended.
8. The ipsilateral FN stimulation of the contralateral EBN allows for modest bursting in the contralateral EBN (while still being inhibited by the ipsilateral IBN whose activity has been reduced). This then stimulates the contralateral Abducens Nucleus and ipsilateral Oculomotor Nucleus. With the stimulation from the contralateral EBN through the contralateral Abducens Nucleus and ipsilateral Oculomotor Nucleus, the antagonist muscles fire, causing the antagonist muscles to contract. Once the SC ceases firing, the stimulus to the LLBN stops, allowing the resumption of OPN firing that inhibits the ipsilateral and contralateral MLBN and the saccade ends.

### 13.10 SYSTEM IDENTIFICATION

In traditional applications of electrical, mechanical, and chemical engineering, the main application of modeling is as a design tool to allow the efficient study of the effects of parametric variation on system performance as a means of cost containment. In modeling physiological systems, the goal is not to design a system but to identify the parameters and structure of the system. Ideally, the input and the output of the physiological system are known, and some information about the internal dynamics of the system is available (Figure 13.59). In many cases, either the input or output is not measurable or observable but is estimated from a remote signal, and no information about the system is known. System identification is the process of creating a model of a system and estimating the

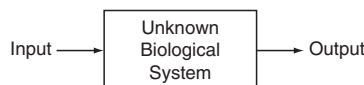


FIGURE 13.59 Block diagram of a typical physiological system without feedback.

parameters of the model. This section introduces the concept of system identification in both the frequency and time domain.

A variety of signals is available to the biomedical engineer, as described earlier. Those produced by the body include action potentials, EEGs, EKGs, EMGs, EOG, and pressure transducer output. Additional signals are available through ultrasound, x-ray tomography, MRI, and radiation. From these signals a model is built and parameters estimated according to the modeling plan in [Figure 13.1](#). Before work on system identification begins, understanding the characteristics of the input and output signals is important as described in Chapter 10—that is, knowing the voltage range, frequency range, whether the signal is deterministic or stochastic, and if coding (i.e., neural mapping) is involved. Most biologically generated signals are low frequency and involve some coding. For example, EEGs have an upper frequency of 30 Hz and eye movements have an upper frequency under 100 Hz. The saccadic system uses neural coding that transforms burst duration into saccade amplitude, as described earlier in this chapter. After obtaining the input and output signals, these signal must be processed. A fundamental block is the amplifier, which is characterized by its gain and frequency, as described in Chapter 8. Note that the typical amplifier is designed as a low-pass filter (LPF), since noise amplification is not desired. Interestingly, most amplifiers have storage elements (i.e., capacitors and inductors), so the experimenter must wait until the transient response of the amplifier has been completed before any useful information can be extracted. An important point to remember is that the faster the cutoff of the filter, the longer the transient response of the amplifier.

In undergraduate classes, a system (the transfer function or system description) and input are usually provided and a response or output is requested. While this seems difficult, it is actually much easier than trying to determine the parameters of a physiological system when all that is known are the input (and perhaps not the direct input as described in the saccadic eye movement system) and noisy output characteristics of the model. In the ideal case, the desired result here is the transfer function, which can be determined from

$$H(s) = \frac{V_o(s)}{V_i(s)} \quad (13.60)$$

### 13.10.1 Classical System Identification

The simplest and most direct method of system identification is sinusoidal analysis. A source of sinusoidal excitation is needed that usually consists of a sine wave generator, a measurement transducer, and a recorder to gather frequency response data. Many measurement transducers are readily available for changing physical variables into voltages, as described in Chapter 9. Devices that produce the sinusoidal excitation are much more difficult to obtain and are usually designed by the experimenter. Recording the frequency response data can easily be obtained from an oscilloscope. [Figure 13.60](#) illustrates the essential elements of sinusoidal analysis.



**FIGURE 13.60** Impulse response block diagram.

The experiment to identify model parameters using sinusoidal analysis is simple to carry out. The input is varied at discrete frequencies over the entire spectrum of interest, and the output magnitude and phase are recorded for each input. To illustrate this technique, consider the following analysis. From Figure 13.60, it is clear that the transfer function is given by

$$H(j\omega) = \frac{V_o(j\omega)}{V_i(j\omega)} \quad (13.61)$$

The Fourier transform of the input is

$$V_i(j\omega) = F\{A \cos(\omega_x t + \theta)\} = A \int e^{-j\omega\lambda} \cos(\omega_x \lambda + \theta) d\lambda = A \int e^{-j\omega\left(-\frac{\theta}{\omega_x} + \tau\right)} \cos(\omega_x \tau) d\tau \quad (13.62)$$

by substituting  $\lambda = \tau - \frac{\theta}{\omega_x}$ . Factoring out the terms not involving  $\tau$ , gives

$$V_i(j\omega) = A e^{\frac{j\omega\theta}{\omega_x}} \int e^{-j\omega\tau} \cos \omega_x \tau d\tau = A e^{\frac{j\omega\theta}{\omega_x}} [\pi \delta(\omega - \omega_x) + \pi \delta(\omega + \omega_x)] \quad (13.63)$$

Similarly,

$$V_o(j\omega) = B e^{\frac{j\omega\phi}{\omega_x}} [\pi \delta(\omega - \omega_x) + \pi \delta(\omega + \omega_x)] \quad (13.64)$$

According to Eq. (13.61)

$$H(j\omega) = \frac{V_o(j\omega)}{V_i(j\omega)} = \frac{B e^{\frac{j\omega\phi}{\omega_x}}}{A e^{\frac{j\omega\theta}{\omega_x}}} = \frac{B}{A} e^{\frac{j\omega(\phi-\theta)}{\omega_x}} \quad (13.65)$$

At steady state with  $\omega = \omega_x$ , Eq. (13.65) reduces to

$$H(j\omega_x) = \frac{B}{A} e^{j(\phi-\theta)} \quad (13.66)$$

Each of these quantities in Eq. (13.66) is known (i.e.,  $B$ ,  $A$ ,  $\phi$ , and  $\theta$ ), so the magnitude and phase angle of the transfer function are also known. Thus,  $\omega_x$  can be varied over the frequency range of interest to determine the transfer function.

In general, a transfer function,  $G(s)|_{s=j\omega} = G(j\omega)$ , is composed of the following terms:

1. Constant term  $K$
2.  $M$  poles or zeros at the origin of the form  $(j\omega)^M$
3.  $P$  poles of the form  $\prod_{p=1}^P (1 + j\omega \tau_p)$  or  $Z$  zeros of the form  $\prod_{z=1}^Z (1 + j\omega \tau_z)$ . Naturally, the poles or zeros are located at  $-\frac{1}{\tau}$ .
4.  $R$  complex poles of the form  $\prod_{r=1}^R \left(1 + \left(\frac{2\zeta_r}{\omega_{nr}}\right)j\omega + \left(\frac{j\omega}{\omega_{nr}}\right)^2\right)$  or  $S$  zeros of the form  $\prod_{s=1}^S \left(1 + \left(\frac{2\zeta_s}{\omega_{ns}}\right)j\omega + \left(\frac{j\omega}{\omega_{ns}}\right)^2\right)$
5. Pure time delay  $e^{-j\omega T_d}$

where  $M$ ,  $P$ ,  $Z$ ,  $R$ ,  $S$ , and  $T_d$  are all positive integers. Incorporating the preceding terms, the transfer function is written as

$$G(j\omega) = \frac{K \times e^{-j\omega T_d} \times \left( \prod_{z=1}^Z (1 + j\omega\tau_z) \right) \times \left( \prod_{s=1}^S \left( 1 + \left( \frac{2\zeta_s}{\omega_{n_s}} \right) j\omega + \left( \frac{j\omega}{\omega_{n_s}} \right)^2 \right) \right)}{(j\omega)^M \times \left( \prod_{p=1}^P (1 + j\omega\tau_p) \right) \times \left( \prod_{r=1}^R \left( 1 + \left( \frac{2\zeta_r}{\omega_{n_r}} \right) j\omega + \left( \frac{j\omega}{\omega_{n_r}} \right)^2 \right) \right)} \quad (13.67)$$

This equation is used as a template when describing the data with a model. To determine the value of the unknown parameters in the model, the logarithm and asymptotic approximations to the transfer function are used. In general, the logarithmic gain, in dB, of the transfer function template is

$$\begin{aligned} 20 \log|G(j\omega)| &= 20 \log K + 20 \sum_{z=1}^Z \log|1 + j\omega\tau_z| + 20 \sum_{s=1}^S \log \left| 1 + \left( \frac{2\zeta_s}{\omega_{n_s}} \right) j\omega + \left( \frac{j\omega}{\omega_{n_s}} \right)^2 \right| \\ &\quad - 20 \log|(j\omega)^M| - 20 \sum_{p=1}^P \log|1 + j\omega\tau_p| - 20 \sum_{r=1}^R \log \left| 1 + \left( \frac{2\zeta_r}{\omega_{n_r}} \right) j\omega + \left( \frac{j\omega}{\omega_{n_r}} \right)^2 \right| \end{aligned} \quad (13.68)$$

and the phase, in degrees, is

$$\begin{aligned} \phi(\omega) &= -\omega T_d + \sum_{z=1}^Z \tan^{-1}(\omega\tau_z) + \sum_{s=1}^S \tan^{-1} \left( \frac{2\zeta_s \omega_{n_s} \omega}{\omega_{n_s}^2 - \omega^2} \right) - M \times (90^\circ) \\ &\quad - \sum_{p=1}^P \tan^{-1}(\omega\tau_p) - \sum_{r=1}^R \tan^{-1} \left( \frac{2\zeta_r \omega_{n_r} \omega}{\omega_{n_r}^2 - \omega^2} \right) \end{aligned} \quad (13.69)$$

where the phase angle of the constant is  $0^\circ$  and the magnitude of the time delay is 1. Evident from these expressions is that each term can be considered separately and added together to obtain the complete Bode diagram. The asymptotic approximations to the logarithmic gain for the poles and zeros are given by the following:

- **Poles at the origin**

*Gain:*  $-20 \log|(j\omega)| = -20 \log \omega$ . The logarithmic gain at  $\omega = 1$  is 0 (i.e., the line passes through 0 dB at  $\omega = 1$  radian/s).

*Phase:*  $\phi = -90^\circ$ . If there is more than one pole, the slope of the gain changes by  $M \times (-20)$  and the phase by  $M \times (-90^\circ)$ .

- **Pole on the real axis**

$$\text{Gain: } -20 \log|1 + j\omega\tau_p| = \begin{cases} 0 & \text{for } \omega < \frac{1}{\tau_p} \\ -20 \log(\omega\tau_p) & \text{for } \omega \geq \frac{1}{\tau_p} \end{cases}$$

*Phase:* an asymptotic approximation to  $-\tan^{-1}(\omega\tau_p)$  is drawn with a straight line from  $0^\circ$  at one decade below  $\omega = \frac{1}{\tau_p}$  to  $-90^\circ$  at 1 decade above  $\omega = \frac{1}{\tau_p}$ .

The pole is located at  $-\frac{1}{\tau_p}$ .

- **Zero on the real axis**

$$\text{Gain: } 20 \log|1 + j\omega\tau_z| = \begin{cases} 0 & \text{for } \omega < \frac{1}{\tau_z} \\ 20 \log(\omega\tau_z) & \text{for } \omega \geq \frac{1}{\tau_z} \end{cases}$$

*Phase:* an asymptotic approximation to  $\tan^{-1}(\omega\tau_z)$  is drawn with a straight line from  $0^\circ$  at one decade below  $\omega = \frac{1}{\tau_z}$  to  $+90^\circ$  at 1 decade above  $\omega = \frac{1}{\tau_z}$ .

The zero is located at  $-\frac{1}{\tau_z}$ .

- **Complex poles**

$$\text{Gain: } -20 \log \left| 1 + \left( \frac{2\zeta_r}{\omega_{n_r}} \right) j\omega + \left( \frac{j\omega}{\omega_{n_r}} \right)^2 \right| = \begin{cases} 0 & \text{for } \omega < \omega_{n_r} \\ -40 \log \left( \frac{\omega}{\omega_{n_r}} \right) & \text{for } \omega \geq \omega_{n_r} \end{cases}$$

A graph of the actual magnitude-frequency is shown in [Figure 13.61](#), with  $\omega_n = 1.0$  and  $\zeta$  ranging from 0.05 to 1.0. Notice that as  $\zeta$  decreases from 1.0, the magnitude peaks at correspondingly larger values. As  $\zeta$  approaches zero, the magnitude approaches infinity at  $\omega = \omega_{n_r}$ . For values of  $\zeta > 0.707$  there is no resonance.

*Phase:* depending on the value of  $\zeta_r$ , the shape of the curve is quite variable but in general is  $0^\circ$  at one decade below  $\omega = \omega_{n_r}$  and  $-180^\circ$  at 1 decade above  $\omega = \omega_{n_r}$ .

A graph of the actual phase-frequency is shown in [Figure 13.61](#) with  $\omega_n = 1.0$  and  $\zeta$  ranging from 0.05 to 1.0. Notice that as  $\zeta$  decreases from 1.0, the phase changes more quickly from  $0^\circ$  to  $180^\circ$  over a smaller frequency interval.

The poles are located at  $-\zeta_r\omega_{n_r} \pm j\omega_{n_r}\sqrt{1 - \zeta_r^2}$ .

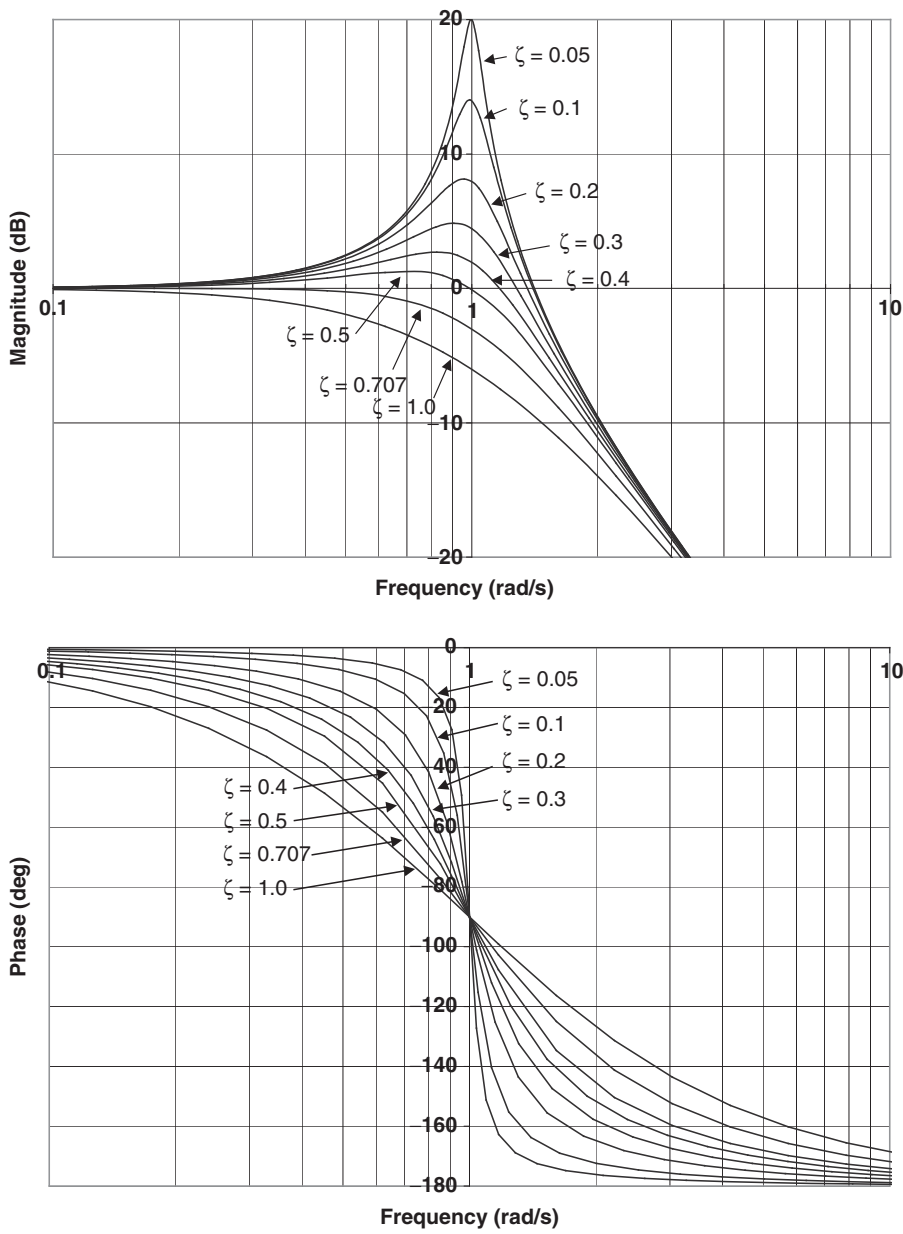
- **Complex zeros**

$$\text{Gain: } 20 \log \left| 1 + \left( \frac{2\zeta_s}{\omega_{n_s}} \right) j\omega + \left( \frac{j\omega}{\omega_{n_s}} \right)^2 \right| = \begin{cases} 0 & \text{for } \omega < \omega_{n_s} \\ 40 \log \left( \frac{\omega}{\omega_{n_s}} \right) & \text{for } \omega \geq \omega_{n_s} \end{cases}$$

*Phase:* depending on the value of  $\zeta_s$ , the shape of the curve is quite variable but in general is  $0^\circ$  at one decade below  $\omega = \omega_{n_s}$  and  $+180^\circ$  at 1 decade above  $\omega = \omega_{n_s}$ .

Both the magnitude and phase follow the two previous graphs and discussion with regard to the complex poles with the exception that the slope is +40 dB/decade rather than -40 dB/decade.

The zeros are located at  $-\zeta_s\omega_{n_s} \pm j\omega_{n_s}\sqrt{1 - \zeta_s^2}$ .

FIGURE 13.61 Bode plot of complex poles with  $\omega_n = 1.0$  rad/s.

- **Time delay**

*Gain:* 1 for all  $\omega$

*Phase:*  $-\omega T_d$

- **Constant K**

*Gain:*  $20 \log K$

*Phase:* 0

The frequency at which the slope changes in a Bode magnitude-frequency plot is called a break or corner frequency. The first step in estimating the parameters of a model involves identifying the break frequencies in the magnitude-frequency and/or phase-frequency responses. This simply involves identifying points at which the magnitude changes slope in the Bode plot. Poles or zeros at the origin have a constant slope of  $-20$  or  $+20$  dB/decade, respectively, from  $-\infty$  to  $\infty$ . Real poles or zeros have a change in slope at the break frequency of  $-20$  or  $+20$  dB/decade, respectively. The value of the pole or zero is the break frequency. Estimating complex poles or zeros is much more difficult. The first step is to locate the break frequency  $\omega_n$ , the point at which the slope changes by  $40$  dB/decade. To estimate  $\zeta$ , use the actual magnitude-frequency (size of the peak) and phase-frequency (quickness of changing  $180^\circ$ ) curves in [Figure 13.61](#) to closely match the data.

The error between the actual logarithmic gain and straight-line asymptotes at the break frequency is  $3$ dB for a pole on the real axis (the exact curve equals the asymptote  $-3$ dB). The error drops to  $0.3$ dB one decade below and above the break frequency. The error between the real zero and the asymptote is similar except the exact curve equals the asymptote  $+3$ dB. At the break frequency for the complex poles or zeros, the error between the actual logarithmic gain and straight-line asymptotes depends on  $\zeta$  and can be quite large as observed from [Figure 13.61](#).

### EXAMPLE PROBLEM 13.9

Sinusoids of varying frequencies were applied to an open-loop system, and the results in [Table 13.3](#) were measured. Construct a Bode diagram and estimate the transfer function.

TABLE 13.3 Data for [Example Problem 14.9](#)

| Frequency<br>(radians/s) | 0.01 | 0.02 | 0.05 | 0.11 | 0.24 | 0.53 | 1.17 | 2.6  | 5.7  | 12.7 | 28.1 | 62   | 137  | 304  | 453  | 672  | 1000 |
|--------------------------|------|------|------|------|------|------|------|------|------|------|------|------|------|------|------|------|------|
| 20 log G <br>(dB)        | 58   | 51   | 44   | 37   | 30   | 23   | 15   | 6    | -7   | -20  | -34  | -48  | -61  | -75  | -82  | -89  | -96  |
| Phase<br>(degrees)       | -90  | -91  | -91  | -93  | -97  | -105 | -120 | -142 | -161 | -171 | -176 | -178 | -179 | -180 | -180 | -180 | -180 |

### Solution

Bode plots of gain and phase versus frequency for the data given are shown in [Figure 13.62](#). From the phase-frequency graph, it is clear that this system has two more poles than zeros because the phase angle approaches  $-180^\circ$  as  $\omega \rightarrow \infty$ . Also note that there is no peaking observed in the gain-frequency graph or sharp changes in the phase-frequency graph, so there does not appear to be any lightly damped ( $\zeta < 0.5$ ) complex poles. However, this does not imply that there are no heavily damped complex poles at this time.

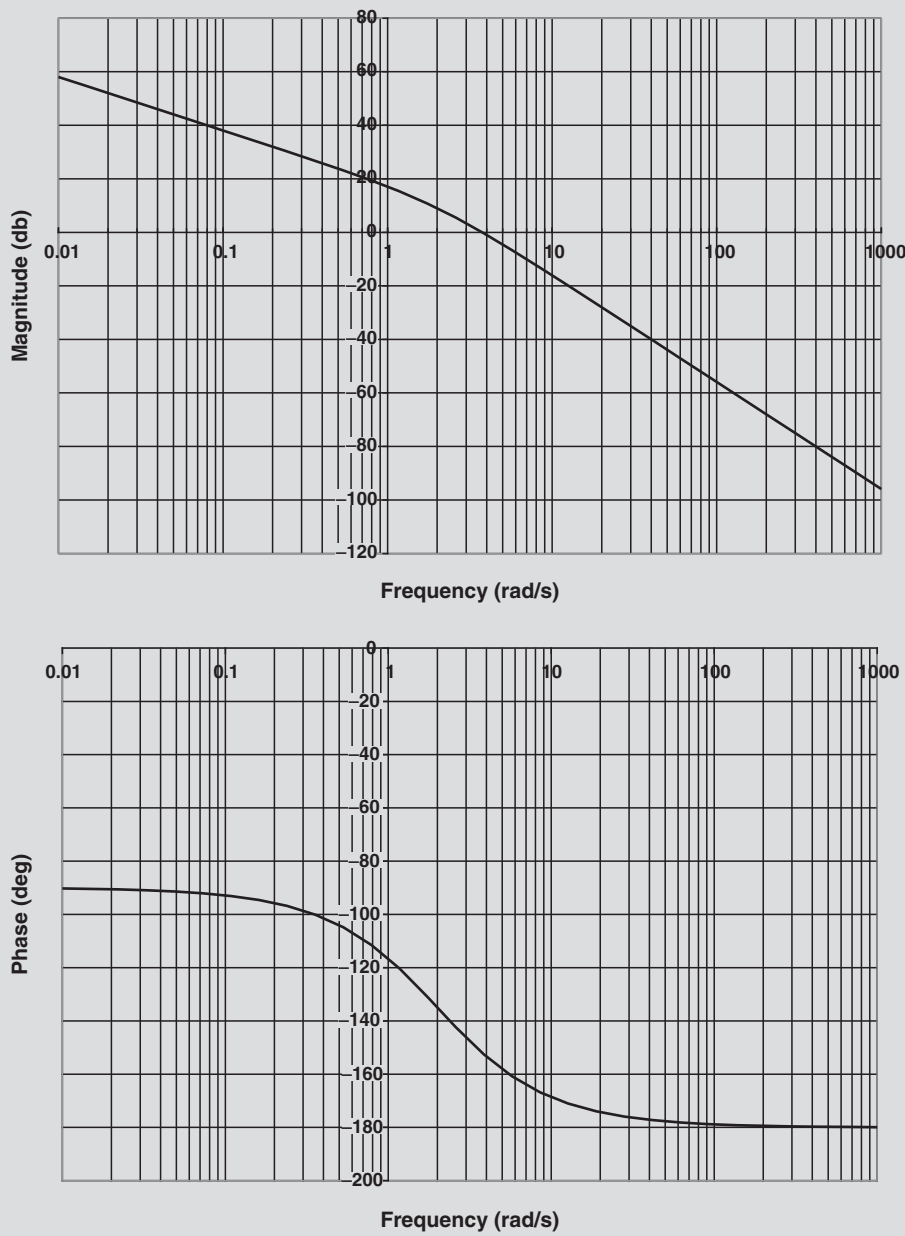


FIGURE 13.62 Data for Example Problem 13.9.

For frequencies in the range of 0.01 to 1 radians/s, the slope of the gain-frequency graph is  $-20$  dB per decade. Since it is logical to assume that the slope remains at  $-20$  dB for frequencies less than 0.01 radians/s, a transfer function with a pole at the origin provides such a response. If

*Continued*

possible, it is important to verify that the magnitude-frequency response stays at  $-20$  dB per decade for frequencies less than  $0.01$  radians/s to the limits of the recording instrumentation.

For frequencies in the range of  $2$  to  $1,000$  radians/s, the slope of the gain-frequency graph is  $-40$  dB per decade. Since a pole has already been identified in the previous frequency interval, it is reasonable to conclude that there is another pole in this interval. Other possibilities exist such as an additional pole and a zero that are closely spaced, or a complex pole and a zero. However, in the interests of simplicity and because these possibilities are not evident in the graphs, the existence of a pole is all that is required to describe the data.

Summarizing at this time, the model contains a pole at the origin and another pole somewhere in the region above  $1$  radians/s. It is also safe to conclude that the model does not contain heavily damped complex poles since the slope of the gain-frequency graph is accounted for completely.

To estimate the unknown pole, straight lines are drawn tangent to the magnitude-frequency curve as shown in Figure 13.63. The intersection of the two lines gives the break frequency for the pole at approximately  $2$  radians/s. Notice that the actual curve is approximately  $3$ dB below the asymptotes as discussed previously and observed in the following figure.

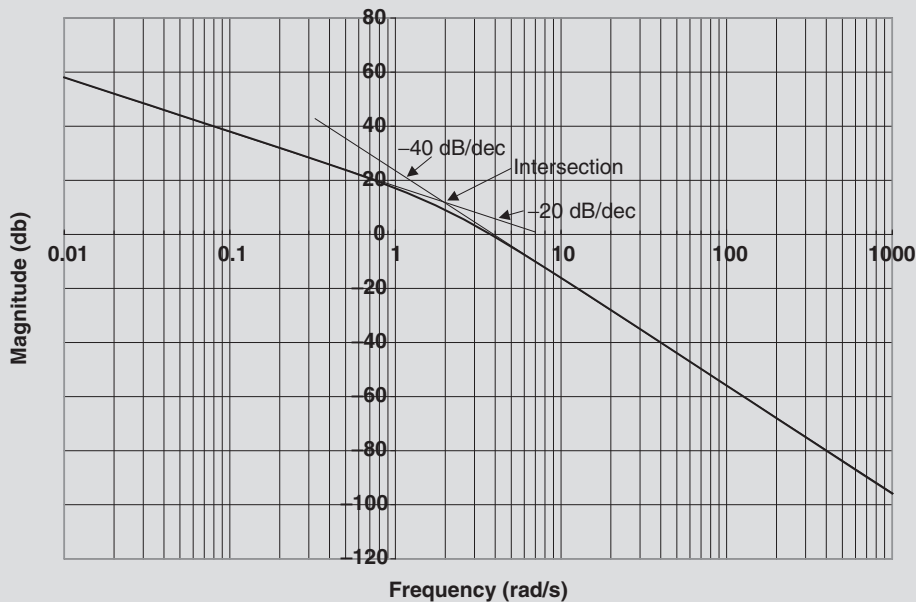


FIGURE 13.63 Straight-line approximations for Example Problem 13.9.

The model developed thus far is

$$G(j\omega) = \frac{1}{j\omega \left( \frac{j\omega}{2} + 1 \right)}$$

To determine the constant  $K$ , the magnitude at  $\omega = 1$  radian/s is investigated. The pole at zero contributes a value of 0 toward the logarithmic gain. The pole at 2 contributes a value of  $-1$  dB ( $-20 \log \left| \frac{j\omega}{2} + 1 \right| = -20 \log \left( \sqrt{\left(\frac{1}{2}\right)^2 + 1^2} \right) = -1$  dB) toward the logarithmic gain. The reason that the contribution of the pole at 2 was computed was that the point 1 radian/s was within the range of  $\pm$  a decade of the break frequency. At  $\omega = 1$  radian/s, the nonzero terms are

$$20 \log |G(\omega)| = 20 \log K - 20 \log \left| \frac{j\omega}{2} + 1 \right|$$

From the gain-frequency graph,  $20 \log |G(\omega)| = 17$  dB. Therefore,

$$17 = 20 \log K - 1$$

or  $K = 8$ . The model now consists of

$$G(j\omega) = \frac{8}{j\omega \left( \frac{j\omega}{2} + 1 \right)}$$

The last term to investigate is whether there is a time delay in the system. At the break frequency  $\omega = 2.0$  radians/s, the phase angle from the current model should be

$$\phi(\omega) = -90 - \tan^{-1} \left( \frac{\omega}{2} \right) = -90 - 45 = -135^\circ$$

This value is approximately equal to the data, and thus there does not appear to be a time delay in the system.

Example Problem 13.9 illustrated a process of thinking in determining the structure and parameters of a model. Carrying out an analysis in this fashion on complex systems is extremely difficult, if not impossible. Software packages that automatically carry out estimation of poles, zeros, a time delay, and a gain of a transfer function from data are available, such as the System Identification toolbox in MATLAB. There are also other programs that provide more flexibility than MATLAB in analyzing complex systems, such as the FORTRAN program written by Seidel [43].

There are a variety of other inputs that one can use to stimulate the system to elicit a response. These include such transient signals as a pulse, step, and ramp, and noise signals such as white noise and pseudo random binary sequences. The reason these other techniques might be of interest is that not all systems are excited via sinusoidal input. One such system is the fast eye movement system. Here we typically use a step input to analyze the system (see [17]).

In analyzing the output data obtained from step input excitation to determine the transfer function, we use a frequency response method using the Fourier Transform and the fast Fourier Transform. The frequency response of the input is known. The frequency response of the output is calculated via a numerical algorithm called the fast Fourier Transform (FFT). To calculate the FFT of the output, the data must first be digitized using an A/D converter and stored in disk memory. Care must be taken to antialias (low-pass) filter

any frequency content above the highest frequency of the signal, and sample at a rate of at least 2.5 times the highest frequency. The transfer function is then estimated.

### 13.10.2 Identification of a Linear First-Order System

The technique for solving for the parameters of a first-order system is presented here. Assume that the system of interest is a first-order system that is excited with a step input. The response to the input is

$$y(t) = \left( y_{ss} + K e^{\frac{-t}{\tau}} \right) u(t) \quad (13.70)$$

where  $K = -(y_{ss} - y(0))$  and is shown in [Figure 13.64](#). Note that at  $t = \tau$ , the response is 63 percent of the way from the initial to the steady-state value. Similarly, at  $t = 4\tau$ , the response is 98 percent of the way from the initial to the steady-state value.

Suppose step input data are collected from an unknown first-order system shown in [Figure 13.64](#). To fully describe the system, the parameters of [Eq. \(13.70\)](#) need to be estimated. One way to estimate the system time constant is from the initial slope of the response and a smoothed steady-state value (via averaging). That is, the time constant  $\tau$  is found from

$$\dot{y}(t) = \frac{1}{\tau} (y_{ss} - y(0)) e^{\frac{-t}{\tau}} \rightarrow \tau = \frac{y_{ss} - y(0)}{\dot{y}(t)} e^{\frac{-t}{\tau}}$$

At  $t = 0$ ,  $\tau = \frac{y_{ss} - y(0)}{\dot{y}(0)}$ , where  $\dot{y}(0)$  is the initial slope of the response. The equation for estimating  $\tau$  is nothing more than the equation of a straight line. This technique is illustrated in [Figure 13.65](#).

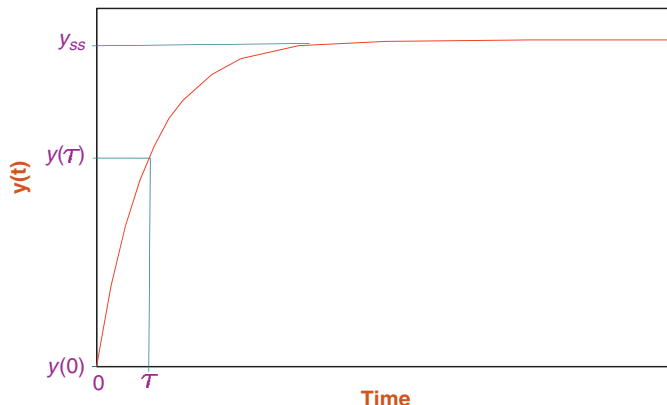


**FIGURE 13.64** First-order system response to a step input.

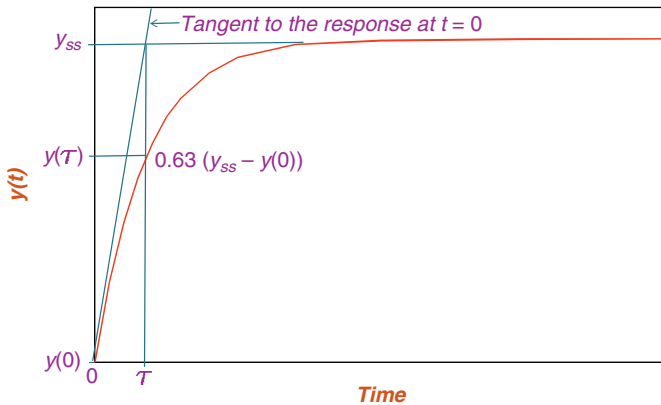


FIGURE 13.65 Estimating the time constant from the initial slope of the response.

### EXAMPLE PROBLEM 13.10

The data in Table 13.4 were collected for the step response for an unknown first-order system. Find the parameters that describe the model.

TABLE 13.4 Data for Example Problem 13.10

| $t$    | 00.0 | 00.05 | 00.1  | 00.15 | 00.2 | 0.25 | 00.3 | 00.4 | 00.5 | 00.7 | 1.0  | 1.5  | 2.0  |
|--------|------|-------|-------|-------|------|------|------|------|------|------|------|------|------|
| $y(t)$ | 00.0 | 00.56 | 00.98 | 1.30  | 1.54 | 1.73 | 1.86 | 2.04 | 2.15 | 2.24 | 2.27 | 2.28 | 2.28 |

### Solution

The model under consideration is described by Eq. (13.70),  $y(t) = y_{ss} + Ke^{\frac{-t}{\tau}} u(t)$ , with unknown parameters  $y_{ss}$ ,  $K$ , and  $\tau$ . The data are plotted in Figure 13.66, along with the tangent. Clearly  $y_{ss} = 2.28$  and  $K = -2.88$ .

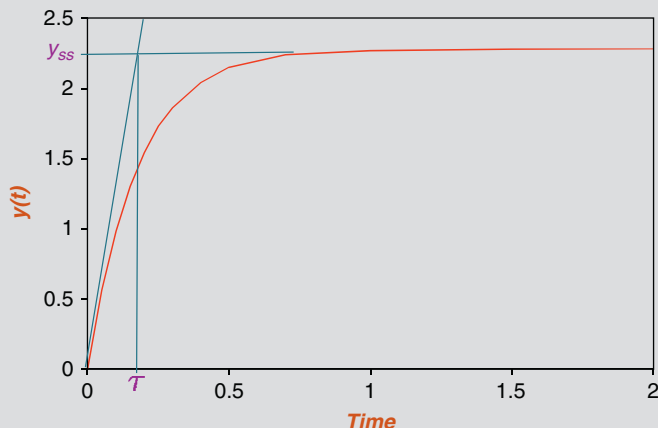


FIGURE 13.66 Illustration for Example Problem 13.10.

*Continued*

From the graph,  $\tau = 0.17$  s. Thus, we have

$$y(t) = 2.88 \left( 1 - e^{\frac{-t}{0.17}} \right) u(t).$$

### 13.10.3 Identification of a Linear Second-Order System

Consider estimating the parameters of a second-order system, such as  $M\ddot{y} + B\dot{y} + Ky = f(t)$ . It is often convenient to rewrite the original differential equation in the standard form for ease in analysis as

$$\ddot{y} + 2\zeta\omega_n\dot{y} + \omega_n^2 y = f(t) \quad (13.71)$$

where  $\omega_n$  is the undamped natural frequency and  $\zeta$  is the damping ratio. The roots of the characteristic equation are

$$s_{1,2} = -\zeta\omega_n \pm \omega_n\sqrt{\zeta^2 - 1} = -\zeta\omega_n \pm j\omega_n\sqrt{1 - \zeta^2} = -\zeta\omega_n \pm j\omega_d \quad (13.72)$$

A system with  $0 < \zeta < 1$  is called underdamped, with  $\zeta = 1$  critically damped and with  $\zeta > 1$  overdamped.

#### Step Response

The complete response of the system in Eq. (13.72) to a step input with arbitrary initial conditions is given in Table 13.5, where  $y_{ss}$  is the steady-state value of  $y(t)$ , and  $A_1$ ,  $A_2$ ,  $B_1$ ,  $\phi$ ,  $C_1$ , and  $C_2$  are the constants that describe the system evaluated from the initial conditions. For the underdamped system, one can estimate  $\zeta$  and  $\omega_n$  to a step input with magnitude  $\gamma$  from data as follows. Consider the step response in Figure 13.67. A suitable model for the system is a second-order underdamped model (i.e.,  $0 < \zeta < 1$ ), with solution

$$y(t) = C \left[ 1 + \frac{e^{-\zeta\omega_n t}}{\sqrt{1 - \zeta^2}} \cos(\omega_d t + \phi) \right] \quad (13.73)$$

where  $C$  is the steady-state response,  $y_{ss}$ , and  $\omega_d = \omega_n\sqrt{1 - \zeta^2}$  and  $\phi = \pi + \tan^{-1}\frac{-\zeta}{\sqrt{1 - \zeta^2}}$ .

The following terms illustrated in Figure 13.67 are typically used to describe, quantitatively, the response to a step input:

TABLE 13.5 Step Response for a Second-Order System

| Damping           | Natural Response Equation  |
|-------------------|--|
| Overdamped        | $y(t) = y_{ss} + A_1 e^{s_1 t} + A_2 e^{s_2 t}$                    |
| Underdamped       | $y(t) = y_{ss} + B_1 e^{-\zeta\omega_n t} \cos(\omega_d t + \phi)$ |
| Critically damped | $y(t) = y_{ss} + (C_1 + C_2 t) e^{-\zeta\omega_n t}$               |

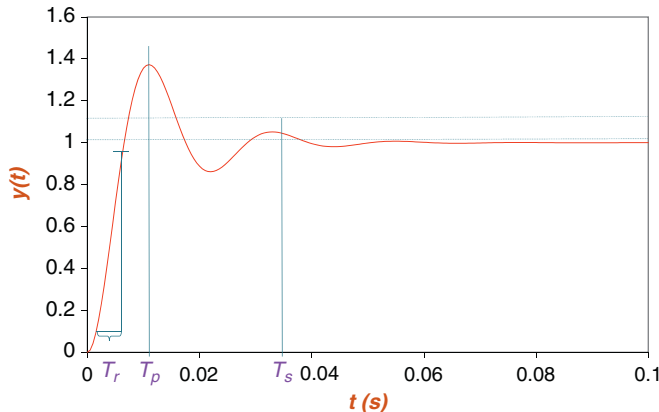


FIGURE 13.67 Sample second-order response with graphical estimates of rise time, time to peak overshoot, and settling time.

- Rise time,  $T_r$ . The time for the response to rise from 10 to 90 percent of steady state.
- Settling time,  $T_s$ . The time for the response to settle within  $\pm 5$  percent of the steady-state value.
- Peak overshoot time,  $T_p$ . The time for the response to reach the first peak overshoot.

Using values graphically determined from the data for the preceding quantities, as shown in Figure 13.67, provides estimates for the parameters of the model. The time to peak overshoot,  $T_p$ , is found by first calculating

$$\frac{\partial y}{\partial t} = \frac{\gamma e^{-\zeta\omega_n t}}{K\sqrt{1-\zeta^2}} [-\zeta\omega_n \cos(\omega_d t + \phi) - \omega_d \sin(\omega_d t + \phi)] \quad (13.74)$$

using the chain rule on Eq. (13.74) and then determining  $T_p$  from  $\frac{\partial y}{\partial t}|_{t=T_p} = 0$ , yielding

$$T_p = \frac{\pi}{\omega_n \sqrt{1-\zeta^2}} \quad (13.75)$$

The response at  $T_p$  is

$$y(T_p) = C \left( 1 + e^{-\zeta \frac{\pi}{\sqrt{1-\zeta^2}}} \right) \quad (13.76)$$

and is found as follows

$$y(T_p) = C \left[ 1 + \frac{e^{-\zeta\omega_n \frac{\pi}{\omega_n \sqrt{1-\zeta^2}}}}{\sqrt{1-\zeta^2}} \cos \left( \omega_d \frac{\pi}{\omega_n \sqrt{1-\zeta^2}} + \phi \right) \right]$$

$$\begin{aligned}
&= C \left[ 1 + \frac{e^{-\zeta \omega_n} \frac{\pi}{\omega_n \sqrt{1-\zeta^2}}}{\sqrt{1-\zeta^2}} \cos(\pi + \phi) \right] \\
&= C \left[ 1 + \frac{e^{-\zeta \omega_n} \frac{\pi}{\omega_n \sqrt{1-\zeta^2}}}{\sqrt{1-\zeta^2}} \sqrt{1-\zeta^2} \right] \\
&= C \left( 1 + e^{-\zeta \frac{\pi}{\sqrt{1-\zeta^2}}} \right)
\end{aligned}$$

With the performance estimates calculated from the data and Eqs. (13.75) and (13.76), it is possible to estimate  $\zeta$  and  $\omega_n$ . First, find  $\zeta$  by using the Eq. (13.76). Then, using the solution for  $\zeta$ , substitute this value into Eq. (13.75) to find  $\omega_n$ . The phase angle  $\phi$  in Eq. (13.73) is determined from the estimate for  $\zeta$ —that is,

$$\phi = \pi + \tan^{-1} \frac{-\zeta}{\sqrt{1-\zeta^2}}$$

### EXAMPLE PROBLEM 13.11

Find  $\zeta$  and  $\omega_n$  for the data in Figure 13.67.

#### Solution

From the data in Figure 13.67,  $C = 1.0$ ,  $T_p = 0.011$ , and  $y(T_p) = 1.37$ . Therefore,

$$y(T_p) = C \left( 1 + e^{-\zeta \frac{\pi}{\sqrt{1-\zeta^2}}} \right) \quad \rightarrow \quad \zeta = \sqrt{\frac{\left( \ln(y(T_p)-1) \right)^2}{1 + \frac{\left( \ln(y(T_p)-1) \right)^2}{\pi^2}}} = 0.3$$

$$T_p = \frac{\pi}{\omega_n \sqrt{1-\zeta^2}} \quad \rightarrow \quad \omega_n = \frac{\pi}{T_p \sqrt{1-\zeta^2}} = 300 \text{ radians/s}$$

and

$$\phi = \pi + \tan^{-1} \frac{-\zeta}{\sqrt{1-\zeta^2}} = 2.8369 \text{ radians.}$$

### Impulse Response

The complete response of the system,  $a_2 \ddot{y} + a_1 \dot{y} + a_0 y = \delta(t)$ , to an impulse with zero initial conditions is given in [Table 13.6](#). Let us consider estimating  $\zeta$  and  $\omega_n$  for the over-damped case. Here, the solution is

$$y(t) = \frac{1}{2\omega_n \sqrt{\zeta^2 - 1}} (e^{s_1 t} - e^{s_2 t}) \quad (13.77)$$

where  $s_{1,2} = -\zeta\omega_n \pm \omega_n \sqrt{\zeta^2 - 1}$ . As before, we use the time to peak overshoot,  $T_p$ , to find the parameter values. The time to peak overshoot is found by first calculating

$$\frac{\partial y}{\partial t} = \frac{1}{2\omega_n \sqrt{\zeta^2 - 1}} (s_1 e^{s_1 t} - s_2 e^{s_2 t}) \quad (13.78)$$

and then determining  $T_p$  from  $\frac{\partial y}{\partial t}|_{t=T_p} = 0$ . This gives

$$T_p = \frac{\ln\left(\frac{s_2}{s_1}\right)}{s_1 - s_2} \quad (13.79)$$

In this situation, the time to peak overshoot is easy to estimate from the data.

If one of the time constants is considerably larger than the other, then the larger or dominant time constant can be determined from the data by locating when the response is less than 1 percent of the initial value. For example, consider the impulse response  $y(t) = e^{-t} - e^{-4t}$  as shown in [Figure 13.68](#). The response of the smaller time constant ( $-e^{-4t}$ ) goes to zero by approximately 1 s, well before the response of the dominant time constant ( $-e^{-t}$ ). So the impulse response is essentially equal to the response of the dominant time constant ( $-e^{-t}$ ) for  $t > 1$  s. To determine the dominant time constant, locate the time at which the response for the dominant time is at 1 percent of the value at  $t = 0$  s; that time is  $5\tau$ . To estimate the initial value of the response for the dominant time constant at  $t = 0$ , project the exponential back, as shown in [Figure 13.68](#), to give a value of 1, then take 1 percent of that value to find  $5\tau$ . The dominant time constant is then easily determined. Thus, given  $T_p$  and one of the time constants, the smaller time constant can then be determined from [Eq. 13.79](#) and using MATLAB's "solve" command, from which  $\zeta$  and  $\omega_n$  are calculated (i.e.,  $\omega_n^2 = s_1 s_2$  and  $\zeta = \frac{s_1 + s_2}{2\omega_n}$ ).

**TABLE 13.6** Impulse Response for a Second-Order System

| Damping           | Natural Response Equation   |
|-------------------|---|
| Overdamped        | $y(t) = \frac{1}{2\omega_n \sqrt{\zeta^2 - 1}} (e^{s_1 t} - e^{s_2 t})$             |
| Underdamped       | $y(t) = \frac{\omega_n e^{-\omega_n \zeta t}}{\sqrt{1 - \zeta^2}} \sin(\omega_d t)$ |
| Critically damped | $y(t) = te^{-\omega_n t}$   |

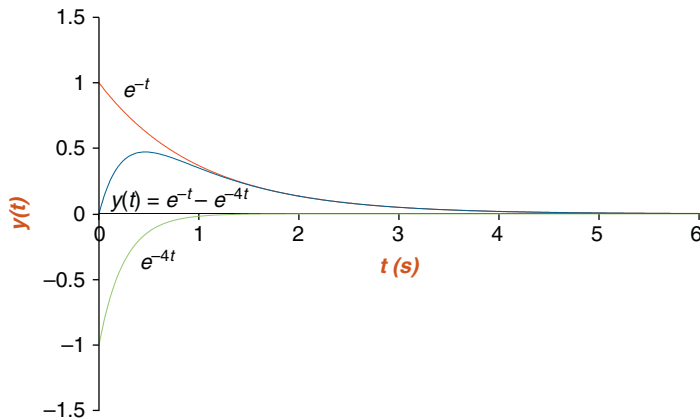


FIGURE 13.68 Impulse response  $y(t) = e^{-t} - e^{-4t}$ , with functions  $e^{-t}$  and  $e^{-4t}$  also shown.

### EXAMPLE PROBLEM 13.12

Find  $\zeta$  and  $\omega_n$  for the impulse response shown in Figure 13.69.

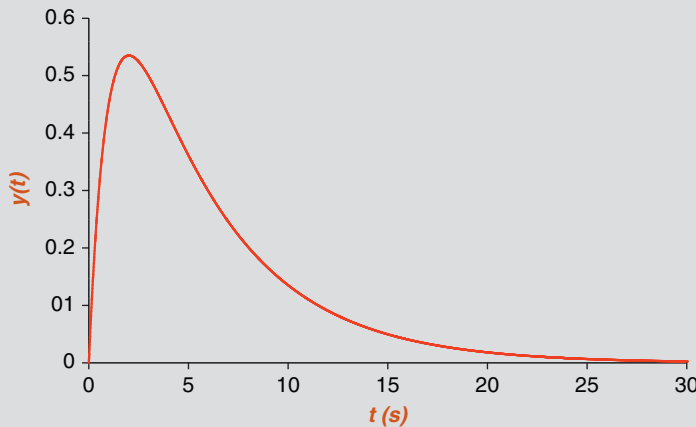


FIGURE 13.69 Illustration for Example Problem 13.12.

#### Solution

The data (solid line) is redrawn in Figure 13.70 with the exponential of the dominant time constant extrapolated back to zero (dotted line). This gives an initial value of 1 for the exponential. The response falls to 1 percent of 1 at approximately 25 s, giving  $5\tau_2 \approx 25$ , or  $\tau_2 = 5$  s for the dominant time constant and  $s_2 = -0.2$ .

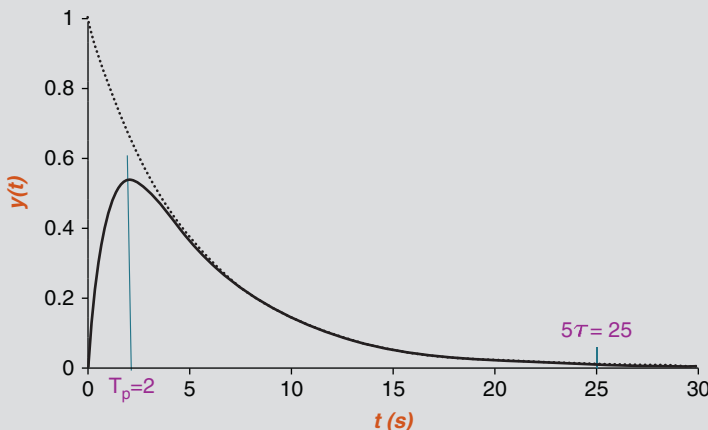


FIGURE 13.70 Graphical analysis for Example Problem 13.12.

From Figure 13.70, the time to peak overshoot occurs at approximately 2 s. Using Eq. (13.79), we have

$$s_1 T_p + \ln(s_1) = s_2 T_p + \ln(s_2)$$

and MATLAB's "solve" command gives  $s_1$ .

```
>> solve('s1*2+log(s1)=s2*2+log(s2)', 's2=-.2')
ans =
s1: [2x1 sym]
s2: [2x1 sym]
>> s1
s1 =
-1.0093940626323415922798829136295
-0.2
```

Notice that there are two roots for  $s_1$ , since both are solutions to the equation. Since  $s_2 = -0.2$ , then  $s_1 = -1$ . Finally, we have

$$\omega_n^2 = s_1 s_2 = 0.2 \text{ and } \zeta = \frac{s_1 + s_2}{2\omega_n} = 3.$$

### 13.11 EXERCISES

- Consider the system shown in Figure 13.71 defined with  $M_1 = 1$  kg,  $M_2 = 2$  kg,  $B_1 = 0.5$  N·s/m,  $B_2 = 1$  N·s/m,  $K_1 = 3$  N/m, and  $K_2 = 2$  N/m. Let  $f(t)$  be the applied force, and  $x_1$  and  $x_2$  be the displacements from rest. (a) Find the transfer function. (b) Solve for  $x_1(t)$  if  $f(t) = 3u(t)$  N and zero initial conditions. (c) Simulate the solution with SIMULINK if  $f(t) = 3u(t)$  N and zero initial conditions. (d) Use MATLAB to draw the Bode diagram.

*Continued*

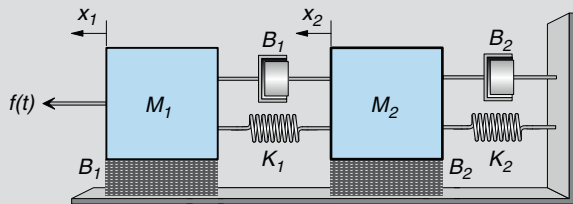


FIGURE 13.71 Illustration for Exercise 1.

2. Consider the system shown in Figure 13.72 defined with  $M_1 = 2 \text{ kg}$ ,  $B_1 = 1 \text{ N}\cdot\text{s}/\text{m}$ ,  $B_2 = 2 \text{ N}\cdot\text{s}/\text{m}$ ,  $K_1 = 5 \text{ N/m}$ , and  $K_2 = 2 \text{ N/m}$ . Let  $f(t)$  be the applied force, and  $x_1$  and  $x_2$  be the displacements from rest. (a) Find the transfer function. (b) Solve for  $x_2(t)$  if  $f(t) = u(t) \text{ N}$  and zero initial conditions. (c) Simulate the solution with SIMULINK if  $f(t) = u(t) \text{ N}$  and zero initial conditions. (c) Use MATLAB to draw the Bode diagram.

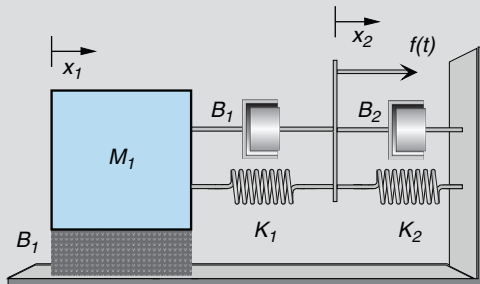


FIGURE 13.72 Illustration for Exercise 2.

3. Consider the system illustrated in Figure 13.73 defined with  $M_1 = 3 \text{ kg}$ ,  $M_2 = 1 \text{ kg}$ ,  $B_1 = 1 \text{ N}\cdot\text{s}/\text{m}$ ,  $B_2 = 2 \text{ N}\cdot\text{s}/\text{m}$ ,  $K_1 = 1 \text{ N/m}$ , and  $K_2 = 1 \text{ N/m}$ . Let  $f(t)$  be the applied force, and  $x_1$  and  $x_2$  be

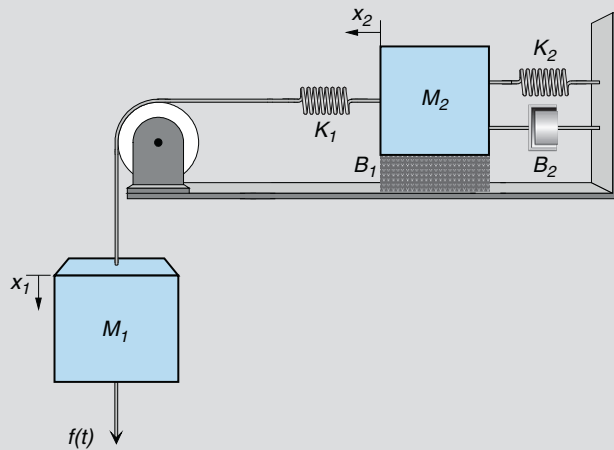


FIGURE 13.73 Illustration for Exercise 3.

the displacements from rest. The pulley is assumed to have no inertia or friction. (a) Write the differential equations that describe this system. (b) Solve for  $x_2(t)$  if  $f(t) = 10u(t)$  N and zero initial conditions. (c) If the input is a step with magnitude 10 N and zero initial conditions, simulate the solution with SIMULINK.

4. Consider the system in Figure 13.74, where there are two viscous elements  $B_2$ ,  $K_1$  is a translational element, and  $K_2$  is a rotational element. Let  $\tau(t)$  be the applied torque,  $x_1$  the displacement of  $M$  from rest, and  $\theta$  the angular displacement of the element  $J$  from rest (i.e., when the springs are neither stretched nor compressed). The pulley has no inertia or friction, and the cable does not stretch. (a) Write the differential equations that describe the system. (b) Write the state variable equations that describe the system. (c) If the input is a step with magnitude 3 N and zero initial conditions, simulate the solution with SIMULINK.

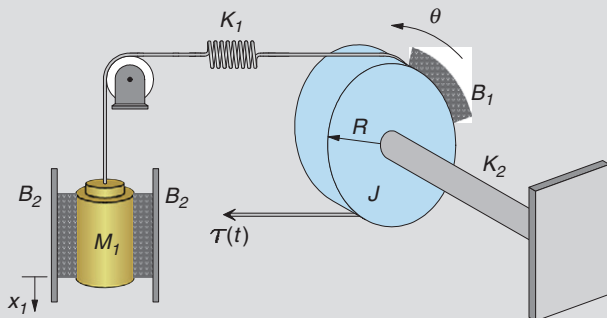


FIGURE 13.74 Illustration for Exercise 4.

5. Consider the system in Figure 13.75, where there are two viscous elements  $B_2$ ,  $K_1$  is a translational element, and  $K_2$  is a rotational element. Let  $f(t)$  be the applied force,  $x_1$  the displacement of  $M_1$  and  $x_2$  the displacement of  $M_2$  from rest, and  $\theta$  the angular displacement of the element  $J$  from rest (i.e., when the springs are neither stretched nor compressed). The pulley has no inertia or friction, and the cable does not stretch. (a) Write the differential equations that describe the system. (b) Write the state variable equations that describe the system.

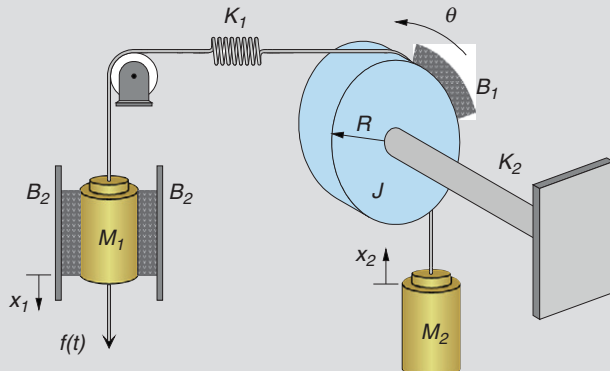


FIGURE 13.75 Illustration for Exercise 5.

*Continued*

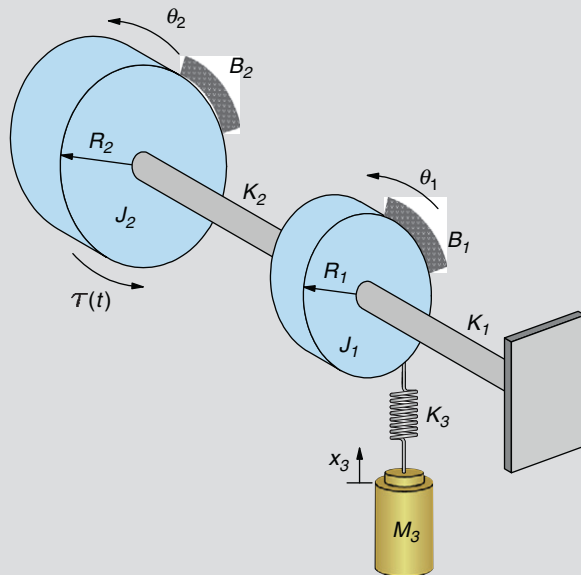


FIGURE 13.76 Illustration for Exercise 6.

6. Consider the system in the following diagram (Figure 13.76) defined with  $M_3 = 1 \text{ kg}$ ,  $K_3 = 4 \text{ N/m}$  (translational),  $J_1 = 0.5 \text{ kg-m}^2$ ,  $B_1 = 1 \text{ N-s-m}$ ,  $B_2 = 2 \text{ N-s-m}$ ,  $K_1 = 2 \text{ N-m}$ ,  $J_2 = 2 \text{ kg-m}^2$ ,  $K_2 = 1 \text{ N-m}$ ,  $R_1 = 0.2 \text{ m}$ , and  $R_2 = 1.0 \text{ m}$ . Let  $\tau(t)$  be the applied torque,  $x_3$  be the displacement of  $M_3$  from rest, and  $\theta_1$  and  $\theta_2$  be the angular displacement of the elements  $J_1$  and  $J_2$  from rest (i.e., when the springs are neither stretched nor compressed). (a) Write the differential equations that describe this system. (b) If the input is a step with magnitude 10 N, simulate the solution with SIMULINK.
7. What is the main sequence diagram? How do results from the Westheimer model in Section 13.3 compare with the main sequence diagram?
8. Simulate a  $20^\circ$  saccade with the Westheimer model in Section 13.3 with  $\zeta = 0.7$  and  $\omega_n = 120 \text{ radians/s}$  using SIMULINK. Assume that  $K = 1 \text{ N-m}$ . Repeat the simulation for a 5, 10, and  $15^\circ$  saccade. Compare these results with the main sequence diagram in Figure 13.6.
9. Suppose the input to the Westheimer model is a pulse-step waveform as described in Section 13.3, and  $\zeta = 0.7$ ,  $\omega_n = 120 \text{ radians/s}$ , and  $K = 1 \text{ N-m}$ . (a) Estimate the size of the step necessary to keep the eyeball at  $20^\circ$ . (b) Using SIMULINK, find the pulse magnitude that matches the main sequence diagram in Figure 13.6 necessary to drive the eyeball to  $20^\circ$ . (c) Repeat part (b) for saccades of 5, 10, and  $15^\circ$ . (d) Compare these results with those of the Westheimer model.
10. A model of the saccadic eye movement system is characterized by the following equation.

$$\tau = 1.74 \times 10^{-3} \ddot{\theta} + 0.295 \dot{\theta} + 25\theta$$

where  $\tau$  is the applied torque. Suppose  $\tau = 200u(t)$  and the initial conditions are zero. Use Laplace transforms to solve for  $\theta(t)$ . Sketch  $\theta(t)$ .

11. Given the Westheimer model described in [Section 13.3](#) with  $\zeta = \frac{1}{\sqrt{2}}$ ,  $\omega_n = 100$  radians/s, and  $K = 1$ , solve for the general response with a pulse-step input as described in [Figure 13.11](#). Examine the change in the response as the pulse magnitude is increased and the duration of the pulse,  $t_1$ , is decreased while the steady-state size of the saccade remains constant.
12. With the Westheimer model described in [Section 13.3](#), separately estimate  $\zeta$  and  $\omega_n$  for  $5^\circ$ ,  $10^\circ$ ,  $15^\circ$ , and  $20^\circ$  saccades using information in the main sequence diagram in [Figure 13.11](#). Assume that peak overshoot,  $\theta(T_p)$ , is 1 degree greater than the saccade size. Simulate the four saccades. Develop a relationship between  $\zeta$  and  $\omega_n$  as a function of saccade size that matches the main sequence diagram. With these relationships, plot  $T_p$  and peak velocity as a function of saccade size. Compare these results to the original Westheimer main sequence results and those in [Figure 13.11](#).
13. Consider an unexcited muscle model as shown in [Figure 13.27](#) with  $K_{lt} = 32 \text{ Nm}^{-1}$ ,  $K_{se} = 125 \text{ Nm}^{-1}$ , and  $B = 3.4 \text{ Nsm}^{-1}$  ( $F = 0$  for the case of an unexcited muscle). (a) Find the transfer function  $H(j\omega) = \frac{X_1}{T}$ . (b) Use MATLAB to draw the Bode diagram.
14. Consider an unexcited muscle model in [Figure 13.38](#) with  $K_{lt} = 60.7 \text{ Nm}^{-1}$ ,  $K_{se} = 125 \text{ Nm}^{-1}$ ,  $B_1 = 2 \text{ Nsm}^{-1}$ , and  $B_2 = 0.5 \text{ Nsm}^{-1}$  ( $F = 0$  for the case of an unexcited muscle). (a) Find the transfer function  $H(j\omega) = \frac{X_1}{T}$ . (b) Use MATLAB to draw the Bode diagram.
15. Consider an unexcited muscle model as shown in [Figure 13.27](#) with  $K_{lt} = 32 \text{ Nm}^{-1}$ ,  $K_{se} = 125 \text{ Nm}^{-1}$ , and  $B = 3.4 \text{ Nsm}^{-1}$  ( $F = 0$  for the case of an unexcited muscle). If the muscle is linearly stretched from 3 mm to 6 mm over a time interval of 0.003 s, that is,  $x_1(t) = tu(t) - (t - 0.003)u(t - 0.003) + 0.003$ , then find the tension  $T$ .
16. Consider an unexcited muscle model in [Figure 13.38](#) with  $K_{lt} = 60.7 \text{ Nm}^{-1}$ ,  $K_{se} = 125 \text{ Nm}^{-1}$ ,  $B_1 = 2 \text{ Nsm}^{-1}$ , and  $B_2 = 0.5 \text{ Nsm}^{-1}$  ( $F = 0$  for the case of an unexcited muscle). If the muscle is linearly stretched from 3 mm to 6 mm over a time interval of 0.003 s—that is,  $x_1(t) = tu(t) - (t - 0.003)u(t - 0.003) + 0.003$ , then find the tension  $T$ .
17. From the horizontal eye movement model in [Figure 13.30](#), derive [Eq. \(13.35\)](#).
18. From the horizontal eye movement model in [Figure 13.41](#), derive [Eq. \(13.48\)](#).
19. From the horizontal eye movement model in [Figure 13.46](#), derive [Eq. \(13.51\)](#).
20. Using the linear homeomorphic saccadic eye movement model from [Section 13.6](#), simulate the following saccades using SIMULINK: (a)  $5^\circ$ , (b)  $10^\circ$ , (c)  $15^\circ$ , (d)  $20^\circ$ .
21. Using the linear homeomorphic saccadic eye movement model from [Section 13.7](#), simulate the following saccades using SIMULINK: (a)  $5^\circ$ , (b)  $10^\circ$ , (c)  $15^\circ$ , (d)  $20^\circ$ .
22. Using the linear homeomorphic saccadic eye movement model from [Section 13.8](#), simulate the following saccades using SIMULINK: (a)  $5^\circ$ , (b)  $10^\circ$ , (c)  $15^\circ$ , (d)  $20^\circ$ .
23. Consider the linear homeomorphic saccadic eye movement model given in [Eq. \(13.35\)](#). (a) Find the transfer function. (b) Use MATLAB to draw the Bode diagram.
24. Consider the linear homeomorphic saccadic eye movement model given in [Eq. \(13.48\)](#). (a) Find the transfer function. (b) Use MATLAB to draw the Bode diagram.
25. Consider the linear homeomorphic saccadic eye movement model given in [Eq. \(13.51\)](#). (a) Find the transfer function. (b) Use MATLAB to draw the Bode diagram.
26. Verify the length-tension curves in [Figure 13.39](#).

*Continued*

27. Verify the force-velocity curve in [Figure 13.40](#) for the muscle model in [Figure 13.38](#). (Hint: Use SIMULINK to calculate peak velocity for each value of  $M$ .)
28. Find the force-velocity curve for the experiment in which a lever is not used for the muscle model in [Figure 13.77](#). Compare the results with those in [Figure 13.40](#).

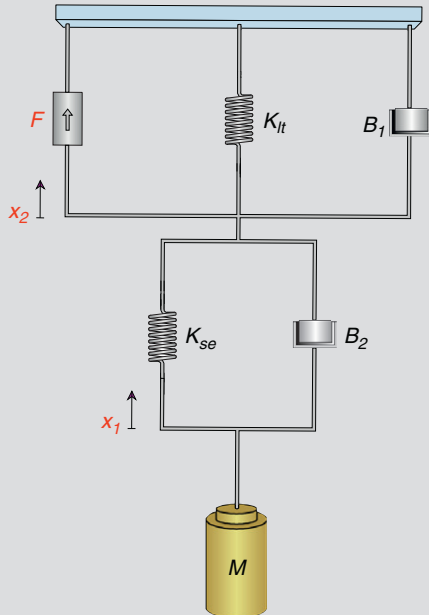


**FIGURE 13.77** Illustration for Exercise 28.

29. Consider the model in [Figure 13.78A](#) of the passive orbital tissues driven by torque,  $\tau(t)$ , with  $K_p = 0.5 \text{ g/}^\circ$ ,  $B_p = 0.06 \text{ gs/}^\circ$ , and  $J_p = 4.3 \times 10^{-5} \text{ g}^2/^\circ$ . All elements are rotational. (a) Find the transfer function  $\frac{\theta(s)}{\tau(s)}$ . (b) Use MATLAB to draw the Bode diagram.
30. Consider the model in [Figure 13.78B](#) of the passive orbital tissues driven by torque  $\tau$  with  $J_p = 4.308 \times 10^{-5} \text{ gs}^2/^\circ$ ,  $K_{p1} = 0.5267 \text{ g/}^\circ$ ,  $K_{p2} = 0.8133 \text{ g/}^\circ$ ,  $B_{p1} = 0.010534 \text{ gs/}^\circ$ , and  $B_{p2} = 0.8133 \text{ gs/}^\circ$ . All elements are rotational. (a) Find the transfer function  $H(s) = \frac{\theta(s)}{\tau(s)}$ . (b) Use MATLAB to draw the Bode diagram.
31. Consider the model in [Figure 13.79](#) of the eye movement system. The elements are all rotational and  $f_K(\theta) = K_1\theta^2$  (a nonlinear rotational spring). (a) Write the nonlinear differential equation that describes this system. (b) Write a linearized differential equation using a Taylor Series first-order approximation about an operating point.
32. Suppose the passive elasticity of unexcited muscle is given by the following nonlinear translational force-displacement relationship  $f_K(\theta) = x|x|$ , where  $x$  is the displacement from equilibrium position. Determine a linear approximation for this nonlinear element in the vicinity of the equilibrium point.

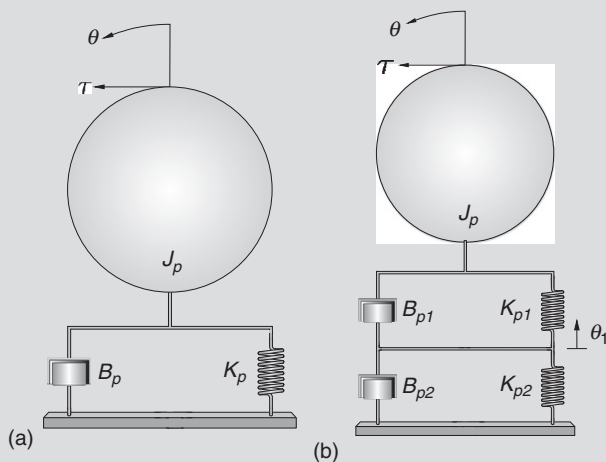


FIGURE 13.78 Illustrations for Exercises 29 and 30.

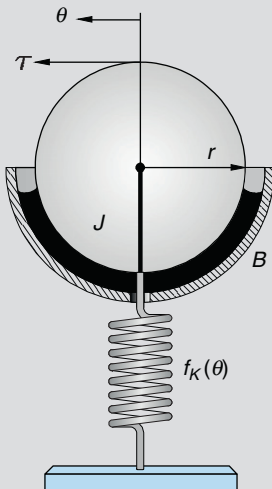


FIGURE 13.79 Illustration for Exercise 31.

33. Sinusoids of varying frequencies were applied to an open-loop system and the following results were measured. Construct a Bode diagram and estimate the transfer function.

|                           |      |      |       |       |       |       |       |       |        |        |        |        |
|---------------------------|------|------|-------|-------|-------|-------|-------|-------|--------|--------|--------|--------|
| Frequency<br>(radians/s)  | 0.6  | 1.6  | 2.6   | 3.6   | 5.5   | 6.1   | 7.3   | 9.8   | 12.7   | 32.9   | 62.1   | 100    |
| Magnitude<br>Ratio, $ G $ | 2.01 | 2.03 | 2.09  | 2.17  | 2.37  | 2.43  | 2.49  | 2.16  | 1.39   | 0.18   | 0.05   | 0.018  |
| Phase<br>(degrees)        | -3.3 | -8.9 | -15.0 | -21.8 | -38.1 | -44.8 | -60.0 | -93.6 | -123.2 | -164.2 | -170.0 | -175.0 |

34. Sinusoids of varying frequencies were applied to an open-loop system and the following results were measured. Construct a Bode diagram and estimate the transfer function.

*Continued*

|                       |       |       |      |      |       |        |        |        |        |        |        |         |
|-----------------------|-------|-------|------|------|-------|--------|--------|--------|--------|--------|--------|---------|
| Frequency (radians/s) | .001  | .356  | 1.17 | 2.59 | 8.53  | 12.7   | 18.9   | 41.8   | 62.1   | 137    | 304    | 1000    |
| 20 log G  (dB)        | 6.02  | 6.02  | 5.96 | 5.74 | 3.65  | 1.85   | -0.571 | -6.64  | -9.95  | -16.8  | -23.6  | -34.0   |
| Phase (degrees)       | -.086 | -3.06 | -10  | -22  | -64.9 | -88.14 | -116.0 | -196.0 | -259.0 | -479.0 | -959.0 | -2950.0 |

35. Sinusoids of varying frequencies were applied to an open-loop system and the following results were measured. Construct a Bode diagram and estimate the transfer function.

|                       |       |       |       |      |       |       |       |       |       |       |       |       |       |       |
|-----------------------|-------|-------|-------|------|-------|-------|-------|-------|-------|-------|-------|-------|-------|-------|
| Frequency (radians/s) | 0.11  | 0.24  | 0.53  | 1.17 | 2.6   | 5.7   | 12.7  | 28.1  | 62    | 137   | 304   | 453   | 672   | 1000  |
| Magnitude Ratio,  G   | 2.0   | 2.0   | 2.0   | 2.0  | 1.93  | 1.74  | 1.24  | 0.67  | 0.32  | 0.15  | .07   | 0.044 | 0.03  | 0.02  |
| Phase (degrees)       | -0.62 | -1.37 | -3.03 | -6.7 | -14.5 | -29.8 | -51.8 | -70.4 | -80.9 | -85.8 | -88.1 | -88.7 | -89.7 | -89.4 |

36. Sinusoids of varying frequencies were applied to an open-loop system and the following results were measured. (Data from [43].) Construct a Bode diagram for the data.

|                       |       |       |       |       |       |       |       |       |       |       |       |       |       |       |       |       |       |       |      |      |
|-----------------------|-------|-------|-------|-------|-------|-------|-------|-------|-------|-------|-------|-------|-------|-------|-------|-------|-------|-------|------|------|
| Frequency (radians/s) | 1     | 3     | 7     | 10    | 15    | 20    | 25    | 30    | 35    | 40    | 50    | 60    | 70    | 80    | 90    | 100   | 110   | 120   | 130  | 140  |
| Magnitude Ratio,  G   | 1     | .95   | .77   | .7    | .67   | .63   | .6    | .53   | .48   | .44   | .35   | .31   | .33   | .35   | .32   | .32   | .3    | .29   | .27  | .26  |
| Phase (radians)       | -.035 | -.227 | -.419 | -.541 | -.611 | -.768 | -.995 | -.108 | -.124 | -.131 | -.152 | -.192 | -.161 | -.183 | -.208 | -.223 | -.253 | -.272 | -.29 | -.30 |

Estimate the transfer function if it consists of (a) two poles; (b) a pole and a complex pole pair; (c) two poles, a zero, and a complex pole pair; (d) three poles, a zero, and a complex pole pair. (Hint: It may be useful to solve this program using the MATLAB System Identification toolbox or Seidel's program.)

37. The following data were collected for the step response for an unknown first-order system. Find the parameters that describe the model.

|      |      |       |      |       |      |       |      |       |      |       |      |       |      |      |
|------|------|-------|------|-------|------|-------|------|-------|------|-------|------|-------|------|------|
| T    | 0.0  | 0.005 | 0.01 | 0.015 | 0.02 | 0.025 | 0.03 | 0.035 | 0.04 | 0.045 | 0.05 | 0.055 | 0.06 | 0.07 |
| v(t) | 0.00 | 3.41  | 5.65 | 7.13  | 8.11 | 8.75  | 9.18 | 9.46  | 9.64 | 9.76  | 9.84 | 9.90  | 9.93 | 10.0 |

38. Suppose a second-order underdamped system response to a step is given by Eq. (13.73) and has  $C = 10$ ,  $T_p = 0.050$ , and  $y(T_p) = 10.1$ . Find  $\zeta$  and  $\omega_n$ . A stylized  $10^\circ$  saccade is shown in the following figure. Estimate  $\zeta$  and  $\omega_n$  for the Westheimer model. Calculate the time to peak velocity and peak velocity.
39. Consider the data in Figure 13.80. Estimate  $\zeta$ ,  $\omega_n$ , and  $\phi$  if the system has the solution of the form of Eq. (13.73).

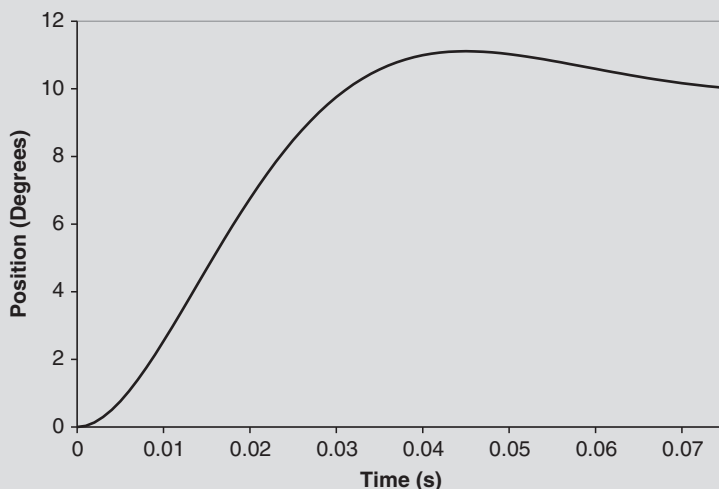


FIGURE 13.80 Illustration for Exercise 39.

## References

- [1] A.T. Bahill, Bioengineering: Biomedical, Medical and Clinical Engineering, Prentice-Hall, Inc., Englewood Cliffs, NJ, 1981.
- [2] A.T. Bahill, L. Stark, The high-frequency burst of motoneuronal activity lasts about half the duration of saccadic eye movements, *J. Neurophys.* 33 (1975b) 382–392.
- [3] A.T. Bahill, M.R. Clark, L. Stark, The main sequence, a tool for studying human eye movements, *Math. Biosci.* 24 (1975a) 194–204.
- [4] A.T. Bahill, J.R. Latimer, B.T. Troost, Linear homeomorphic model for human movement, *IEEE Trans. Biomed. Eng. BME-27* (1980) 631–639.
- [5] R.H.S. Carpenter, Movements of the Eyes, second ed., Pion Ltd., London, 1988.
- [6] M.R. Close, A.R. Luff, Dynamic properties of inferior rectus muscle of the rat, *J. Physiol., London* 236 (1974) 258.
- [7] C.C. Collins, The human oculomotor control system, in: G. Lennerstrand, P. Bach-y-Rita (Eds.), *Basic Mechanisms of Ocular Motility and Their Clinical Implications*, Pergamon Press, Inc., Oxford, 1975, pp. 145–180.
- [8] C.C. Collins, D. O'Meara, A.B. Scott, Muscle tension during unrestrained human eye movements, *J. Physiol.* 245 (1975) 351–369.
- [9] J.D. Enderle, Observations on Pilot Neurosensory Control Performance During Saccadic Eye Movements, *Aviat. Space Environ. Med.* 59 (1988) 309–313.
- [10] J.D. Enderle, A Physiological Neural Network for Saccadic Eye Movement Control. Air Force Material Command, in: Armstrong Laboratory AL/AO-TR-1994-0023, 1994, p. 48.
- [11] J.D. Enderle, Neural Control of Saccades, in: J. Hyönä, D. Munoz, W. Heide, R. Radach (Eds.), *The Brain's Eyes: Neurobiological and Clinical Aspects to Oculomotor Research, Progress in Brain Research*, vol. 140, Elsevier, Amsterdam, 2002, pp. 21–50.
- [12] J.D. Enderle, Eye Movements, in: M. Akay (Ed.), *Wiley Encyclopedia of Biomedical Engineering*, John Wiley & Sons, Inc., Hoboken, 2006a.
- [13] J.D. Enderle, The Fast Eye Movement Control System, in: J. Bronzino (Ed.), *The Biomedical Engineering Handbook Biomedical Engineering Fundamentals*, third ed., CRC Press, Inc., Boca Raton, FL, 2006b, Chapter 16, pages 16-1 to 16-21.
- [14] J.D. Enderle, Models of Horizontal Eye Movements. Part 1: Early Models of Saccades and Smooth Pursuit, Morgan & Claypool Publishers, San Rafael, CA, 2010, p. 149.
- [15] J.D. Enderle, E.J. Engelken, Simulation of Oculomotor Post-Inhibitory Rebound Burst Firing Using a Hodgkin-Huxley Model of a Neuron, *Biomed. Sci. Instrum.* 31 (1995) 53–58.
- [16] J.D. Enderle, J.W. Wolfe, Time-Optimal Control of Saccadic Eye Movements, *IEEE Trans. Biomed. Eng. BME-34* (1) (1987) 43–55.
- [17] J.D. Enderle, J.W. Wolfe, Frequency Response Analysis of Human Saccadic Eye Movements: Estimation of Stochastic Muscle Forces, *Comp. Bio. Med.* 18 (1988) 195–219.
- [18] J.D. Enderle, W. Zhou, Models of Horizontal Eye Movements. Part 2: A 3rd-Order Linear Saccade Model, Morgan & Claypool Publishers, San Rafael, CA, 2010, p. 144.
- [19] J.D. Enderle, E.J. Engelken, R.N. Stiles, A comparison of static and dynamic characteristics between rectus eye muscle and linear muscle model predictions, *IEEE Trans. Biomed. Eng.* 38 (1991) 1235–1245.
- [20] J.D. Enderle, J.W. Wolfe, J.T. Yates, The Linear Homeomorphic Saccadic Eye Movement Model — A Modification, *IEEE Trans. Biomed. Eng. BME-31* (11) (1984) 717–720.
- [21] E.J. Engelken, K.W. Stevens, J.W. Wolfe, J.T. Yates, A Limbus Sensing Eye-Movement Recorder, USAF School of Aerospace Medicine, Brooks AFB, TX, 1984, USAFSAM-TR-84-29.
- [22] W.O. Fenn, B.S. Marsh, Muscular Force at different speeds of shortening, *J. Physiol. (London)* 35 (1935) 277–297.
- [23] A.F. Fuchs, C. Kaneko, C. Scudder, Brainstem Control of Saccadic Eye Movements, *Annu. Rev. Neurosci.* 8 (1985) 307–337.
- [24] A.F. Fuchs, E.S. Luschei, Firing patterns of abducens neurons of alert monkeys in relationship to horizontal eye movement, *J. Neurophysiol.* 33 (3) (1970) 382–392.
- [25] N.J. Gandhi, E.L. Keller, Spatial distribution and discharge characteristics of the superior colliculus neurons antidromically activated from the omnipause region in monkey, *J. Neurophysiol.* 76 (1997) 2221–2225.

- [26] H. Goldstein, The neural encoding of saccades in the rhesus monkey (Ph.D. dissertation), The Johns Hopkins University, Baltimore, MD, 1983.
- [27] M.R. Harwood, L.E. Mezey, C.M. Harris, The Spectral Main Sequence of Human Saccades, *J. Neurosci.* 19 (20) (1999) 9098–9106.
- [28] A.V. Hill, The heat of shortening and dynamic constants of muscle, *Pro. Royal Soc., London (B)* 126 (1938) 136–195.
- [29] A.V. Hill, The development of the active-state of muscle during the latent period, *Pro. Royal Soc., London (B)* 137 (1950a) 320–329.
- [30] A.V. Hill, The series elastic component of muscle, *Pro. Royal Soc., London (B)* 137 (1950) 273–280.
- [31] A.V. Hill, The transition from rest to full activity in muscles: the velocity of shortening, *Pro. Royal Soc., London (B)* 138 (1951a) 329–338.
- [32] A.V. Hill, The effect of series compliance on the tension developed in a muscle twitch, *Pro. Royal Soc., London (B)* 138 (1951b) 325–329.
- [33] F.K. Hsu, A.T. Bahill, L. Stark, Parametric sensitivity of a homeomorphic model for saccadic and vergence eye movements, *Comp. Prog. Biomed.* 6 (1976) 108–116.
- [34] X. Hu, H. Jiang, C. Gu, C. Li, D. Sparks, Reliability of Oculomotor Command Signals Carried by Individual Neurons, *PNAS* (2007) 8137–8142.
- [35] M.C. Khoo, *Physiological Control Systems: Analysis, Simulation, and Estimation*, IEEE Press, Piscataway, NJ, 2000.
- [36] R.J. Leigh, D.S. Zee, *The Neurology of Eye Movements*, third ed., Oxford University Press, New York, 1999.
- [37] A. Levin, J. Wyman, The viscous elastic properties of a muscle, *Pro. Royal Soc., London (B)* 101 (1927) 218–243.
- [38] L. Ling, A. Fuchs, C. Siebold, P. Dean, Effects of initial eye position on saccade-related behavior of abducens nucleus neurons in the primate, *J. Neurophysiol.* 98 (6) (2007) 3581–3599.
- [39] S. Ramat, R.J. Leigh, D. Zee, L. Optican, What Clinical Disorders Tell Us about the Neural Control of Saccadic Eye Movements, *Brain* (2007) 1–26.
- [40] D.A. Robinson, Oculomotor control signals, in: G. Lennerstrand, P. Bach-y-Rita (Eds.), *Basic Mechanisms of Ocular Motility and their Clinical Implication*, Pergamon Press, Oxford, 1975, pp. 337–374.
- [41] D.A. Robinson, The Mechanics of Human Saccadic Eye Movement, *J. Physiol., London* 174 (1964) 245.
- [42] D.A. Robinson, Models of mechanics of eye movements, in: B.L. Zuber (Ed.), *Models of Oculomotor Behavior and Control*, CRC Press, Boca Raton, FL, 1981, pp. 21–41.
- [43] R.C. Seidel, Transfer-function-parameter estimation from frequency-response data – A FORTRAN program, (1975). NASA TM X-3286 Report.
- [44] D.L. Sparks, R. Holland, B.L. Guthrie, Size and distribution of movement fields in the monkey superior colliculus, *Brain Res.* 113 (1976) 21–34.
- [45] P.A. Sylvestre, K.E. Cullen, Quantitative analysis of abducens neuron discharge dynamics during saccadic and slow eye movements, *J. Neurophysiol.* 82 (5) (1999) 2612–2632.
- [46] J.A. Van Gisbergen, D.A. Robinson, S. Gielen, A quantitative analysis of generation of saccadic eye movements by burst neurons, *J. Neurophysiol.* 45 (3) (1981) 417–442.
- [47] R.B. Weber, R.B. Daroff, Corrective movements following refixation saccades: Type and control system analysis, *Vision Res.* 12 (1972) 467–475.
- [48] G. Westheimer, Mechanism of saccadic eye movements, *AMA Arch. Ophthalmol.* 52 (1954) 710–724.
- [49] D.R. Wilkie, *Muscle: Studies in Biology*, vol. 11, Edward Arnold Ltd., London, United Kingdom, 1968.
- [50] W. Zhou, X. Chen, Enderle, An Updated Time-Optimal 3rd-Order Linear Saccadic Eye Plant Model, *Int. J. Neural. Syst.* 19 (5) (2009) 309–330.